University of KwaZulu-Natal

Giant Radio Halos and Relics in ACTPol Clusters

by

Sinenhlanhla Precious Sikhosana

A research project submitted in fulfillment of the academic requirement for the University of KwaZulu-Natal, School of Mathematics, Statistics and Computer Science Master of Science degree.

Durban

March, 2017

As the candidate's supervisor I have approved this thesis for submission.

Signed: _____ Name: _____ Date: _____

Abstract

Galaxy clusters are the largest gravitationally-bound structures in the universe. They act as the largest astrophysical laboratories in the universe and are extremely interesting objects to study as they are at crossroads between astrophysics and cosmology. In previous decades the most prominent cluster studies were focused on thermal processes in the intracluster medium (ICM). However, recent studies have shown that non-thermal studies give a different perspective on ICM processes.

Giant radio halos and radio relics are examples of this non-thermal diffuse radio emission. Giant radio halos are believed to originate from synchrotron radiation resulting from the re-acceleration of relativistic electrons in the cluster's magnetic field by the turbulent energy following merger activity. Radio relics, another form of non-thermal diffuse radio emission, have been identified as possible tracers of merger shock waves. The study of diffuse radio emission has a number of open questions such as; the observed bimodality in the radio power versus X-ray luminosity plot. The bimodality could partly be due to the identification of halos and relics in clusters without a well-defined selection function.

In this thesis, we studied giant radio halos and relics in a homogeneous, mass-selected sample of sixteen clusters selected via the Sunyaev- Zel'dovich (SZ) effect by the Atacama Cosmology Telescope (ACT) with polarization sensitive receivers (ACTPol). We carried out a radio wavelength study using data obtained from the Giant Metrewave Radio Telescope (GMRT) for four of these clusters. This subsample of four clusters will be added to the larger sample, eight of which have archival data, and four of which will be proposed for observations in the next GMRT observation cycle. We used the GMRT data at 610 MHz to search for diffuse radio emission in each cluster. We applied various uv-cuts and tapers to isolate the low-resolution emission in the target field. For two of the four observed clusters, we tentatively discovered extended radio emission at a significance level of at least 3σ. We then measured radio fluxes for compact sources in the cluster region. We were able to calculate spectral indices for the compact sources that were cross-matched in FIRST.

keywords: intracluster medium, diffuse radio emission, radio halos, radio relics, merger, shock waves, and bimodality.

Acknowledgments

I would like to thank Prof. Kavilan Moodley for his constant supervision and guidance throughout my project. I would have never been able to quickly grasp vital astronomy tools and concepts without the mentorship of Dr. Kenda Knowles; her input is greatly appreciated. I am thankful for the technical advice that was given by Dr. Huib Intema; through his suggestions, we were able to obtain scientifically satisfying images.

For this project I was fully funded by the SKA South Africa project, with the funding, I was able to purchase equipment which optimized my research and with the travel grant, I was able to attend conferences.

Preface

The work described in this thesis was carried out in the School of Mathematics, Statistics, and Computer Science, University of KwaZulu-Natal, from January 2015 to December 2016. This dissertation was completed under the supervision of Prof. K. Moodley and the mentorship of Dr. K. Knowles.

This study represents original work by the author and has not been submitted in any form for any degree or diploma to any other tertiary institution. Where use was made of the work of others it has been duly acknowledged in the text.

Declaration

I, **Sinenhlanhla Precious Sikhosana**, fully understand the meaning of plagiarism and hereby declare that all of the work in this document, unless stated otherwise through source acknowledgment, is my original research.

Signature:

_____

Date:

_____

Contents

List of Figures

List of Tables

CHAPTER 1

Introduction

For centuries astronomers believed that the bulk of the universe's constituents was the visible baryonic matter. It was the measurements of stellar velocities and the observations of Type 1a supernova (SNeIa) that proved that there were missing components in the cosmological model (Oort, 1932; Rubin et al., 1964; Riess et al., 1999; Perlmutter et al., 1999). These discoveries showed that contrary to what was believed, baryonic matter only made up approximately five percent of the universe. This led to the development of the current cosmological model, known as the concordance Λ Cold Dark Matter (ΛCDM) model. In this model, the universe is made up of $\sim$5% baryonic matter, $\sim$25% cold dark matter, and $\sim$70% dark energy. The first observational evidence was found when Oort (1932) measured the doppler shift in spectra of the stars in the Milky Way. He found that the velocity of the stars was much greater than what was theoretically predicted. Zwicky (1933) also found that the galaxy peculiar velocities in the Coma Cluster were much higher than predicted by theory, he concluded that there was an unobserved matter component which was responsible for the high velocities. This matter component was then referred to as 'dark matter'. Cold dark matter is collisionless and can only be observed through its gravitational effects. Presently the most promising candidate of what cold dark matter is, are the Weakly Interacting Particles (WIMPs) (Clowe et al., 2004). Dark energy, which is the major component of the ΛCDM universe, can be better understood when using the Einstein field equations (Dvali et al., 2000). Its existence was inferred from the SNeIa observations that revealed

that the universe is expanding at an accelerated rate (Riess et al., 1999; Perlmutter et al., 1999). Studies such as those done by Allen et al. (2004) further constrained the dark energy content in the universe. The Cosmic Microwave Background (CMB) has been crucial for constraining the cosmological parameters (Planck Collaboration et al., 2016b) and the Planck Telescope has played a major role in the currently accepted cosmological parameters. The ΛCDM model has been tested against many observations such as CMB surveys (Planck Collaboration et al., 2016b; Das et al., 2014) and dark energy surveys (Parkinson et al., 2012; Sullivan et al., 2011). Although the model seems to account for what is observed, there are still a lot of unknowns that need to be clarified such as the recent discovery of the non-zero neutrino mass (Kajita, 2016; McDonald, 2006). It is clear that new physics is required to fully explain the existence of the non-baryonic cold dark matter and dark energy. The understanding of these constituents is fully dependent on simultaneous progress in particles physics, cosmology theory and experiments (Olive and Particle Data Group, 2014).

In the quest to obtain the most accurate cosmological model, scientists design surveys using the most powerful telescopes that observe the universe across the electromagnetic spectrum. The main aim of these surveys is to constrain cosmological parameters such as the Hubble parameter (H_0), baryonic matter density ($\Omega_b h^2$), cold dark matter density ($\Omega_c h^2$), matter in the universe (Ω_m), dark energy (Ω_Λ), spatial curvature (Ω_K), and many other parameters of the ΛCDM model (Ω is the dimensionless density parameter, where $\Omega = \frac{\rho}{\rho_c}$). Events occurring at different epochs can be used to constrain the model. The Baryon Acoustic Oscillation (BAO) signal, which is evident from the CMB's matter power spectrum, is one example of the probes (Beutler and BOSS Collaboration, 2015). The BAOs are pressure waves that resulted from the motion of contraction caused by gravitational collapse and rarefaction caused by the baryon's radiation pressure. The BAO scale can be used as a standard ruler for the measurement of angular diameter distance. It can also be used to constrain cosmological parameters such the Hubble parameter and the matter density in the universe (Alam et al., 2016; Ross et al., 2015). The BAOs have been used to break degeneracy from CMB cosmological parameter measurements (Planck Collaboration et al., 2016b; Sievers et al., 2013).

As mentioned above, the CMB power spectrum can also be used to constrain cosmological parameters. The photons from the CMB, released after decoupling, travel through the universe and interact with matter on both small and large scales. It is these interactions that make the CMB the primary tool for measuring cosmological parameters such as the

neutrino mass ν, the curvature of the universe and the dark energy equation of state w ($w = \frac{p}{\rho}$). The anisotropies in the CMB, measured by the Cosmic Background Explorer satellite (COBE) (Bennett et al., 1993) showed that there were matter fluctuations which are responsible for the large-scale structure we see today. The Wilkinson Microwave Anisotropy Probe (WMAP) (Bennett et al., 2013) improved the measurements of the fluctuation and (Planck Collaboration et al., 2016b) is the latest survey that accurately measured these fluctuations. From the CMB anisotropies, one can accurately constrain matter density in the universe which is done by the large CMB surveys. The Planck 2016 results provide the most accurate constraints of the cosmological parameters to date (Planck Collaboration et al., 2016b). The Atacama Cosmology Telescope (ACT; Das et al., 2014) and the South Pole Telescope (SPT; George et al., 2015) are ground based CMB experiments providing high quality data.

The CMB data is also used to measure the weak gravitational lensing effect. Weak gravitational lensing has been widely exploited as a probe of the dark matter. Weak lensing is a valuable probe as it simultaneously probes background evolution of large-scale structure and the growth of cosmic structure (Camera et al., 2016). The Canada-France-Hawaii Telescope Lensing Survey (CFHTLenS; Fu et al., 2014) uses weak lensing to constrain cosmological parameters. Constraints on shapes of dark matter halos using weak lensing are obtained in the Red-sequence Cluster Survey (RCS; van Uitert et al., 2012). Weak gravitational lensing will also be used by future surveys, such as the Square Kilometer Array (SKA), to give tight constraints at even higher redshifts. The Kilo-Degree Survey (KiDS; Hildebrandt et al., 2016), unlike most surveys that aim to target high redshifts, will target low redshifts to probe large-scale structure and will obtain shear measurements of fifteen million galaxies. This will be the first survey to produce a tomographic cosmic shear analysis of the flat ΛCDM model. Gravitational lensing of large-scale structure has been also used as a direct probe of dark matter (Clowe et al., 2004; Markevitch et al., 2004) while weak gravitational lensing has been claimed to have the highest precision when constraining dark matter density (Camera et al., 2016). Gravitational lensing from optical surveys such as the Sloan Digital Sky Survey (SDSS; Alam et al., 2016) and the Hubble Space Telescope (HST; Lesgourgues et al., 2007) have been used, in the form of galaxy spectroscopic catalogs, to constrain the Hubble parameter, the curvature of the universe, and other parameters.

Type Ia supernovae have been used as a probe of dark energy (Riess et al., 1999; Perlmutter et al., 1999). The intrinsic luminosity of SNeIa makes them good candidates for standard

candles. Their luminosity distance is measured using light curves and these observational results are compared to the theory. These studies showed an expanding universe, hence, inferred the existence of dark energy (Riess et al., 1999; Perlmutter et al., 1999). After these findings, many other surveys have measured the light curves of thousands of SNeIa (Betoule et al., 2014). These surveys further cement the result of the cosmic acceleration. Future surveys such as the large synoptic survey telescope (LSST; Odderskov and Hannestad, 2016) and the Dark Energy Survey (DES) (Abbott et al., 2016) will detect a larger amount of the SNeIa and probe current cosmological models.

Another probe of dark energy are the galaxy cluster counts. The number density of clusters as a function of redshift depends on the rate at which the cosmic structures grow. It also depends on the cosmic volume element as a function of redshift. This dependence on redshift allows one to use the cluster counts to probe dynamical and geometric aspects of the cosmological model. Surveys such as Planck (Planck Collaboration et al., 2016b) and ACT (Hasselfield et al., 2013) use cluster counts to probe the nature of dark energy and its current models. Galaxy cluster counts are essential for constraining the cosmological parameters and in turn the ΛCDM model (Albrecht et al., 2009). To fully exploit cluster counts as a cosmological probe it is important that we have a clear understanding of the formation and evolution of galaxy clusters.

Large-scale structures in the form of galaxy clusters are the largest gravitationally-bound objects. Since their detection, they have been used in astrophysical and cosmological studies. The first of these objects to be detected was the Coma cluster (Zwicky, 1937a). Since its discovery, many studies were conducted to understand the nature of galaxy clusters (Rood et al., 1972; Briel et al., 1992). Another breakthrough in the galaxy cluster field was the detection of the Bullet Cluster (Tucker et al., 1998). This merging cluster, when observed at multiwavelengths, reveals the colliding dark matter of the two galaxy clusters (Markevitch et al., 2004). Hence, bullet clusters can be used to probe dark matter (Paraficz et al., 2016). Galaxy cluster systems can be observed at multiwavelengths, with each spectral window revealing unique information on the formation and evolution of clusters. Future generation surveys will detect large numbers of galaxy clusters (Ascaso et al., 2015). These clusters will be of higher redshift and lower mass compared to the current galaxy cluster surveys (Prandoni and Seymour, 2015). Hence, new methods will be required to allocate galaxy cluster members (Acosta-Pulido et al., 2015; Battistelli et al., 2016). The lower mass and higher redshift studies will open up a window of studying the early formation and evolution

of galaxy clusters.

Further studies on galaxy clusters particularly at X-ray wavelengths showed that clusters had substructures (Buote, 2001; Schuecker et al., 2001). The Spitzer and XMM-Newton telescopes have also been used to investigate the morphology of clusters (Papovich et al., 2010; Merten and CLASH, 2014). Magnetohydrodynamic (MHD) simulations have been conducted to better understand the equilibrium and non-equilibrium states of clusters and to classify relaxed and unrelaxed clusters (Biffi et al., 2016). The X-ray observations (Sarazin, 2004) and the MHD simulations revealed that the galaxy clusters with substructures were actually undergoing merger activity. Cluster mergers are the most energetic events in the universe since the big bang. This event is also responsible for astrophysical activities that occur in the intracluster medium (ICM) (Vazza et al., 2006). These merger activities result in non-thermal diffuse radio emission that can not be related to individual galaxies (Wylezalek et al., 2013) and the ICM (Sommer et al., 2016; Malu et al., 2016).

Galaxy clusters that are found to host diffuse radio emission often have a high mass range. These clusters are often selected according to thermal activity that is found to be directly proportional to the cluster mass. The first mass proxy successfully used was based on the X-ray luminosity of the cluster (Sunyaev and Zeldovich, 1972; Rottgering et al., 1997; Boschin et al., 2012; Botteon et al., 2016). Numerous clusters selected by X-ray luminosity showed evidence of diffuse radio emission, however, this number was much smaller than what was theoretically predicted (Feretti et al., 2012). Scaling relations have been derived for these clusters that host diffuse radio emission (Cassano et al., 2013). In recent years the SZ effect has been used as a mass proxy (Planck Collaboration et al., 2013). The SZ effect, integrated along the line of sight, proved to be a more robust method for targeting high mass clusters at high redshifts (Hasselfield et al., 2013). A reasonable number of SZ-selected clusters has been found to host diffuse radio emission (Venturi et al., 2007). The diffuse radio emission has been categorized into three groups: giant radio halos (GRHs), radio mini-halos, and radio relics (RRs).

Each of these sources of diffuse radio emission has its own formation theory. The hadronic model states that GRH emission is produced through cosmic ray proton and thermal proton collision (Donnert et al., 2013; Brunetti, 2011a). This proton-proton reaction produces gamma-rays as a by-product (Donnert et al., 2013). These gamma-rays have not been detected yet but multiple surveys are focused on searching for them (Ackermann et al., 2014; Brunetti et al., 2012). The second and observationally convincing formation theory for

GRH is the turbulent re-acceleration model. This model indicates that the GRH emission is from the pre-existing electrons which are re-accelerated by merger activity (Beresnyak et al., 2013; Brunetti, 2004b; Cassano et al., 2016). The formation theory for radio mini-halos is that existing electrons deposited by AGN activity are re-accelerated by turbulence in the core region of the intracluster medium, mostly known as sloshing (Bravi et al., 2015). The observationally prevailing theory for the formation of RRs is that they are remnants of now inactive AGN lobes that are re-accelerated by adiabatic compression from merger shock waves (Enßlin et al., 1998; Berrington and Dermer, 2002; Kang and Ryu, 2016). To validate these theories, they need to be tested with observational data.

Many surveys have carried out extensive multiwavelength studies on clusters that host GRHs in order to understand their internal dynamics. The study of Abell 773 showed that the cluster was undergoing merger activity and it was found that the GRH in this cluster was associated with the merger (Barrena et al., 2007). In A520, a bow shock was found in the cluster which hosts a GRH, clearly indicating merger activity in the cluster (Markevitch et al., 2005). Another study of cluster ACT-CL J0256.5+0006 selected via the SZ effect indicated merger activity when observed in the X-ray (Knowles et al., 2016). The discovery of ultra-steep spectra radio halos (USSRHs) such as in van Weeren et al. (2009) was a confirmation of the predictions made by the turbulent re-acceleration model (Brunetti, 2004b), and provided further observational evidence supporting this model. Very few radio mini-halos have been detected, however, recently a mini-halo was detected in the RXCJ1504.1-0248 cluster (Giacintucci et al., 2011). This cluster exhibits an extreme cool-core. X-ray observations from Chandra indicated that the mini-halo was related to particle acceleration by turbulence in the cool core. A radio relic studied in (Giacintucci et al., 2008) was related to shock acceleration through spectral properties which were consistent with the acceleration of cosmic ray electrons (CRe) by shocks in the ICM. The X-ray surface brightness edge coincided with the outer border of the relic, further suggesting the shock wave relation. The radio relic in the galaxy cluster PLCKG287.0+32.9 (Bonafede et al., 2014) was associated with lobes of a radio galaxy. The steep spectrum on both ends of the relic proved that it was associated with particle re-acceleration. X-ray studies of the highest redshift cluster 'El Gordo', which hosts both a radio halo and a relic, showed the presence of a merger-induced shock (Botteon et al., 2016).

Although these observations largely support the existing theories, there have been a few observations that indicate that further understanding of diffuse radio emission is required in

order to build the most accurate formation models. A study on Abell 3411 showed complex diffuse radio emission which was broken up into 5 fragments. Although the emission was classified as a radio relic current models do not account for the observed fragmentation. The cluster CL1821+643 which has a cool core was found to host a GRH (Kale and Parekh, 2016). Cool-core clusters were previously associated with dynamically stable clusters, hence, this detection contradicted the known theoretical predictions. Such observations indicate that new surveys are required that will probe new parts of the parameter space, such as low mass and high redshift clusters. Radio surveys such as LOFAR and the SKA will probe such parts of the parameter space and this will give insight into the evolution of diffuse radio emission hosted in clusters (Brunetti and Jones, 2014). The SKA telescope will observe cool-core clusters and the evolution of radio mini-halos (Gitti et al., 2015). The simulations by (Govoni et al., 2015) predicted that the SKA will be able to detect polarization of GRHs. A combination of future generation radio surveys and other high-energy surveys will result in exciting discoveries which will further develop diffuse radio emission theory and the understanding of the intracluster medium.

Although the detection of diffuse radio emission in clusters has increased over the past few years more detections are necessary in order to have complete samples that can be used for statistical analysis of diffuse radio sources. These studies will broaden our understating of the intracluster medium and give us an insight of the events that occur during the evolution of the diffuse radio sources. In this project, we search for diffuse radio emission in clusters uniformly selected via the SZ effect from the ACT survey with polarization sensitive receivers (ACTPol). These clusters were observed using target observation from the Giant Metrewave Radio Telescope at 610 MHz. These clusters are a sub-sample of a pilot project (PI: Dr. K. Knowles) which aims to study a complete sample of 16 SZ-selected clusters from ACTPol and to perform statistical studies such as the SZ-radio scaling relations. The main aim of the pilot project is to verify the formation and evolution theories of diffuse radio sources in clusters.

This thesis is structured as follows. In chapter two we give a theoretical background on topics such as the cosmological model, galaxy clusters, radio halos and radio relics. In chapter three we present the methods used to analyze radio data and give a brief insight into how radio interferometers operate. We present the cluster sample selection in chapter four and describe the specific analysis methods applied to our sample. In chapter five we summarize our results and outline the future work that follows from our findings.

The following cosmological parameters are adopted throughout the thesis, unless stated otherwise: $\Omega_k = 0$, $\mathrm{H}_0 = 70$ $\mathrm{kms}^{-1}\mathrm{Mpc}^{-1}$, $\Omega_\Lambda = 0.73$, $\Omega_m = 0.27$.

CHAPTER 2

Theoretical Background

Our understanding of the universe has significantly increased over the past decades. This is due to the combination of several cosmological probes such as the CMB, BAOs, gravitational lensing, supernovae and galaxy cluster counts. These probes have been used refine cosmological models by constraining the cosmological parameters. The tight cosmological constraints have introduced a number of open questions as the current models fail to explain some observations. New generation surveys, with a combination of cosmological probes, are required to answer these open questions. The constraining power of an individual cosmological probe is usually too weak to constrain all the parameters simultaneously. However, by combining different probes, it is possible to place tight constraints on the cosmological parameters, to break degeneracies between them and to reduce uncertainties. Hence, a thorough understanding of a variety of cosmological probes is required to have the most accurate model of the universe.

2.1 Cosmological Model

Currently, the accepted theory of the formation of the universe is the Big Bang Theory. This theory states that the universe was an extremely compact, hot and dense plasma in its early stages. A cosmic explosion ('Big Bang') that occurred 13.7 billion years ago resulted in the expansion and cooling of the universe. The first observational evidence

proving that the universe is expanding was provided by Edwin Hubble (Hubble, 1929). He measured the relation between the redshift of galaxies and their distance. He found that the redshift of galaxies further away was larger that the redshift of galaxies nearby, proving that the galaxies were receding. From the measurements, he derived the Hubble law, which describes the linear relationship between redshifts of galaxies and their distance from the observer. In addition to the expanding universe, in 1998, it was discovered that the rate of expansion was actually accelerating (Riess et al., 1999; Perlmutter et al., 1999). The current model that explains most of these observations is the ΛCDM model. For years the widely accepted standard cosmology model, which was the cold dark matter model (Lemaître, 1931), assumed that the universe was expanding at a constant rate. However, observations showed discrepancies when the measurements of cosmological parameters were compared to what model predicted. To account for the discrepancies, the Λ term introduced by (Einstein, 1917) and (Lemaître, 1949) was re-introduced by (Riess et al., 1999; Perlmutter et al., 1999). The ΛCDM model, which we refer to when describing the cosmos, constitutes dark energy, cold dark matter, and baryonic matter. As more accurate cosmological probes are discovered the accuracy of the measurements of the cosmological parameters increases. The CMB is one of the powerful probes that is used to constrain multiple cosmological parameters

The CMB is the thermal radiation that was released 380 000 years after the Big Bang. The very early universe was extremely hot, dense and filled with a hydrogen plasma. As the universe expanded, this plasma cooled to the point where protons and electrons could combine to form atoms. This is referred to as the epoch of recombination (Hu and Dodelson, 2002). These neutral atoms could not scatter the photons, hence, the universe went from being dense and opaque to being transparent. Shortly after this, photons that were previously scattered by the electrons and protons of the plasma were able to escape freely into space. This is known as photon decoupling and during this epoch, the photons were at a temperature of ≈ 3000 K. These photons that existed at the time of decoupling have since been propagating, losing energy and increasing in wavelength. It is these photons that are observed even today and are referred to as the CMB. The CMB is well described as a black body with a temperature ($\sim$2.73 K) that is uniform across the sky. This uniformity suggests that the different parts of the universe were related at the time of last scatter. Upon its discovery (Penzias and Wilson, 1965), it was believed that the CMB was homogeneous and isotropic. In 1992 an experiment carried out using the COBE satellite discovered that the CMB is not entirely isotropic but has anisotropies of the order 10^{-5} (Smoot et al., 1992).

These anisotropies are an imprint of primordial perturbations in the early universe. These perturbations are believed to have originated from quantum fluctuations.

The CMB anisotropies are produced in the same density fluctuations that are responsible for the formation of small-scale and large-scale structure. The fluctuations from the anisotropies resulted in overdense and underdense regions in the universe, which created gravitational potential wells (Hu and Dodelson, 2002). The dark matter which was already present during this epoch was pulled into the potential wells and collapsed to form dark matter halos. The baryonic matter which was present after recombination was gravitationally pulled by the dark matter halos. These structures grew in size until they reached Jean's length* and collapsed under gravity to form the large-scale structure that we see today. Dark matter was a catalyst for structure formation. It is believed that in the absence of dark matter the large-scale structure that we see today would have taken a longer period to form. Using the matter power spectrum or the CMB power spectrum one can constrain parameters such as dark matter density, baryonic matter density, the curvature of space and the age of the universe.

Prior to the decoupling epoch, when the photons were scattered by electrons through Thompson scattering, radiation pressure opposed the gravitational collapse of matter (Hu and Dodelson, 2002). This continuous compression and rarefaction generated pressure waves known as the BAOs. These oscillations left a signature on the large-scale matter distribution and in the CMB anisotropy. It is this signal that is evident in the CMB power spectrum and can be used as a cosmological probe. The BAO signal has been used to break degeneracies in cosmological parameters measured in CMB surveys (Planck Collaboration et al., 2016b) and will serve as a probe of dark energy in future surveys. Other probes of dark energy include Type Ia supernovae, gravitational lensing, and galaxy clusters.

Type Ia supernovae are a result of white dwarfs which accrete mass from companion stars and explode when they reach the Chandrasekhar mass limit. This process enables supernovae to have a desirable characteristic intrinsic luminosity (Riess et al., 1999). The peak luminosity of a SNeIa can be used as an efficient distance indicator, allowing for cosmology to be constrained via the distance-redshift relation. The measured luminosity distance, in the form of the Hubble diagram, can be compared to the theoretical prediction to constrain Ω_m and Ω_Λ (Riess et al., 1999; Perlmutter et al., 1999).

When observing distant sources, images of galaxies along the line of sight are distorted

*The critical scale at which a gas cloud will collapse under its own gravitational force.

due to the gravitational effect of mass variations. Deep gravitational potential wells such as found in massive galaxy clusters generate strong lensing. This phenomenon leads to galaxies being stretched into arcs and even appearing as multiple images. More moderate gravitational perturbations give rise to weak lensing (Lewis and Challinor, 2006). Weak lensing is now widely used to measure the matter power spectrum in specified regions of the observable sky (Lesgourgues et al., 2007). It is this matter power spectrum that is used to constrain cosmological models (Gil-Marín et al., 2016).

Galaxy clusters are fundamental cosmological objects because they provide an independent measure of cosmological parameters with different systematics compared to the CMB, BAOs, SNeIa and gravitational lensing. In particular, galaxy clusters are used to test cosmology by measuring their mass function. The mass function is defined as the number density of clusters as a function of their mass and redshift. The precise determination of the mass function and its evolution can place tight constraints on the energy components of the universe (Albrecht et al., 2009; Planck Collaboration et al., 2016b; Hasselfield et al., 2013).

2.2 Galaxy Clusters

The ΛCDM model predicts a hierarchical structure formation. In this model, the nonlinear structure on small scales forms first, and as more structure forms under gravitational collapse large-scale structures like galaxies form. These structures create a deep potential well and more mass falls in, creating even larger structures such as galaxy clusters. Galaxy clusters are at the end of the formation hierarchy, hence, are the largest gravitationally-bound objects. Once a galaxy cluster is virialized it reaches dynamical equilibrium. This means that the kinetic energy of galaxies moving randomly inside the cluster generates a pressure strong enough to counteract gravitational collapse, with the balancing of these forces, gives stability to the cluster (Bahcall, 1977). A group of galaxy clusters forms the largest structures in the universe, these are known as superclusters. Due to the massive size of galaxy clusters, they are assumed to be the most accurate tracers of superclusters. They are found in regions where there are dark matter overdensities, hence, they can be seen as tracers of the dark matter distribution (Mana et al., 2013). The complex processes that go on in the intracluster medium (ICM) and the massive size of galaxy clusters position these objects at the crossroads of cosmology and astrophysics. The large-scale distribution of clusters can be used to probe cosmological parameters, while the intensive study of the ICM can be used

to test models of gravitational structure formation, galaxy formation, and plasma physics (Kravtsov and Borgani, 2012).

2.2.1 Galaxy Cluster Formation

To physically understand the formation of galaxy clusters and how hydrostatic equilibrium is reached we begin by deriving a simplified version of the growth of the matter overdensities. In the ΛCDM model, objects form via the gravitational collapse in the initial primordial overdensity field characterized by

$$\delta(\vec{x}) = \frac{\rho(\vec{x}) - \bar{\rho}_m}{\bar{\rho}_m}. \tag{2.1}$$

The assumption is that on large scales, $\delta(\vec{x})$ is a homogeneous isotropic Gaussian random field. This Gaussian random field can be better understood by the analysis of its statistical properties. These can be fully represented by the power spectrum P(k), where k is the modulus of the wave vector. Let us consider that the field is smoothed on the scale R, then

$$\delta_R(\vec{x}) \equiv \int \delta(\vec{x} - \vec{R}) W(\vec{x}, R) d^3r. \tag{2.2}$$

We can now relate the variance of the smoothed Gaussian random field to the power spectrum in the following way

$$\langle \delta_R^2 \rangle \equiv \sigma^2(R) = \frac{1}{(2\pi)^3} \int P(k) |\tilde{W}(\vec{k}, R)|^2 d^3k, \tag{2.3}$$

where $\tilde{W}$ is the Fourier transform of W which is the smoothing function. At high redshifts, the total mass as a function of redshift is written in the following way: M(z) = $\frac{4\pi}{3}\rho(z)R^3$. We can think of the density field smoothed on the scale R or the corresponding mass scale M. The smoothed Gaussian density field is also Gaussian with the probability distribution function that is given by

$$p(\delta_m) = \frac{1}{\sqrt{2\pi}\sigma(M)} e^{\left[-\frac{\delta_m^2}{2\sigma^2(M)}\right]}, \tag{2.4}$$

where $\frac{\sigma(R)}{R} \equiv \frac{\sigma(M)}{M}$. In the linear regime of the evolution of the structure formation, according to the ΛCDM model, the initial Gaussianity of the $\delta(\vec{x})$ field is preserved, while different Fourier modes $\delta(\vec{k})$ evolve independently and grow at the same rate, described by the linear

growth factor, $D(a)$, as a function of the universe expansion factor $a = (1+z)^{-1}$. For a ΛCDM cosmological model the evolution is given by

$$\delta(a) \propto D(a) = \frac{5\Omega_m}{2} E(a) \int_0^a \frac{da'}{[a'E(a')]^3}. \tag{2.5}$$

where Ω_m is the mass density parameter and $E(a)$ is the normalized expansion rate and explicitly described by

$$E(a) \equiv \frac{H(a)}{H_0} = [\Omega_m a^{-3} + (1 - \Omega_m - \Omega_\Lambda)a^{-2} + \Omega_\Lambda]^{\frac{1}{2}}, \tag{2.6}$$

where Ω_Λ is the the dark energy density parameter. This model fully describes the growth of large-scale structure in the linear regime. However, on a smaller scale, this model breaks down as non-Gaussianities are introduced. At these non-linear regimes, a modification is required. The spherical collapse model best describes the evolution of structure at these non-linear scales.

When the gravitational collapse of large-scale structure is balanced by the radiation pressure force, the galaxy cluster reaches hydrostatic equilibrium. The collisional baryonic components of the newly formed large-scale structure have their configuration described by the hydrostatic equilibrium equation. This basically states that when equilibrium is reached the pressure gradient $\nabla p(\vec{x})$ at point $\vec{x}$ is balanced by the gravitational potential $\phi(\vec{x})$ where

$$\nabla\phi(\vec{x}) = -\frac{\nabla p(\vec{x})}{\rho_g(\vec{x})}. \tag{2.7}$$

Assuming spherical symmetry, the hydrostatic equilibrium equation can be written as

$$\rho g^{-1} \frac{dp}{dr} = -\frac{GM(<r)}{r^2}. \tag{2.8}$$

Since these are collisional particles we can assume the ideal gas equation $p = \frac{\rho_g k_B T}{\mu m_p}$, where μ is the mean molecular weight and m_p the proton mass. We can now express the mass contained within a cluster region $M(<r)$ in terms of density profile $\rho_g(r)$ and temperature profile $T(r)$

$$M_{HE}(<r) = -\frac{rK_B T(r)}{G\mu m_p} \left[\frac{dln\rho_g(r)}{dlnr} + \frac{dlnT(r)}{dlnr}\right]. \tag{2.9}$$

The hydrodynamic state of a galaxy cluster can be analyzed using simulations (Biffi et al.,

2016; Donnert et al., 2013). In observations, a difference between optical and X-ray mass measurements is often interpreted as a lack of hydrostatic equilibrium in the observed cluster. The X-ray data can often reveal the hydrodynamical state of a cluster by the observed morphology of the galaxy cluster.

2.2.2 Mass Function

A galaxy cluster's mass is not a directly measurable property, instead, it is inferred using mass proxies (Zwicky, 1937b; Ettori et al., 2010; Anderson et al., 2014). The most commonly used mass proxies are: optical richness which is the number of red galaxies in a given cluster radius, the line of sight velocity dispersion, X-ray temperature, and luminosity, and lastly the most recently added probe is the integrated SZ parameter. Recently, the integrated SZ parameter has been the favoured mass proxy because it is a more robust indicator of the cluster mass. A cluster's mass is usually defined with respect to the critical or the mean density of the universe and it is assumed that it follows a halo density profile. We begin by defining the mass with respect to the critical density of the universe as a function of redshift, $\rho_c(z)$. For a dynamically relaxed cluster, we consider a spherical region of a virialized halo of radius R_Δ. This virialized sphere has volume and mean density

$$V_\Delta = \frac{4\pi}{3} R_\Delta^3 \tag{2.10}$$

$$\bar{\rho}(z) = \Delta \rho_c(z). \tag{2.11}$$

The total matter that is contained in the region R_Δ is defined to be the mass M_Δ

$$M_\Delta = V_\Delta \bar{\rho}(z) = \frac{4\pi}{3} R_\Delta^3 \Delta \rho_c(z). \tag{2.12}$$

Galaxy cluster properties are observed in high-density contrast regions, hence, the typical values of Δ are 200 or 500. The underlying mass density distribution of clusters can be well understood by studying the halo density distribution. Which means an intensive study of the halo density profiles such as the Navarro-Frenk-White profile or the Burket profile (Mana et al., 2013) is required.

Once the cluster mass definition is fully described one can further investigate the mass function. The mass function is defined as the number density of the galaxy clusters as a function of mass. The mathematical relation is expressed as the number density of virialized

dark matter halos at redshift z within the mass range [M, M + dM]

$$\frac{dn(M,z)}{dlnM} = \bar{\rho}_m |\frac{d\log\sigma^{-1}}{dM}| f(\nu). \tag{2.13}$$

Where, $\bar{\rho}_m$ is the mean matter density, $\nu \equiv \frac{\delta_c}{\sigma(M,z)}$ and f(ν) is the analytical function obtained when evaluating the derivative, δ_c is the critical linear overdensity and $\sigma^2(M,z)$ is the variance of the density fluctuation field. The Press-Schechter formalism (Press and Schechter, 1974) was previously used to derive the mass function. In this formalism, the linear growth of the density fluctuation field is combined with the spherical top-hat collapse model to analytically derive the mass function. The Press-Schechter mass function takes the following form

$$\frac{dn(M,z)}{dM} = \frac{2}{V}\frac{\partial p_{\delta_M > \delta_c}(M,z)}{\partial M} = -\sqrt{\frac{2}{\pi}}\frac{\bar{\rho}_m \delta_c}{M\sigma_M^2}\frac{d\sigma_M}{dM} e^{\left(-\frac{\delta_c^2}{2\sigma_M^2}\right)}. \tag{2.14}$$

Here V=$\frac{M}{\bar{\rho}_m}$, δ_M is the smoothed density field and p_{δ_M} is the Gaussian probability distribution assigned to the smoothed density field. The shape of this mass function and its evolution was in broad agreement with what was measured in the numerical simulations of hierarchical galaxy clustering as it assumes Gaussian initial conditions (Donnert, 2013). However, from observations, it was found that this formalism under-predicts the abundance of low mass halos and overestimates the number of high mass halos (Foot and Vagnozzi, 2016). Nowadays, the Press-Schechter mass function is used to roughly obtain an analytical estimate of the mass function. Recently, the N-body simulations have been used to formulate a more accurate mass function. By means of larger and more detailed N-body simulations, it has been found that the mass function determined for a wide range of redshifts and cosmological models can be fitted accurately by a universal function (Jenkins et al., 2001; Warren et al., 2006; Tinker et al., 2008)

The mass function is a powerful probe of cosmological models. The cosmological parameters can be related to the mass function through σ_M which depends on the matter power spectrum and the linear perturbation growth factor. It is also sensitive to the cosmological parameters at high mass and redshift, hence, it can constrain cosmological models on these scales.

2.2.3 Observables and Scaling Relations

The observed galaxy clusters often have a mass range of $10^{13} - 10^{15} M_{\odot}$ and have a diameter of $\sim$1 Mpc. Using the Bautz-Morgan classification (Bautz and Morgan, 1970), galaxy clusters can be grouped into three types. Type I clusters are dominated by the brightest cluster galaxy that is centrally located. Type II clusters contain bright galaxies that are in the intermediate phase, progressing to being elliptical galaxies. Type III clusters have no dominant clusters. Galaxy clusters are made up of 2-5% galaxies, 11-15% intracluster medium and 80-87% dark matter halo. Galaxy clusters can be observed at different wavelengths of the electromagnetic spectrum. Each wavelength reveals valuable information about the formation and evolution of the galaxy clusters and distribution of dark matter halos. At radio wavelengths, galaxy clusters can be observed via the SZ effect. At millimeter wavelengths, high-density regions within galaxy clusters can cause distortions in the CMB spectrum by inverse Compton scattering, and this is known as the SZ effect (Sunyaev and Zeldovich, 1970). The low energy CMB photons enhance their energy due to collisions with higher energy ICM electrons. This causes a local frequency dependent shift in the CMB spectrum when observed through a galaxy cluster. This effect can be used to detect the galaxy clusters with no redshift limitations by integrating the SZ effect along the line of sight, a quantity which is known as the Y-parameter. The Y-parameter is mathematically defined in terms of the line-of-sight-distortion

$$y = \int \frac{k_B T_x(l)}{c^2 m_e} n_e(l) \sigma_T dl, \tag{2.15}$$

where T_x is the X-ray temperature, m_e is the electron mass, $n_e(l)$ is the electron number density along the line of sight and σ_T is the Thompson cross-section. The actual measured SZ quantity Y_{sz} is measured across the galaxy cluster area dA

$$Y_{sz} = \int y dA. \tag{2.16}$$

The leading surveys that have used the SZ effect to select galaxy clusters are the ACT survey (Hasselfield et al., 2013), the SPT survey (Reichardt et al., 2013), and the Planck survey (Planck Collaboration et al., 2013).

At optical wavelengths, galaxy clusters are selected based on overdensities of galaxies on the sky. Optically selected catalogs are biased towards bright clusters since they are

flux limited, this directly implies that these catalogs are also redshift limited (Abell, 1958; Zwicky et al., 1968). Another selection technique is based on the overdensity of red galaxies which populate the well-evolved galaxy clusters. This selection technique takes advantage of the fact that cluster galaxies tend to stand out in the colour-magnitude diagram because they appear in a "red sequence". The leading survey at optical wavelengths is the Sloan Digital Sky Survey (Abazajian et al., 2009).

The X-ray extended emission from hot ICM in galaxy clusters is used to detect clusters in X-ray surveys. These surveys can be limited in surface brightness and sources that are too diffuse or too faint are often missed. The X-ray cluster selection surveys were the first surveys used to search for the non-thermal diffuse radio emission, associated with the ICM. Many surveys have been developed with the main aim of constructing spectroscopic or photometric galaxy cluster catalogs. The Uhuru X-ray satellite was the first satellite used to carry out an X-ray all-sky survey (Giacconi et al., 1972). The ROSAT satellite, launched in 1990, allowed a significant step forward in X-ray surveys of clusters(Voges et al., 1999). Two powerful and currently active X-ray missions, NASA's Chandra X-Ray Observatory (Giacconi et al., 2002) and ESA's X-Ray Multi-Mirror (XMM) Newton (Watson et al., 2009), are performing some of the deepest and widest X-ray surveys ever undertaken.

One of the most important properties of galaxy clusters is the correlation between the different observable integrated quantities such as the Y_{sz} parameter and the observable quantities such as the thermal properties within a radial range, which are known as scaling relations. Scaling relations are weakly sensitive to the cluster's dynamical state. The scaling relations alone cannot determine whether the cluster is relaxed or unrelaxed. Kravtsov and Borgani (2012) showed that both relaxed and unrelaxed clusters showed the same scaling relation between X-ray luminosity and the integrated SZ parameter. The following are some of the different scaling relations that have been intensively studied: The total mass of galaxy clusters (or its proxies) and bolometric luminosity, the gas temperature and X-ray luminosity and the total mass and integrated SZ parameter (Kaiser, 1986; Ettori et al., 2010; Czakon et al., 2015).

2.2.4 Cluster Mergers

Galaxy clusters accumulate mass by accreting neighbouring clusters (Berrington and Dermer, 2002). Gravitational forces drive the interaction between the merging systems. These

cluster mergers are believed to be the most energetic events in the universe since the Big Bang as they can release $\gtrsim 10^{64}$ ergs in gravitational binding energy (Randall et al., 2016). During a merger as the plasma clouds of each cluster pass through each other, they are affected by ram pressure causing them to slow down. Individual galaxies in the cluster largely do not collide during the merger but are primarily affected by tidal interactions. During cluster mergers, the ICM sound speeds are ≈ 1000 kms^{-1}. These speeds cause shock formation at the interaction boundary of the merging systems (Sarazin, 2004). X-ray images of merging galaxy clusters show distinctive substructure and other features such as 'cold fronts' and 'cool trails' which are associated with 'post shock' gas. There are different categories of mergers but the most physically intriguing are the dissociative mergers. These mergers occur when the ICM of a merging subcluster experiences sufficient ram pressure forces to displace it from the gravitational potential minimum of its dark matter halo. One spectacular example is the Bullet Cluster, shown in figure 2.1 (Markevitch et al., 2004; Springel and Farrar, 2007). For this type of merger, the absence of an observed separation between the dark matter and stellar components in the Bullet Cluster can be used to place upper limits on the cross-section for dark matter scattering (Spergel and Steinhardt, 2000; Robertson et al., 2017). The most interesting aspect of cluster mergers is that they disturb the ICM, hence, they are a useful probe for ICM plasma physics, cluster scaling relations, the growth of large-scale structure and non-thermal particle populations. Some of the energy released during mergers re-accelerate electrons in the ICM to relativistic speeds and since there are magnetic fields present in the ICM, this causes non-thermal diffuse radio emission in the form of synchrotron radiation.

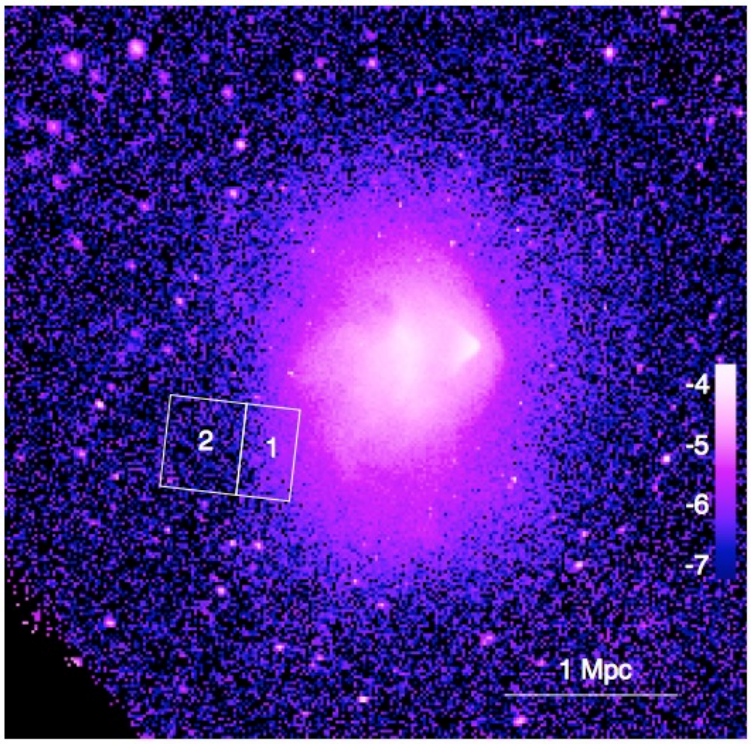

Figure 2.1: The colour scale image of the bullet cluster 1E 0657-55.8 made from 500 ks of Chandra data. The data is taken from the 0.8-4 keV band and binned to have a pixel size of 3.936″. This image has units of $\log(S_x/[\text{Counts/s/arcsec}^2])$. The regions labeled one and two have a difference in temperature. Source: (Shimwell et al., 2015)

2.2.4.1 Thermal and Non-Thermal Emission in the ICM

The emission in the intracluster medium can be divided into thermal or non-thermal categories. The thermal radiation, for example, the bremsstrahlung radiation, results from particles that are in thermal equilibrium and can be described by a Maxwellian distribution (Dicke, 1954). The thermal emission in the ICM has been intensively studied and it is well understood. The anti-correlation between cooling core galaxy clusters and galaxy clusters undergoing strong mergers is an example of a thermal property that is observable (Jacob and Pfrommer, 2016). Heating and compression associated with mergers can produce a large temporary increase in X-ray luminosity and temperature. There is a lot of thermal activity that results in observables that can be used to characterize galaxy clusters. A number of observational lines of evidence, based on X–ray measurements of gas density (Croston et al., 2008) and temperature profiles (Leccardi and Molendi, 2008; Pratt et al., 2007; Vikhlinin et al., 2006), and the combination of the two to obtain an entropy profile (Cavagnolo et al., 2009), reveal that clusters exhibit different behaviours in central regions, depending on the presence and prominence of cool cores. Galaxy clusters are classified as having cool cores

if the intracluster medium in the center of the clusters is so dense that the cooling time of the gas is much shorter than the Hubble time (Hudson et al., 2010). These central region behaviours have also been linked to merger activity. Cool core clusters have been found to be present in dynamically relaxed clusters, while unrelaxed, merging clusters do not contain cool cores.

Non-thermal diffuse radio emission is continuum radiation from high-energy particles that are not in thermal equilibrium and hence, can not be described by a Maxwellian distribution. This non-thermal emission arises from synchrotron radiation in the ICM. Non-thermal diffuse radio emission is not a well-understood phenomenon, however, in the past few years, there have been studies trying to understand the link between thermal emission and non-thermal diffuse radio emission (Sarazin, 2004). These studies enhance our understanding of galaxy clusters because non-thermal diffuse radio emission gives us a different view of the ICM. Some of the most studied non-thermal diffuse radio sources are GRHs and radio relics. The formation of these observables is still a much-debated issue and will be further discussed in the following sections. Diffuse radio emission is not the only evidence of non-thermal activity in the intracluster medium, other important evidence includes the detection of excess emission of hard X-Ray (HXR) in galaxy clusters (Brunetti, 2004a).

2.2.5 Future Surveys

The existence of non-thermal diffuse radio emission in clusters has opened up an exciting area of study both in cosmology and astrophysics. Presently we do not doubt the existence of non-thermal diffuse radio emission, however, there are still many questions open questions on the formation of the non-thermal diffuse radio emission and its evolution. To answer these questions, radio telescopes that have high angular resolution and that can map a large area of the sky simultaneously, are required. These astronomical instruments will be able to observe galaxy clusters at high redshift and low mass. These are the currently unexplored parameter spaces. Next generation telescopes are designed to answer both cosmological and astrophysical questions. The leading future surveys, at radio wavelengths, are the SKA telescopes including its pathfinders such as the Australian Square Kilometer Array Pathfinder and the MeerKAT telescope, the upgraded Giant Meterwave Telescope (uGMRT), and the Low-Frequency Array (LOFAR) phased array project.

The LOFAR survey is designed to answer some of the open questions in radio astronomy

such as the formation of massive galaxies in the epoch of reionization and the magnetic fields and shocked hot gas association within bound clusters (Röttgering et al., 2011). The LOFAR telescope will be able to detect diffuse radio emission up to the cluster formation epoch. This will answer many questions with regards to the evolution of shocks and magnetic field in clusters. The spectrum of radio emission in galaxy clusters provides us with essential information on the energy and physics of the relativistic particles in the ICM as well as the strength and distribution of magnetic fields. The SKA telescope's increased sensitivity to radio emission on cluster scales will allow a detailed analysis of the polarization spectra and brightness distribution of the diffuse radio emission (Acosta-Pulido et al., 2015). With the SKA data and gamma-ray experiments, scientists will be able to constrain the contribution of cosmic-ray protons to the observed diffuse radio emission. These constraints will bring an insight into the formation of diffuse radio sources such as radio halos and relics, hence, ruling out or providing further evidence for their formation models.

2.3 Diffuse Radio Emission in Galaxy Clusters

Galaxy clusters play a vital role in probing dark energy, hence, it is important to understand how they form and evolve. Their formation and evolution are directly linked to the intracluster medium (ICM). Therefore, we need to have an understanding of the thermal and non-thermal components of the ICM. The thermal components are well understood and their observable properties are well modeled. However, the non-thermal components still need a great development in their formation models. These non-thermal components in the form of diffuse radio sources are allocated into three groups: giant radio halos, radio mini-halos, and radio relics.

2.3.1 Giant Radio Halos

Giant radio halos are central, extended over Mpc scales, unpolarized and have steep[†] spectra. This radio emission has no optical counterparts hence; it is not associated with individual galaxies but the intracluster medium, an example of a GRH is shown in figure 2.2. Detailed observations indicated that radio halos are spatially restricted to hot merger-shocked regions (Cuciti et al., 2015).

[†]spectral index $\alpha \geq 1.15$

The difficulty in explaining the source particles of GRHs arises from the combination of their Mpc size and the relatively short radiative lifetime of the radio emitting electrons. The diffusion time of relativistic electrons to spread over the Mpc scale exceeds their radiation lifetime by two orders of magnitude ($10^{10} - 10^{8}$ years) (Venturi, 2011). This is known as the 'diffusion problem'. To overcome the diffusion problem, a mechanism is required to re-accelerate particles with an efficiency comparable to the electron losses (Petrosian, 2001), or relativistic particles need to be continually injected into the cluster region (Jaffe, 1977). We introduce the models that explain these mechanisms in the section below.

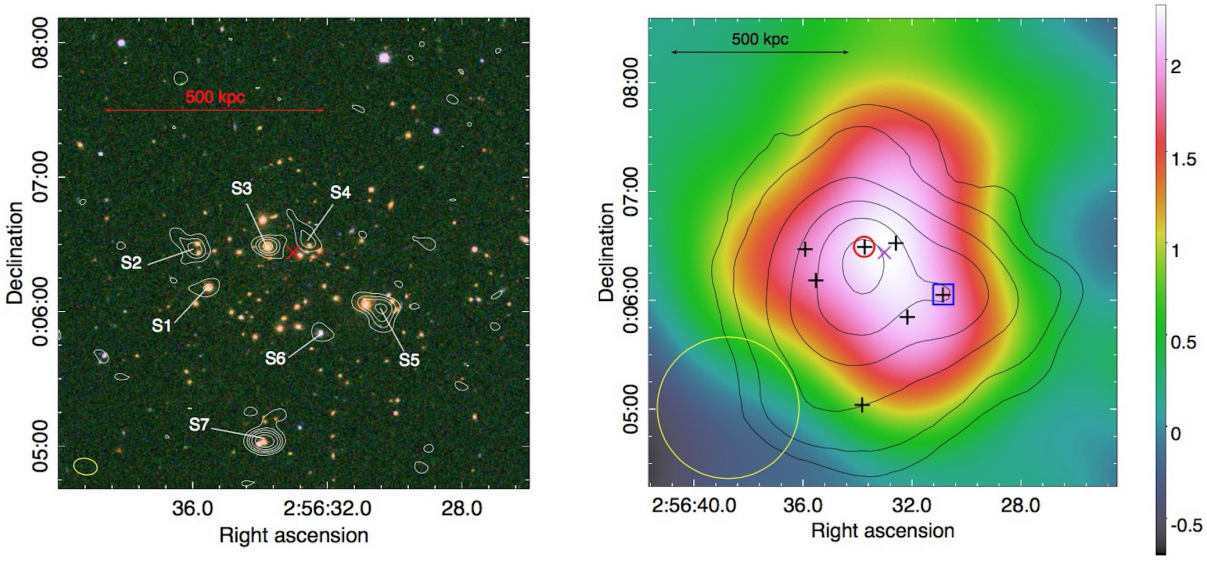

Figure 2.2: A radio halo detection in ACT cluster J0256.5+0006. Left: SDSS image of the θ_{500} cluster region with contours of high-resolution emission detected in cluster region using GMRT at 610 MHz, beam size ($6.5'' \times 5.0''$), 1σ noise level corresponds to 31 μJy beam^{-1}. Right: a low-resolution image of the θ_{500} cluster region with XMM-Newton MOS X-ray contours with arbitrary levels. LR image has beam size ($79.6'' \times 76.8''$). The red circle and blue square show the bright cluster galaxy of the main subcluster component. Source: (Knowles et al., 2016)

2.3.1.1 Giant Radio Halo Formation Theories

Hadronic model

Protons that have relativistic speeds in the ICM have very long life-spans ($\sim 10^{14}$ yrs), these protons remain confined in galaxy clusters for a Hubble time (Donnert et al., 2010). As a result, these Cosmic Ray protons (CRp) are expected to be the dominant components of the non-thermal diffuse radio emission in galaxies. The hadronic secondary electron model is based on this theory. In this model, the origin of giant radio halos (GRHs) is associated with the collision of CRp with thermal protons. Collisions between these protons in the

ICM generates secondary particles that combined with the primary relativistic particles are expected to produce relativistic electrons. The possible mechanisms for the CRp injection in the ICM include shock waves caused by cluster accretion and mergers, outflows from radio galaxies with Active Galactic Nuclei (AGN) and supernova-driven winds. Simulations have derived direct constraints on this model (Donnert, 2013). The following are the observational properties from simulations of cluster-wide radio bright populations of Cosmic Ray electrons (CRe):

1. Radio emission predicted from simulations should be consistent with the observed profile.

2. Non-thermal pressure caused by the CRp, magnetic field, and turbulence should not exceed the non-thermal pressure constraint from X-rays.

3. The population of old CRp or CRe with very steep spectral index should be located in clusters with an ultra-steep spectrum.

4. Gamma-rays should be detected as a by-product of the collision of CRp with thermal protons.

Observations do not align with the theoretical predictions of the hadronic models as there has been no gamma-ray detection and the hadronic models fail to simultaneously reproduce observables such as the GRH bimodality and the ultra-steep spectrum (USS). The hadronic model simulations also predict that most of the massive clusters should possess GRHs and since their lifetime is comparable with the Hubble time, one would expect that 70% of massive clusters should host GRHs (Kuo et al., 2003), however, observations show that only 30% of massive clusters host GRHs.

Re-acceleration model

A promising model for the formation of the GRHs is the turbulent re-acceleration model. This model assumes a reservoir of pre-existing relativistic particles. These particles could be from AGN relativistic jets or left over during large-scale structure formation. In this model, the gravitational potential energy released during a cluster merger is directed to re-accelerating these electrons. Once the electrons have speeds that are high enough they will emit synchrotron radiation that is luminous at radio wavelengths. One of the major observational properties that favours this model is the observed spectral properties of GRHs

(Brunetti, 2011b). This model also predicts a steep spectral index for some of the GRHs. The synchrotron spectrum can be derived from the maximum energy of these re-accelerated electrons

$$E_{max} \approx \frac{\chi(E)}{\beta_{rad}}, \tag{2.17}$$

where $\chi(E) = \chi$ for the FERMI mechanism[‡] and $\beta_{rad} = c_1(B^2 + B_{IC}^2)$ is the sum of all the magnetic field components. The maximum frequency of the radiation from the CRe is

$$\nu_{max} = c_2 B E_{max}^2 \tag{2.18}$$

$$\nu_{max} = \frac{c_2}{c_1^2} \frac{B\chi^2}{(B^2 + B_{IC}^2)^2}, \tag{2.19}$$

where c_1 and c_2 are constants obtained when differentiating. This maximum frequency of the cosmic ray electrons, derived in detail by Rybicki and Lightman (1979), can be related to the magnetic fields in the intracluster medium. This maximum frequency is essential for the identification of the origin of CRe. Acquiring flux measurements for the radio sources formed from the synchrotron radiation is important for observing how these objects evolve at different frequencies. The flux S_ν per unit frequency can be written as

$$S_\nu \propto \nu^{-\alpha}, \tag{2.20}$$

where α is the spectral index. The very first observational motivation of the turbulent re-acceleration model was the observed steepened spectra of the Coma cluster radio halo (Willson, 1970). A large number of GRHs have also been observed to be hosted by dynamically disturbed clusters (Venturi et al., 2007).

The observational evidence favours this model. The observed spectrum of radio halos also supports the merger-induced turbulent re-acceleration model, which suggests that many radio halos in the universe should emit at low frequencies (Brunetti et al., 2008). Observations often link the radio emission with dynamically disturbed galaxy clusters. This means that they could be used as tracers of cluster mergers. This relation will, therefore, allow detailed studies of higher redshift cluster formation processes and properties of the accompanying cluster merger shock waves (Enßlin and Röttgering, 2002).

[‡]The mechanism by which cosmic ray electrons and protons achieve a high-energy distribution, also known as diffusive shock acceleration.

Hybrid models

Although the observations favour the re-acceleration model, none of the previously explained models fully describe the observational characteristics of GRHs. To account for these unexplained characteristics, (Miniati et al., 2001) proposes hybrid models. These models combine aspects from both the hadronic model and the re-acceleration model. Hybrid models suggest that the observed radio halos can evolve from the re-acceleration of both primary and secondary electrons by magnetohydrodynamic turbulence.

The relative contributions of primary and secondary electrons to the total re-accelerated particle population are constrained by the observed properties of the radio emission. Some constraints have been derived by Brunetti and Blasi (2005); Brunetti and Lazarian (2011).

2.3.1.2 Observational Properties

The presence of GRHs shows that there are relativistic particles and magnetic fields that spread across galaxy cluster scales (Venturi, 2011). The spectra of GRHs is important for studying the origin of these relativistic particles and the dynamics of the galaxy cluster hosting the emission. The detection of radio halos and studies of their spectrum has not revealed any similarities in the characteristics of the GRH spectra, instead, there is a spread in spectral index value α. The discovery of ultra-steep spectra, with $\alpha \sim 2$ has further observationally motivated the turbulent re-acceleration model (Macario et al., 2010). This model predicts the presence of such spectra in some GRHs. The size of some of these GRHs with ultra-steep spectra significantly increases with decreasing frequency. This significant increase is not observed in the radio halos with $\alpha \sim 1.2$ to 1.4 as the sizes of these halos do not appreciably change with decreasing frequencies. Observing more GRHs of this kind will help in developing a more accurate formation model.

One prominent observation of GRHs is that they are mostly found in X-ray luminous, dynamically disturbed systems and this observational property has led to the conclusion that this emission is related to cluster mergers. Since this X-ray luminosity seemed to have a positive correlation with GRH existence it has been used to select cluster candidates hosting GRH. However, there is a bimodality that has been observed: clusters that are radio loud and host a GRH had a radio power that correlated positively with X-ray luminosity but those that are radio quiet do not show this correlation. Brunetti and Cassano (2010) explains this bimodality as a transition phase in clusters. They argue that galaxy clusters

host GRHs for a certain period of time and during this time the cluster is hydrodynamically active. As the cluster moves into a more dynamically relaxed state the radio emission is gradually suppressed and then these clusters populate the radio quiet group.

The aforementioned bimodality was thought to have disappeared when comparing radio power to integrated SZ signal (Basu, 2012). The reason given was that the SZ measure allows an unbiased estimate of cluster mass whereas the X-ray selected cluster samples are biased towards detecting clusters that have bright cool cores, hence, they exhibited the bimodal behaviour. However, recent findings in Cassano et al. (2013), where a complete sample of SZ-selected clusters was studied, indicated a bimodal behaviour that is similar to the X-ray luminosity. These findings further support the turbulent re-acceleration model, in which the bimodality arises from the transition of clusters from dynamically unrelaxed to relaxed states. However, further studies need to be done to ensure that the bimodality is indeed observed in the SZ-selected sample.

2.3.1.3 Scaling Relations

Since the discovery of giant radio halos, there have been studies of the relation of non-thermal diffuse radio emission and thermal emission. A decade ago Liang et al. (2000) found a strong correlation between the radio halo power and the X-ray temperature. This led to further statistical analysis of the radio halo power and its correlation with global cluster properties. These studies revealed that there is indeed a correlation between the radio halo power and X-ray luminosity, X-ray temperature, integrated SZ signal and cluster mass (Venturi, 2011). Cassano did further analysis of galaxy clusters at 1.4GHz to quantify these correlations (Cassano, 2010; Cassano et al., 2013). These studies found that clusters hosting GRHs showed an overall positive radio halo power and X-ray luminosity correlation, given by $\mathrm{P}_{1.4\mathrm{GHz}} \propto \mathrm{L}_{\mathrm{X}}^{\beta}$. However, there exists a scatter within the clusters hosting radio halos, for example, some radio halos with ultra-steep spectra are outliers and they lie below the correlation margin. The integrated SZ signal at R_{Δ} also showed a positive correlation $P_{1.4\mathrm{GHz}} \propto Y_{\mathrm{SZ}}^{\beta}$. The scaling relations will be probed further as the radio halo population increases and as more powerful telescopes are built that will observe clusters with low mass and high redshift.

2.3.1.4 Giant Radio Halos as Probes of Cluster Mergers

Multiwavelength studies of GRHs have shown that it is only dynamically disturbed clusters that host these diffuse radio sources (Venturi et al., 2009). These studies show that X-ray images of host clusters exhibit substructure and are morphologically disturbed. These observational properties are the primary motivation for using GRHs as a probe for cluster mergers. The observed bimodality also associates the presence of radio halos with cluster mergers. The galaxy clusters that do not host GRHs are found to be dynamically relaxed and associated with post-merger systems. Cassano et al. (2010) were the first to quantify this relation by intensive statistical analysis of the cluster substructure using a complete sample of deep radio observations and X-ray data. They studied the radio halo power, centroid shift[§] and X-ray brightness concentration parameter. From these studies, they derived that indeed there was a connection between cluster mergers and the presence of GRHs. It remains to be investigated whether, or not, GRHs can probe the cluster merger rate and evolution (Cassano et al., 2016).

2.3.2 Radio Mini-Halos

The morphology of radio mini-halo is similar to that of giant radio halos, however, contrary to GRHs this emission is found in clusters that are dynamically relaxed. Radio mini-halos spread over 100-500 kpc, have steep radio spectra and are centered in cool-core clusters (ZuHone and Markevitch, 2012). It has been discovered that clusters hosting radio mini-halos often have radio-loud active galactic nuclei (AGN) with cooling outflows (Gitti et al., 2014). Although these central galaxy activities shoot out electrons at relativistic speeds (CRe) their lifetime ($\sim 10^8$ yrs) does not allow them to spread to kpc scales. Another mechanism is needed to produce the observed radio emission. Similarly to the GRHs, the two prevailing formation theories are as follows: i) Secondary particles generated by inelastic collisions between relativistic cosmic ray protons and thermal protons. ii) Existing electrons deposited by AGN activity are re-accelerated by turbulences in the core region of the intracluster medium. Magnetohydrodynamic (MHD) simulations and observation seem to favour the latter theory. Clusters hosting radio mini-halos, shown in figure 2.3, have also been found to host 'cold fronts' which are an indication of cluster turbulence. There have also been discoveries of positive correlations between radio luminosity of mini-halos and

[§]The shift in the central position of a galaxy cluster due to merger activity.

the cooling flow power. These characteristics are associated with turbulent activity (Bravi et al., 2015). Although the observational evidence seems to favour the second theory, the first theory has not been completely ruled out.

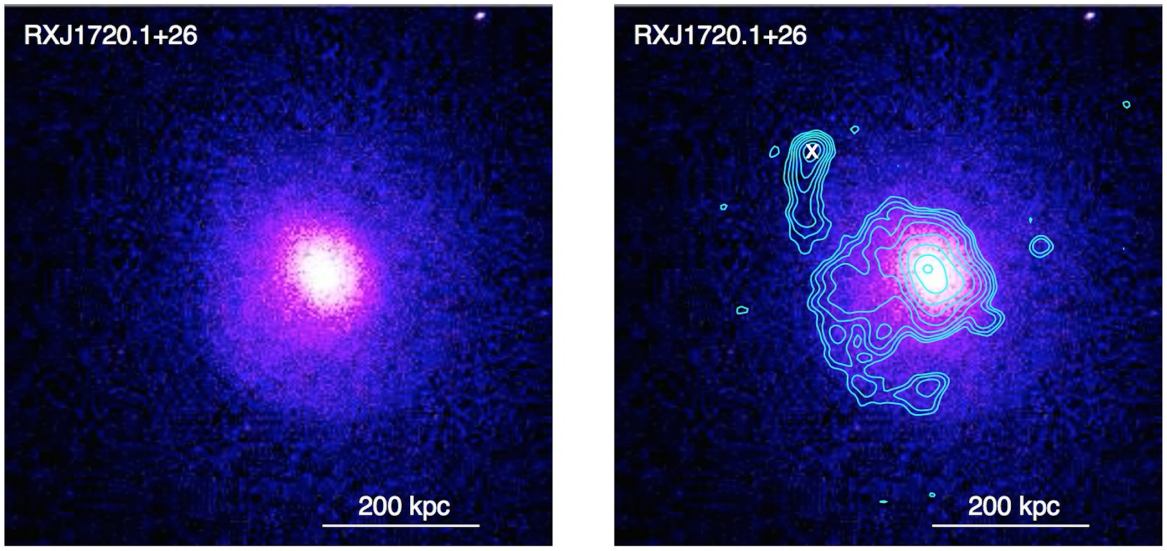

Figure 2.3: A detection of a mini-halo in cluster RXJ170.1+26. The image on the left shows a Chandra X-ray image of the cluster. Source: (Mazzotta and Giacintucci, 2008). The image on the right indicates the mini-halo detection contours obtained using GMRT at 610 MHz. The beam size is ($8''\times 6''$), 1σ noise level corresponds to 30 μJy beam^{-1} and the cross indicates a head-tail source that is not related to the mini halo. The detected contours, when overlaid on the X-ray image, show that the cluster is confined to the cold front region. Source: (Giacintucci et al., 2012)

2.3.3 Radio Relics

Radio relics, another form of diffuse radio sources in clusters, are elongated highly polarized radio sources that are often found on the outskirts of the cluster regions. The polarized property of radio relics makes them a good probe of magnetic fields associated with the peripheries of clusters. There is no distinct formation theory at the moment, however, from theoretical simulations and observations, there are two model candidates. In the first model, it is assumed that the relativistic electrons are produced by the diffusive shock acceleration of thermal electrons due to Fermi-I processes (Hoeft and Brüggen, 2003). The second model states that radio relics are a result of the revival of fossil cocoon-like remnants of lobes from radio galaxies or AGN that, over time, became inactive. The electrons of these remnants are re-accelerated by adiabatic compression that results from merger shock waves (Kale and Dwarakanath, 2009). Three-dimensional MHD simulations favour the existence of fossil radio plasma (Enßlin and Brüggen, 2002), a simulation of the evolution of a radio relic is

shown in figure 2.4. From observations, it has been found that radio relics are associated with merger shock fronts (Kang and Ryu, 2016). Both these findings favour the second model. The association of radio relics and merger shock waves has raised the question of common origins of radio halos and radio relics. The discovery of clusters hosting both the central emission and the peripheral polarized emission has further perpetuated the belief that these two radio sources are of common origin.

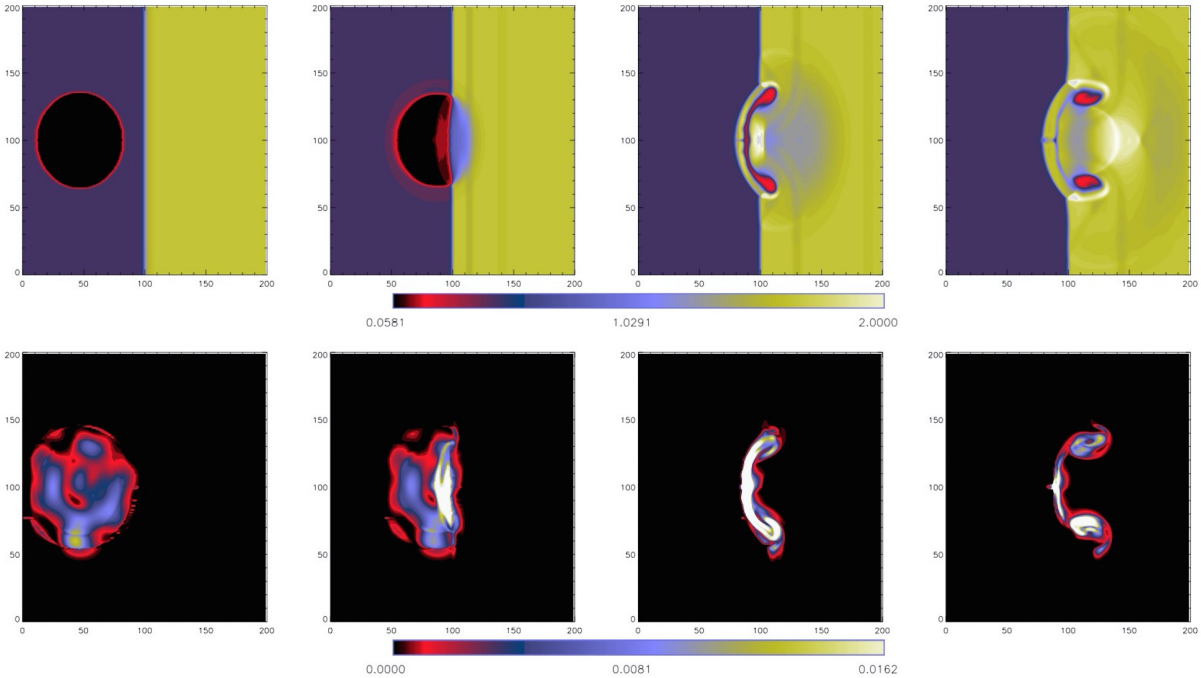

Figure 2.4: This is a simulated image showing the evolution of radio relics from the initial set up before the merger-induced shock on the left to the image obtain in the final post-shock stage (right). The top panel shows the simulated magnetic field energy density. The bottom panel indicates a central slice through the simulation volume. Source: (Enßlin and Brüggen, 2002)

Although classically radio relics were associated with a peripheral elongated morphology, recent studies have found that this is not an exclusive morphology. Giovannini and Feretti (2004) conducted a study on the different shapes and positions of radio relics. In the study, it was found that some radio relics were circular in shape and found in the peripheral region of the cluster (Govoni et al., 2001). The circular shape could emanate from elongated sources that have been extended to disk shapes that are now observed in projection. Other relics were rather situated towards the inner region of the cluster and found to be near first-ranked galaxies although not directly associated with the individual galaxies themselves. These were associated with the remnants of radio lobes from a previously active galactic nuclei (Slee et al., 2001). Another class of relics was found to be elongated but at a much

further distance from the cluster region (Harris et al., 1993; Giovannini and Feretti, 2000). It was concluded that these are associated with the filamentary structure of superclusters (Bagchi et al., 2002; Linden et al., 2011). The next generation telescopes will discover many more radio relics which will broaden the statistical studies of these sources and help clarify their origin and evolution.

CHAPTER 3

Analysis Methods

In 1933 Jansky (1933) detected radio signals from outside the atmosphere using his single dish antenna. His discovery opened up a new branch in astronomy called 'radio astronomy'. This research area has vastly increased our understanding of the universe. Radio astronomy provides an alternative look at the universe through radio wavelengths. Radio wavelengths are much larger than optical and X-ray wavelengths, hence, a telescope with a larger diameter is needed to achieve angular resolution as good as optical telescopes. Angular resolution is given by $\theta = \frac{\lambda}{D}$, where λ is the observing wavelength and D is the diameter of the telescope. To increase angular resolution one needs to either decrease the observing wavelength or increase the diameter of the telescope. The telescope's dish diameter can be increased up to $\sim$100 m because the telescope's dish has to be steerable, hence, this constrains the dish diameter.

Radio interferometry is the solution to having a larger aperture and also has economical advantages. The idea of interferometry has been around for centuries. In 1921 the first optical interferometer was introduced, called the Michelson Stellar Interferometer (Michelson and Pease, 1922). It introduced the technique of using two spaced receiving apertures and measuring the fringe amplitude to determine the angular width. This method was then implemented on radio telescopes. In 1946 Ryle and Vonberg built a dipole array radio interferometer to investigate the cosmic radio emission (Ryle and Vonberg, 1946). Ryle (1952) introduced the phase-switching interferometer which removed unwanted components of the

receiver output and left only fringe oscillations. The Lloyds Mirror (Sea) interferometer introduced by Bolton et al. (1949) received radiation from sources rising over the horizon both directly and by reflection from the sea. Methods of advancing radio interferometry are still being investigated even to this day. The new generation telescopes, such as LOFAR (van Haarlem et al., 2013) and the SKA (Acosta-Pulido et al., 2015) will tackle questions in astronomy that have been around for decades.

3.1 Interferometry and Aperture Synthesis

To simplify large interferometric arrays we regard them as a collection of two element interferometers. To understand how the two element interferometer works we use the analogy of Young's double-slit experiment (Young, 1801). A single wavelength source of light passing through two slits will diffract and produce a fringe pattern of maxima and minima at an angular distance $\frac{\lambda}{D}$ apart. The phase difference between the waves will change as the path lengths of the directed light source vary, giving rise to the constructive and destructive interference. Interferometers use the same concept. Let us consider an interferometer composed of two antennas, as illustrated in figure 3.1. All we can learn from the observed source comes from the distribution of its electric field $\vec{E}$. Each antenna measures a different part of the wavefront arriving from the source. The signals from each antenna are cross-correlated, similar to Young's double-slit experiment. Depending on the path taken and the distance between the antennas, the interferometer will produce constructive or destructive interference. If we add in the Earth's rotation to make the observation realistic, one can imagine a source moving through the interferometer beam, giving positive and negative output, and producing a fringe pattern (Wilson et al., 2009). The more extended the source is, the lower the fringe amplitude. When the fringe amplitude is zero this corresponds to beam smearing, meaning, the source is larger that the beam size. In the following section, we derive the antenna's response, correlator output, noise, and imaging algorithms.

For simplicity let us consider a one-dimensional sky. The wave-front from the observed source in the θ direction reaches the antenna on the right-hand side at time

$$\tau_g = \frac{D}{c} \times \sin\theta \tag{3.1}$$

before it reaches the antenna on the left-hand side. τ_g is defined as the geometric delay. The

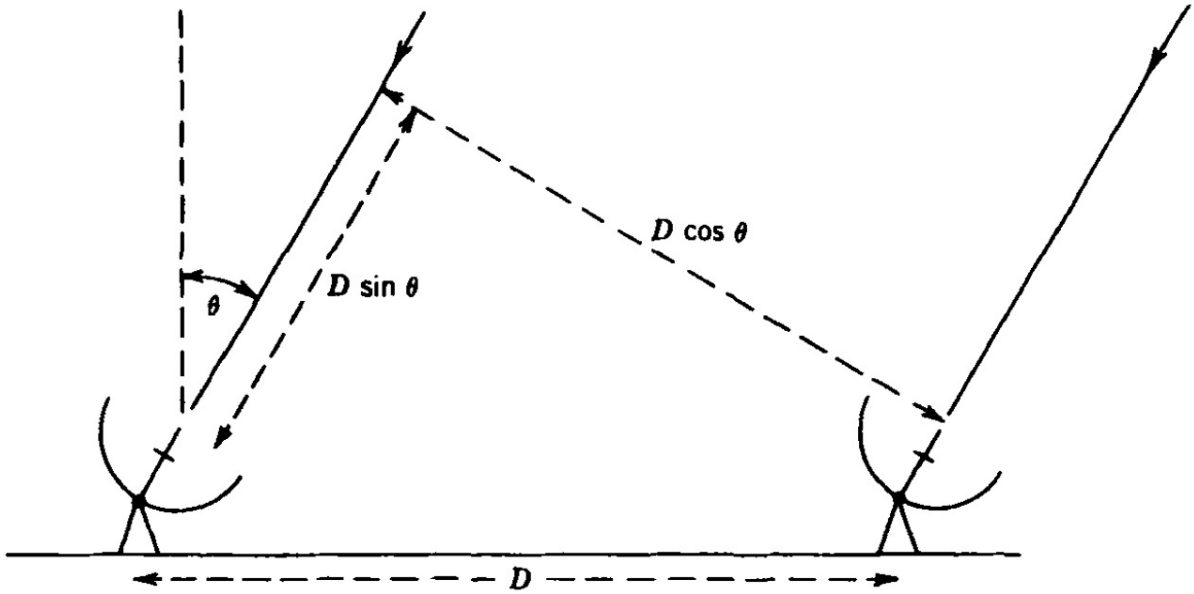

Figure 3.1: A sketch of a two element interferometer.

signals from the two antennas are multiplied, with the output proportional to

$$F = 2\sin(2\pi\nu t)\sin 2\pi\nu(t-\tau_g) \tag{3.2}$$

$$= \cos(2\pi\nu\tau_g) - \cos(4\pi\nu t)\cos(2\pi\tau_g) - \sin(4\pi\nu t)\sin(2\pi\nu\tau_g) \tag{3.3}$$

The terms in this equation that most rapidly vary can be filtered out. This leaves us with the fringe function

$$F = \cos(2\pi\nu\tau_g) = \cos\left(\frac{2\pi Dl}{\lambda}\right) \tag{3.4}$$

where $l = \sin\theta$. This signal multiplication takes place inside a correlator. If the signals at the correlator have uniform power spectral density over the defined bandwidth ($\Delta\nu$) and have central frequency, ν_0, the output becomes

$$F(l) = \frac{1}{\Delta\nu}\int_{\nu_0-\frac{\Delta\nu}{2}}^{\nu_0+\frac{\Delta\nu}{2}} \cos\left(\frac{2\pi Dl\nu}{c}\right) d\nu \tag{3.5}$$

$$= \cos\left(\frac{2\pi Dl\nu_0}{c}\right)\frac{\sin(\pi Dl\frac{\Delta\nu}{c})}{\pi Dl\frac{\Delta\nu}{c}}. \tag{3.6}$$

The second term is identified as the envelope fringe which takes the form of a sinc(x) function

$$\mathrm{sinc}(x) = \frac{\sin(\pi x)}{\pi x}, \tag{3.7}$$

which is the overall pattern of the fringe function. Going back to 3.1, let us assume that for an observed point source each antenna sends equal amounts of voltage V(t) to the correlator. The resulting voltage output from the correlator is

$$r = \frac{1}{2T}\int_{-T}^{T} V(t)V(t-\tau)dt, \tag{3.8}$$

where V(t) is the signal voltage, 2T is the time taken by the correlator to sum the output and $\tau = \tau_g - \tau_i$ is the total time delay, with τ_i is introduced as the instrumental time delay. Since the integration time (2T) is much greater than the inverse of the bandwidth ($\Delta\nu^{-1}$) we can take the limit as T approaches infinity. This gives us the autocorrelation function

$$r(\tau) = \lim_{T\to\infty}\frac{1}{2T}\int_{-T}^{T} V(t)V(t-\tau)dt. \tag{3.9}$$

Another way of interpreting the autocorrelation function is that it is the Fourier Transform of the squared amplitude of the voltage response

$$r(\tau) \leftrightarrows \int_{-\infty}^{\infty} |H(\nu)|^2 e^{j2\pi\nu\tau}d\nu, \tag{3.10}$$

where $H(\nu)$ is the amplitude of the voltage response and $\leftrightarrows$ denotes the Fourier Transform operation. Using a Gaussian bandpass filter, to block unwanted frequencies, centered at frequency ν_0 we can re-write the squared amplitude of the voltage response as

$$|H(\nu)|^2 = \frac{1}{2\sigma\sqrt{2\pi}}\left\{ e^{\left[-\frac{(\nu-\nu_0)^2}{2\sigma^2}\right]} + e^{\left[-\frac{(\nu+\nu_0)^2}{2\sigma^2}\right]} \right\}, \tag{3.11}$$

where σ is the bandwidth factor, which is the range of frequencies the telescope is designed to accept. Considering only the positive frequencies, which are what is realistically observed, the autocorrelation function simplifies to

$$r(\tau) = e^{-2\pi\tau^2\sigma^2}\cos(2\pi\nu_0\tau). \tag{3.12}$$

The envelope function is no longer a sinc function but a Gaussian function. The pattern

produced by the envelope function is referred to as the bandwidth pattern. Minimizing the instrumental delay results in the total time delay being just the geometric time delay and gives the autocorrelation as

$$r(\tau_g) = e^{\left[-2\left(\frac{\pi D\sigma}{c}\sin\theta\right)^2\right]}\cos\left(\frac{2\pi\nu_0 D}{c}\sin\theta\right). \tag{3.13}$$

The bandwidth pattern is a function of the bandwidth factor and the antenna baseline. We can determine the fringe pattern by the behavior of the envelope function. In the generalized case, longer baselines and wider bandwidths result in narrow fringe patterns.

3.2 Interferometer Response in the UV-Plane

We now extend our analysis into two-dimensional space. The interferometers observe the sky in (u,v) coordinates. In this coordinate system (l,m) are the corresponding directional cosines. When an observation is made, a plot of the length and direction of the projected antenna baselines trace the source across the sky and produces an arc of an ellipse in the uv-plane (Thompson et al., 1986). To physically understand the plots produced in the uv-plane we take a two-dimensional Fourier Transform and this results in an intensity distribution across the observed sky.

The mathematical representation of the antenna observations gives us a better understanding of radio observations (Kraus, 1966). Let the center of the observed field be $\vec{s_0}$. The component of the power of the source in the field is $\frac{1}{2}A(\vec{\sigma})I(\vec{\sigma})\Delta\nu d\Omega$ for both antennas, where $d\Omega$ is the component of the sources solid angle, $A(\vec{\sigma})$ the effective collecting area, $\Delta\nu$ is the recievers system's bandwidth and $I(\vec{\sigma})$ the source intensity. The source that is being observed is at position $\vec{s} = \vec{s_0} + \vec{\sigma}$. Expressing the baseline length in terms of wavelength ($\vec{D}_\lambda$) we find that $\nu\tau_g = \vec{D}_\lambda \cdot \vec{s} = \vec{D}_\lambda \cdot (\vec{s_0} + \vec{\sigma})$. With these new parameters we can extend equantion 3.13 and define the two-dimensional correlator output as

$$\begin{aligned} r(\vec{D}_\lambda, \vec{s_0}) &= \Delta\nu \int_{4\pi} A(\vec{\sigma})I(\vec{\sigma})\cos[2\pi\vec{D}\cdot(\vec{s_0}+\vec{\sigma})]d\Omega \\ &= \Delta\nu\cos(2\pi\vec{D}_\lambda\cdot\vec{s_0})\int_{4\pi} A(\vec{\sigma})I(\vec{\sigma})\cos(2\pi\vec{D}_\lambda\cdot\vec{\lambda})d\Omega \\ &- \Delta\nu\sin(2\pi\vec{D}_\lambda\cdot\vec{s_0})\int_{4\pi} A(\vec{\sigma})I(\vec{\sigma})\sin(2\pi\vec{D}_\lambda\cdot\vec{\sigma})d\Omega. \end{aligned} \tag{3.14}$$

This is the output of the correlator for radiation from a source in the direction $\vec{s}$. In the

above we have assumed that the waveforms radiated from different source elements $d\Omega$ are of uncommon origin, hence, uncorrelated. This assumption holds true for all cosmic radio sources.

To obtain the complex visibility function we normalize the reception pattern and multiply it with the intensity distribution;

$$\mathcal{V} = |\mathcal{V}|e^{j\phi_\nu} = \int_{4\pi} A_N(\vec{\sigma})I(\vec{\sigma})e^{-j2\pi\vec{D}_\lambda\cdot\vec{\sigma}}d\Omega. \tag{3.15}$$

The complex visibility function is a mathematical model of the antenna response in the uv-plane and gives us a useful relationship between the source brightness and the response of an interferometer (Berger and Segransan, 2007). Separating the real and the imaginary components gives us

$$\int_{4\pi} A(\vec{\sigma})I(\vec{\sigma})\cos(2\pi\vec{D}_\lambda\cdot\vec{\sigma})d\Omega = |\mathcal{V}|\cos\phi_\nu \tag{3.16}$$

$$\int_{4\pi} A(\vec{\sigma})I(\vec{\sigma})\sin(2\pi\vec{D}_\lambda\cdot\vec{\sigma})d\Omega = -|\mathcal{V}|\sin\phi_\nu. \tag{3.17}$$

We can now express the correlator output in terms of a fringe pattern that arises when a point source in the direction $\vec{s_0}$ is observed. This correlator output is known as a 'Complex Correlator' which is a correlator which produces both 'Real' and 'Imaginary' parts – or the Cosine and Sine fringes. The corresponding output is

$$r(\vec{D}_\lambda, \vec{s_o}) = A_0\Delta\nu|\mathcal{V}|\cos(2\pi\vec{D}_\lambda\cdot\vec{s_0} - \phi_\nu). \tag{3.18}$$

If we have a very large interferometer array, which extends to multiples of kilometers, we need consider that the arrays will not all lie at the same altitude. This consideration introduces a 3D plane. Extending the uv-plane into 3D we add the 'w' term which is in the direction $\vec{s_0}$;

$$\vec{D}_\lambda\cdot\vec{s_0} = w \tag{3.19}$$

$$\vec{D}_\lambda\cdot\vec{s} = (ul + vm + w\sqrt{1-l^2-m^2}). \tag{3.20}$$

Considering a unit sphere centered at $(u, v, w) = 0$, the tracked source element in the uvw-

plane becomes

$$d\Omega = \frac{dldm}{\sqrt{1-l^2-m^2}}, \tag{3.21}$$

where $\hat{n} = \sqrt{1-l^2-m^2}$ is the direction cosine along the $\vec{w}$ axis. To get the intensity of the observed sky we take a Fourier Transform of the observed sky

$$\mathcal{V}(u,v,w) = \int_{-\infty}^{\infty}\int_{-\infty}^{\infty} A_N(l,m)I(l,m) \times e^{-j2\pi[ul+vm+w\sqrt{1-l^2-m^2}-1]}\frac{dldm}{\sqrt{1-l^2-m^2}}. \tag{3.22}$$

If l and m are small enough then $(\sqrt{1-l^2-m^2}-1)w \simeq -\frac{1}{2}(l^2+m^2)$, which reduces equation 3.23 to give us the *visibility equation*

$$\mathcal{V} \approx \mathcal{V}(u,v,0) = \int_{-\infty}^{\infty}\int_{-\infty}^{\infty} \frac{A_N(l,m)I(l,m)}{\sqrt{1-l^2-m^2}} e^{-j2\pi(ul+vm)} dldm. \tag{3.23}$$

If the source being observed is at a very low elevation angle the values of the 'w' term can be very large, thus leading to maximum baseline separations $(D_\lambda)_{max}$. This leads to a synthesized beam that is $\theta_b \approx (D_\lambda)^{-1}_{max}$. This beam results in maximized phase errors

$$\pi\left(\frac{\theta_f}{2}\right)^2 \theta_b^{-1}, \tag{3.24}$$

where θ_f is the synthesized field width. To understand the visibility equation in terms of sky, that is right ascension and declination (α_0, δ_0) we introduce a new coordinate system. In this coordinate system, we rotate the (u,v,w) coordinate system until the w-axis points towards the north pole of a hypothesized sphere. We label these new coordinates with a prime. The visibility equation in 3.23 becomes

$$\mathcal{V}(u',v',0) = \int_{-\infty}^{\infty}\int_{-\infty}^{\infty} A_N(l',m')I(l',m') \times e^{-j2\pi[u'l'+v'm']}\frac{dl'dm'}{\sqrt{1-l'^2-m'^2}}. \tag{3.25}$$

The inverse Fourier transform of the visibility function is known as the van Cittert-Zernike theorem. This theorem states that under specified conditions, the output signal of an interferometer is a Fourier transform of the observed brightness distribution of a source on the sky. Using this theorem and equation 3.25 we get:

$$F(l',m') = \frac{A_N(l',m')I(l',m')}{\sqrt{1-l'^2-m'^2}} = \int_{-\infty}^{\infty}\int_{-\infty}^{\infty} \mathcal{V}(u',v')e^{j2\pi[u'l'+v'm']}du'dv'. \tag{3.26}$$

To relate this equation to the angular position (α_0, δ_0) we perform the following coordinate transformation:

$$l = l', m'' = (m' - \cos\delta_0)\delta_0 \tag{3.27}$$

$$F(l', (m' - \cos\delta_0)\delta_0) \leftrightarrows |\sin\delta_0|\mathcal{V}(u', v', \sin\delta_0)e^{-j2\pi v' \cos\delta_0}. \tag{3.28}$$

Applying this transformation to the van Cittert-Zernike theorem we get

$$\frac{A_N(l', m')I(l', m')}{\sqrt{1 - l'^2 - m'^2}} = \int_{-\infty}^{\infty}\int_{-\infty}^{\infty} \mathcal{V}(u', v' \sin\delta_0)|\sin\delta_0|e^{-j2\pi v' \cos\delta_0} e^{j2\pi(u'l' + v'm')} du'dv' \tag{3.29}$$

$$= \int_{-\infty}^{\infty}\int_{-\infty}^{\infty} \mathcal{V}(u, v)e^{j2\pi(ul + vm'')} dudv \tag{3.30}$$

The van Cittert–Zernike theorem (van Cittert, 1958) has important implications for radio astronomy. With the exception of pulsars and masers, all astronomical sources are spatially incoherent. Nevertheless, because they are observed at distances large enough to satisfy the van Cittert–Zernike theorem, these objects exhibit a non-zero degree of coherence at different points in the imaging plane. By measuring the degree of coherence at different points in the imaging plane of an astronomical object, we can thereby reconstruct the source's brightness distribution and make a two-dimensional map of the source's appearance (Carozzi and Woan, 2009).

3.3 Antennas

The aim of building antenna arrays is to increase the effective resolution and collecting area of radio telescopes resulting in the desired scientific results being achieved. The layout of the antenna arrays can be grouped into two: phased arrays and multi-element interferometers. Phased array signals from each antenna are added in phase before being transferred to a square-law detector. A multi-element interferometer is recognized as a constellation of two-element arrays. The signals from the two-element arrays are correlated in pairs for every possible combination and the outputs are then used to make a map of the brightness intensity distribution. When deciding on array configuration the most important property is the visibility coverage on the uv-plane. Different configurations result in particular advantages. Linear arrays (Tingay et al., 2013) are most useful for observing regions of the sky within about 60° of the celestial poles that need approximately six hours of tracking, this config-

uration produces full two-dimensional coverage. Open-ended array configurations (T, Y) produce the best spatial frequency coverage. One example of a hybrid of such configuration is the Giant Metrewave Radio Telescope (GMRT) (Swarup, 1990). The closed configurations (circle, +) (Bridger et al., 2004) give the most uniform distributions of measurements.

Antennas, constituents of arrays, come in different shapes and sizes. There are dipole antennas, horn antennas, and the most commonly used parabolic antennas. The advantages of parabolic antennas are that the power loss is minimized and they allow for wide frequency coverage. Parabolic antennas have varying focal arrangements (Wilson et al., 2009) with each arrangement having either economical or observational advantages. There are primary focused arrangements, Cassegrain focus, Nay Smith focus and offset Cassegrain focus. The MeerKAT telescope antennas are an example of an offset Cassegrain focus. The main advantage of the offset Cassegrain is that there is no shadowing of the secondary focus, hence, maximizing effective area. The surface accuracy of the parabolic reflectors is very important as small smoothness deviations result in phase variations of the electromagnetic field as it approaches the focal point. The proof of how deviations result in phase variation can be found in Appendix B.

The antenna reception pattern is known as the primary beam. The primary beam pattern from a parabolic telescope dish is similar to that of a diffraction pattern from a double slit experiment. The primary beam pattern has a bright maximum which is the main lobe. It also several smaller maxima, these are known as the side lobes. The side lobes cause distortions in the data, especially when they fall within a radio source such as a point source. This distortion contributes to the antenna temperature (T_A). The side lobe distortions can also result in false radio sources, hence, it is very important to have a well-defined primary beam model so that the pattern can be completely deconvolved (Garrett et al., 1999).

3.3.1 Receivers

In any radio telescope, antennas are followed by receiving systems which further process the raw signal. The signal strength and corresponding antenna temperature, which is incopo-rated in the radiometer equation, play a major role in determining the receiver requirements. The voltage reception pattern of an individual antenna can be represented as a Fourier Transform of the field's distribution aperture $\bar{\mathcal{E}}(X, Y)$, where X, Y are positions within the

antenna aperture

$$V_A(l,m) \propto \int_{-\infty}^{\infty}\int_{-\infty}^{\infty} \bar{\mathcal{E}}(X,Y)e^{j2\pi[\frac{X}{\lambda}l+\frac{Y}{\lambda}m]}dXdY. \tag{3.31}$$

The antenna response directly corresponds to the amount of signal a receiver can process. To convert to the uv-plane, we can also specify the antenna response using $A(l,m)$ instead of the voltage response as

$$V_A(l,m) \approx \sqrt{A(l,m)} \propto |V_A(l,m)| \tag{3.32}$$

$$\hat{V} = \int_{-\infty}^{\infty}\int_{-\infty}^{\infty} E(l,m)\sqrt{A(l,m)}dldm, \tag{3.33}$$

where $E(l,m)$ is the incident electric field. A radio receiver converts signals from a radio antenna into a usable form. The antennas deliver a noise power to the receiver which depends on the background noise from the sky, atmospheric noise, side-lobe noise and the noise from the losses of the antenna. The sensitivity of the radio telescope receiver is defined as the signal which will give a DC-output voltage equal to the effective value of the output fluctuations due to the system noise (Chengular et al., 2003).

In electronics, the noise temperature is a temperature (in Kelvin) assigned to a component such that the noise power delivered by the noisy component is given by,

$$P \approx kTdv. \tag{3.34}$$

Similarly receivers also measure the average noise power. The receivers used to measure the average power of the noise coming from a radio telescope in a well-defined frequency range are called radiometers (Price, 1984). The simplest radiometer consists of four stages in series: a bandpass filter to select the desired range, a square-law detector, integrator and a voltmeter. The ideal radiometer equation for a multi-element array is

$$\sigma \propto \frac{\mathcal{F}T_{sys}}{A_e\sqrt{N(N-1)\Delta\nu_{RF}\tau}}, \tag{3.35}$$

where σ is the theoretical map noise that can be achieved when observing a source for a time of τ using an N-element interferometer with system temperature T_{sys} ($\mathrm{T}_{sys} = \mathrm{T}_{background} + \mathrm{T}_{sky} + \mathrm{T}_{spill} + \mathrm{T}_{loss} + \mathrm{T}_{cal} + \mathrm{T}_{receiver}$), effective antenna gain A_e, and bandwidth $\Delta\nu$. $\mathcal{F}$ is the fudge factor which is determined by comparing ideal results to the integration times

and sensitivities (Chengular et al., 2003). For the GMRT telescope, the fudge factors for various observing frequencies can be found in the users manual. The radiometer equation is mostly used for calculating the integration time for observing radio sources and gives an indication of the expected theoretical noise. It can also be used to indicate the theoretical signal to noise ratio of an observation.

3.3.2 Correlators

Correlators multiply the signal voltage coming in from antennas. The correlator output can be mathematically represented as

$$r(\tau) = V_1(t) \otimes V_2(t) = \lim_{T\to\infty} \frac{1}{2T} \int_{-T}^{T} V_1(t) V_2^*(t-\tau) dt, \tag{3.36}$$

where τ is the time that V_2 signal is delayed and $\otimes$ represents the convolution. Expressing the integral using a convolution gives

$$V_1(t) \otimes V_2(t) = \lim_{T\to\infty} \frac{1}{2T} \int_{-\infty}^{\infty} V_1(t) V_{2^-}^*(\tau - t) = V_1 \otimes V_2^*. \tag{3.37}$$

Moving from the time frame to the frequency frame by taking the Fourier Transform we obtain the Wiener-Khinchin relation

$$V_1(t) \otimes V_2(t) \leftrightarrows \hat{V}_1(\nu) \hat{V}_2^*(\nu), \tag{3.38}$$

with the quantity on the right hand side known as the cross power spectrum. We now represent the correlator output in terms of incident radiation. Multiplying the voltage spectrum $\hat{V}(\nu)$ and by the filter response $H(\nu)$ and taking the Fourier Transform from the frequency domain to the time domain gives

$$V_1(t) = \int_{-\infty}^{\infty} \int_{-\infty}^{\infty} \int_{-\infty}^{\infty} E(l,m) \sqrt{A_1(l,m)} H_1(\nu) e^{j2\pi\nu t} dl dm d\nu. \tag{3.39}$$

The correlator output is thus

$$\begin{aligned} r(\tau) &= \lim_{T\to\infty} \frac{1}{2T} \int_{-\infty}^{\infty}\int_{-\infty}^{\infty}\int_{-\infty}^{\infty}\int_{-\infty}^{\infty} E(l,m)E^*(l,m)\sqrt{A_1(l,m)A_2(l,m)} \\ &\times H_1(\nu)H_2^*(\nu)e^{j2\pi\nu t}e^{-j2\pi\nu(t-\tau)}dldmdtd\nu \\ &= \int_{-\infty}^{\infty}\int_{-\infty}^{\infty}\int_{-\infty}^{\infty} I(l,m)\sqrt{A_1(l,m)A_2(l,m)}H_1(\nu)H_2^*(\nu)e^{j2\pi\nu\tau}dldmd\nu. \end{aligned} \tag{3.40}$$

If the antennas and filters are identical then the correlator output reduces to

$$r(\tau) = \int_{-\infty}^{\infty}\int_{-\infty}^{\infty}\int_{-\infty}^{\infty} I(l,m)A(l,m)|H(\nu)|^2 e^{j2\pi\nu\tau}dldmd\nu. \tag{3.41}$$

The different propagation times of wavefronts result in a difference in path length of $(ul + vm)\lambda$. If V_1 has a larger path length then the correlator output is

$$r = \int_{-\infty}^{\infty}\int_{-\infty}^{\infty}\int_{-\infty}^{\infty} I(l,m)A(l,m)|H(\nu)|^2 e^{-j2\pi(lu+vm)}dldmd\nu. \tag{3.42}$$

The correlator output measures the Fourier Transform of the intensity distribution modified by the antenna pattern. If the intensity and antenna pattern is constant over the bandpass range and the width of the source is much less than the antenna beam the correlator output further reduces to

$$r = \int_{-\infty}^{\infty}\int_{-\infty}^{\infty} I(l,m)A(l,m)e^{-j2\pi(lu+mv)}dudm \int_{-\infty}^{\infty}|H(\nu)|^2 d\nu \tag{3.43}$$

$$= A_0\mathcal{V}(u,v)\int_{-\infty}^{\infty}|H(\nu)|^2 d\nu. \tag{3.44}$$

If the filter response does not change over the bandwidth, the correlator response becomes

$$r = A_0\mathcal{V}\Delta\nu, \tag{3.45}$$

which is the surface area times the visibility coverage times the specified bandwidth. This means that the correlator response is directly proportional to the surface area and the bandwidth of the telescope. Future surveys now try to maximize the correlator response by increasing the surface area of the interferometers and increasing the bandwidth of the telescopes.

3.4 Imaging

The process of converting the visibilities observed in the uv-plane to radio images is called *Imaging*. This process involves sampling of visibilities, calibration of the data and finally deconvolution of the visibilities with the dirty beam to obtain a 'CLEAN' image.

3.4.1 Visibilities

When sampling the visibility function the sampling operation can be represented as multiplication of $\mathcal{V}(u)$ by a series of delta functions (Thompson et al., 1986). Considering the one-dimensional case the sampling operation can be written as

$$\left[\frac{1}{\Delta u}\right] III\left(\frac{u}{\Delta u}\right) = \sum_{i=-\infty}^{\infty} \delta(u - i\Delta u), \tag{3.46}$$

where III is known as the Shah function. The Fourier transform of the Shah function is equivalent to the delta function, hence, we obtain the following result

$$III(l\Delta u) = \frac{1}{\Delta u} \sum_{n=-\infty}^{\infty} \delta(1 - \frac{n}{\Delta u}), \tag{3.47}$$

where n is the dimension of the function. In the l domain the Fourier transform of a sampled visibility is equal to the convolution of the Fourier transform of $\mathcal{V}(u)$, which turns out to be the intensity in the l domain. When one has acquired the sampling function, interpolation is the next step for selecting the desirable visibilities. In this case, we interpolate the sampling function by a rectangular function. In the u domain this corresponds to the convolution of the sampled values with the Fourier transform of a rectangular function, which is a unit area sinc function. The sampling theorem states that if the intensity distribution is non-zero within an interval of width l_w, $I_1(l)$ is fully specified by the visibility function at points spaced by $\Delta u = l_w^{-1}$.

Now let us extend to the two-dimensional uv-plane. The visibility is measured at an ensemble of n_d pairs of points symmetric about the (u,v) origin

$$\mathcal{V}_{measured}(u, v) = W(u, v)w(u, v)\mathcal{V}(u, v), \tag{3.48}$$

where W is the transfer function and w is the weighting function. The measured visibility

Fourier transform is

$$I_{measured}(l,m) = I_{true}(l,m) \otimes b_0(l,m). \tag{3.49}$$

The measured intensity is a two-dimensional convolution of the true intensity and the dirty beam $b_0(l,m)$. The direct Fourier transform of the measured visibility is

$$\sum_{i=1}^{n_d} \left[\mathcal{V}_{measured}(u_i,v_i)e^{j2\pi(u_il+v_im)} + \mathcal{V}_{measured}(-u_i,-v_i)e^{-j2\pi(u_il+v_im)}\right] \tag{3.50}$$

where w_i is the weighting function. For the best signal-to-noise ratio (SNR), the weights should be inversely proportional to the variance, which is given by the Gaussian noise. The most commonly used weightings are natural, uniform and robust weighting. Natural weighting gives constant weights to all visibilities. This weighting gives optimum point-source sensitivity in an image. However, the synthesised beam-shape and sidelobe levels are usually poor. This gives a weight inversely proportional to the sampling density function. This form of weighting minimizes the sidelobe level. However the noise level can be a factor of two worse than natural weighting. The robust (Briggs) weighting is a compromise between natural and uniform weighting. Briggs weighting introduces an algorithm that takes account of the signal-to-noise-ratio of individual points in the assignment of weights and reduces the weighting of noisy points (Briggs, 1995).

3.4.2 Calibration and Deconvolution

Calibration of visibilities is required to remove all instrumental and atmospheric effects. The corrections are applied before the visibilities are combined into an image as the effects are due to single antenna electronics. There need to be corrections for calculable or directly monitored effects. Calibration sources are also used for both calculable and monitored effects. When including the calibration sources we have to re-write the visibility function as

$$[\mathcal{V}(u,v)]_{uncal} = G_{mn}\int_{-\infty}^{\infty}\int_{-\infty}^{\infty}\frac{A_N(l,m)I(l,m)}{\sqrt{1-l^2-m^2}}e^{-j2\pi(ul+vm)}dldm, \tag{3.51}$$

where A_N is the antenna aperture normalized in the direction of the main beam and G_{mn} is the complex gain factor. To calibrate the complex gain factor, an unresolved calibrator

can be used. The measured response is

$$\mathcal{V}_c(u,v) = G_{mn}\mathcal{S}_c, \tag{3.52}$$

where $\mathcal{S}_c$ is the flux density of the calibration source. When calibrating the visibilities of the target source the amplitude and phase are considered separately. The phase calibration of the target source requires subtracting the calibrator phase from the observed phase. Calibration observations require periodic interruption of observations of the target sources. The desirable characteristics of calibration sources are well-measured flux density and defined angular width and position.

After calibrating the observed data using a well known source the next step is self-calibration. This step improves the noise level of the image. Since the self-calibration is more localized it further reduces the artefacts created by side lobes around point sources. In the case of self-calibration the complex antenna gains are regarded as free parameters to be explicitly derived with the intensity. The procedure in self-calibration is to use a least-squares method to minimize the square of the modulus of the difference between the observed visibilities and the corresponding sky model. The sky model indicates the positions and fluxes of point sources in the observing field. These values are usually adopted from existing surveys. The minimized expression is given by

$$\sum_{time}\sum_{m<n} w_{mn}|\mathcal{V}^{meas} - g_m g_n^* \mathcal{V}^{model}|^2, \tag{3.53}$$

where w_{mn} is inversely proportional to the variance of $\mathcal{V}_{mn}^{meas}$, hence, we can rewrite the expression as

$$\sum_{time}\sum_{m<n} w_{mn}|\mathcal{V}^{model}|^2|\chi_{mn} - g_m g_n^*|^2, \tag{3.54}$$

where $\chi_{mn} = \frac{\mathcal{V}^{meas}}{\mathcal{V}^{model}}$. If one is using an accurate model, χ_{mn} is independent of u and v. χ_{mn} values simulate the response to a calibrator and enable the gains to be determined, however, the model's accuracy is very low therefore we have to iterate. In self-calibration, the phases can only be solved up to a constant gradient across the uv-plane. The inverse Fourier transform of the measured visibility is the 'dirty map' I^D due to the unfilled spots

in the uv-plane

$$I^D = (\text{true sky brightness map}) \times (\text{dirty beam}). \tag{3.55}$$

In the case of poor uv coverage, the dirty beam has strong side lobes which make the dirty map hard to interpret. To get the true sky brightness we deconvolve the two functions by taking a Fourier transform of the convolution, which is a product of the Fourier transform of the components. We divide out the Fourier transform of the measured sky brightness and transform back to obtain

$$I^D(l,m) \otimes b_0(l,m) \leftrightarrows \mathcal{V}(u,v)[W(u,v)w(u,v)w_t(u,v)], \tag{3.56}$$

where w_t is the applied taper. The method of deconvolution is applied in the CLEAN algorithm.

3.4.2.1 Deconvolution - The CLEAN Algorithm

The CLEAN algorithm was derived by Högbom (1974). This algorithm provides one solution to the convolution equation by representing the radio sky by a number of point sources in an empty field of view. An iterative approach is used to find the positions and fluxes of these point sources. The final image, known as the CLEAN image, is the sum of the point source components convolved with a CLEAN beam. There are many variations to the CLEAN algorithm such as the Clark algorithm (Clark, 1980) and the Cotton-Schwab algorithm (Schwab, 1984). However, the Högbom algorithm is the most commonly used, so we will describe this algorithm in further detail. The algorithm follows these steps:

1. Find the strength and position of the point source with the brightest intensity in the dirty image.
2. Subtract from the dirty image, at the position of the peak, the dirty beam multiplied by the peak strength and a damping factor.
3. Record the position and the magnitude of the point source subtracted in a model.
4. Go back to the first step unless all the remaining peaks are below the user-specified level. What remains in the dirty image is the residuals.

5. Convolve the point source model with the idealized CLEAN beam.

6. Add the residuals of the dirty image to the CLEAN image formed in step five.

The CLEAN algorithm does have some shortcomings (Högbom, 1974) such as it can not be implemented in extended sources, and in order for it to converge there are a few conditions that have to be met. Another well-known problem is the generation of spurious structure in the form of spots or ripples as modulation on extended features. Even with these shortcomings, it is still the most practical algorithm for deconvolving the dirty image and is widely used in radio astronomy.

3.5 Source Peeling and Atmospheric Modeling

The earth's atmosphere has a large impact on radio astronomy observations. The radio waves traversing through the atmosphere interact with particles along their wave path. The earth's atmosphere consists of multiple layers, with each layer varying in electron density. Electron density is defined as $\int n_e dl$, where n_e is the local electron number density and l is the distance along the line of sight. At the low densities encountered in the further heights of the earth's atmosphere, collisions between particles are very rare. Hence, unlike common astrophysical plasmas, it is possible for gas to remain in an ionized state for long periods of time. The ionized layer of particles is called the ionosphere. The ionosphere (Spoelstra, 1983) is a spherical shell concentric with the Earth. The spherical curvature of the ionosphere causes the waves propagating through it to slightly change direction, as shown in figure 3.2.

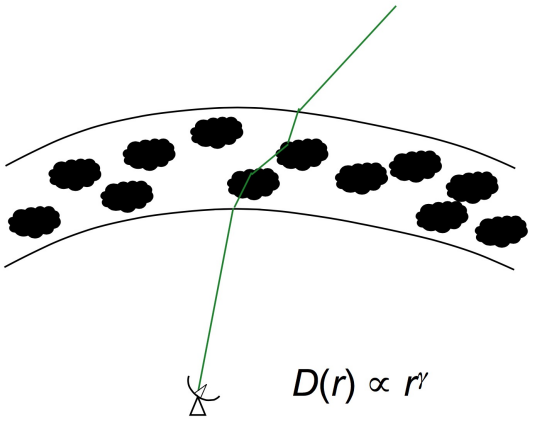

Figure 3.2: A diagram indicating deflection in direction of the radio waves while propagating through the ionosphere.(Erickson, 1984)

Radio waves from a source in the telescope's field of view (FOV) arrive at the receivers of the interferometer having traversed different paths through the ionosphere. These wavefronts acquire different phase delays due to the non-uniformity in the electron density (Loi et al., 2015). This means that a wavefront that was initially planar can be distorted. These phase shifts, that can go up to 4-5 percent, cause difficulty in radio observations and lead to various errors. Very often ionospheric effects cause a shift in source position and change the sources in angular size. The position shift affects the astrometric accuracy of radio astronomical observations. The degradation of astrometry can lead to incorrect source identification compared to sources at higher frequencies such as optical frequencies. Although night observations may reduce ionospheric effects they do not completely get rid of them.

Lonsdale (2005) gives a brief discussion of the different ionospheric calibration regimes that arise due to various interferometer setups. His discussion is best summarized by the image in figure 3.3.

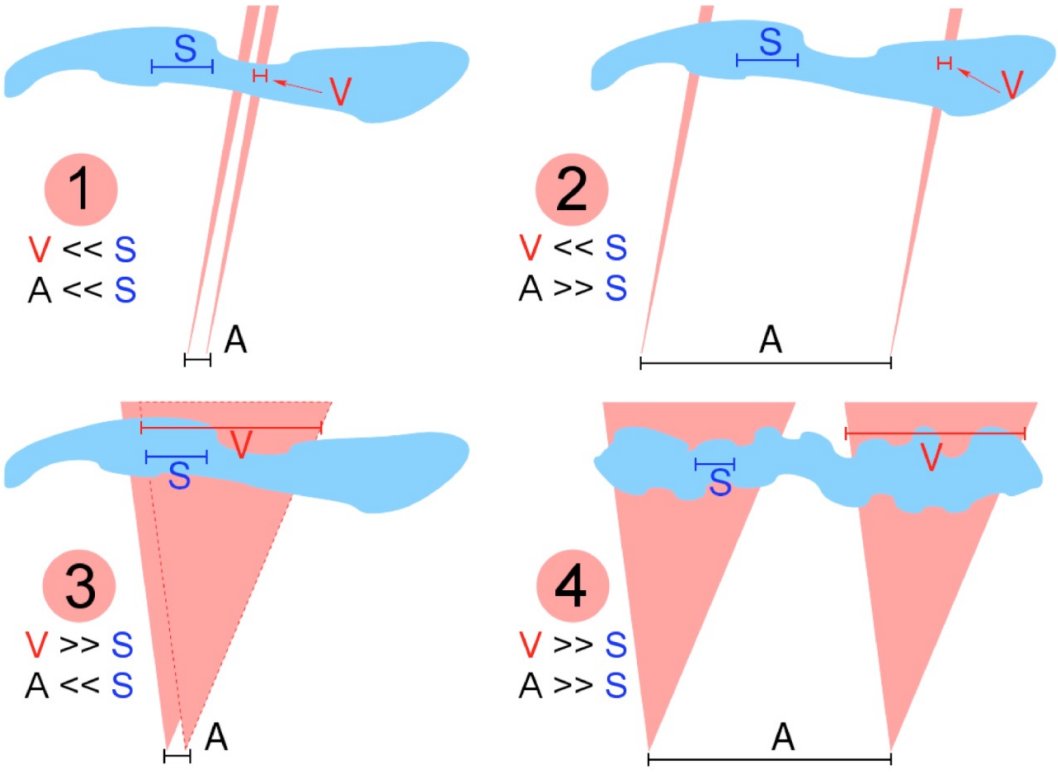

Figure 3.3: There are four regimes that result depending on the size of the array and the size of the field of view. A is the array size on the ground. V is the FOV at ionospheric heights. S is the scale size of the ionospheric irregularities which is in the range of 1 to 100 km. Source: (Lonsdale, 2005)

Regime 1 (top left) portrays compact arrays (small baselines) with a small FOV. Regime

two (top right) shows extended arrays (long baselines) with a small FOV. Regime 1 and 2 can be dealt with by using self-calibration. Regime 3 (bottom left) indicates compact arrays with large FOV. This regime can be dealt with by modeling distortions as position-dependent refractive shifts. Regime 4 (bottom right) indicates extended arrays with large FOV. In this regime, phase variation across the FOV is significant. Calibration in this regime is not so straightforward. Most radio astronomy interferometers and future telescopes have a regime 4 design. When the first data sets of low frequency (150 MHz) Giant Metrewave Radio Telescope (GMRT) were reduced it became clear that a new method of data calibration was needed (Intema, 2014).

The Source Peeling and Atmospheric Modeling (SPAM) software was developed to deal with ionospheric phase errors, directional dependent effects and to reduce the amount of time spent on tedious data reduction steps (Intema et al., 2009). SPAM is designed to deal with the most complex regime which is regime 4. Measurements of the ionospheric phase structure are extracted by phase calibration of the brightest sources in the FOV using an automated peeling routine. The directional dependent phase corrections in arbitrary viewing directions are predicted using optimized sets of base functions during imaging. When deconvolving the dirty beam the imager can correct for any direction dependent phase errors using a facet-based algorithm which divides the field of view into smaller polyhedral facets (Perley, 1989; Cornwell and Perley, 1992) method and the Cotton-Schwab CLEAN deconvolution. SPAM has the power to handle any other effects like asymmetric primary beams and pointing errors. This is achieved by the robust CLEAN scheme that the imager algorithm uses. The latest SPAM software package is fully automated and produces results that are comparable to the best, currently existing, self-calibration model and field-based calibration method.

CHAPTER 4

Diffuse Radio Emission in ACTPol Clusters

Over the few past decades, massive clusters that were predicted to host diffuse radio emission were selected using the X-ray luminosity. The X-ray luminosity of a cluster is related to the cluster mass. It has been used as a mass proxy for targeting massive clusters. Studies found that diffuse radio sources in the form of Giant Radio Halos (GRHs) in the X-ray selected clusters, satisfied scaling relations with the thermal properties of the cluster (Cassano et al., 2013). These statistically defined relations revealed the existence of a bimodal behaviour in the radio power and X-ray luminosity of galaxy clusters. The scaling relations can also be used to probe the evolution of diffuse radio sources. Recently, the SZ effect has been found as a more robust proxy for selecting massive clusters at higher redshifts (Hasselfield et al., 2013). The detection of SZ-selected clusters hosting diffuse radio emission has increased over the past years (Knowles et al., 2015; Botteon et al., 2016; Macario et al., 2010). Now the primary focus, similarly to x-ray selected clusters, is to investigate the scaling relations of the SZ-selected clusters. Millimeter surveys such as the Planck survey (Bonafede et al., 2015), the SPT survey (Schaffer et al., 2011), and the ACT survey, provide SZ-selected cluster samples that can be used to search for diffuse radio emission in galaxy clusters. The main aim of these surveys is to obtain statistically complete cluster samples from which scaling relations can be derived.

The ACT telescope is an off-axis Gregorian design telescope situated in the Atacama desert in Chile. It is a six-meter dish that observes the sky at millimeter wavelengths with

arcminute resolution (Swetz et al., 2011). This telescope has been operating since 2008. During the 2008 to 2011 season, the telescope observed two regions of the sky. The first region was at -55^o declination and 455 square degrees wide. The second region was 504 square degree wide and located at the celestial equator ($\delta = 0^o$). In both these regions, the survey was used to detect galaxy cluster via the SZ distortions that produce approximately arcminute scale temperature reductions along the line of sight (Marriage et al., 2011). The ACT regions overlapped with optical surveys such as the SDSS, which means that they could immediately obtain optical counterparts for the SZ detected galaxy clusters (Menanteau et al., 2013). In the 2008-2011 season, $\sim$91 clusters were detected and had optical counterparts, with 68 of these clusters being new detections (Menanteau et al., 2013; Hasselfield et al., 2013).

Recently, the ACT survey was upgraded to include polarization sensitive receivers (ACTPol) that operate at dual frequencies of 97 GHz and 148 GHz (Thornton et al., 2016). The ACTPol survey's first season observations used the deep survey strategy (Naess et al., 2014). The deep survey consists of four 120 square degree regions at different positions. In the second season the wide survey strategy was included (Louis et al., 2016). The wide survey is a concatenation and extension of the deep survey fields that is observed at shallower sensitivities compared to the deep survey. These fields overlap with other wavelength surveys, in particular, the SDSS BOSS N region (Louis et al., 2016). For our sample, we focused on the 900 square degree region which covers two deep fields, namely, the D5 and D6 regions. Figure 4.1 is an image of the D56 wide field region and the other wavelength surveys it overlaps with.

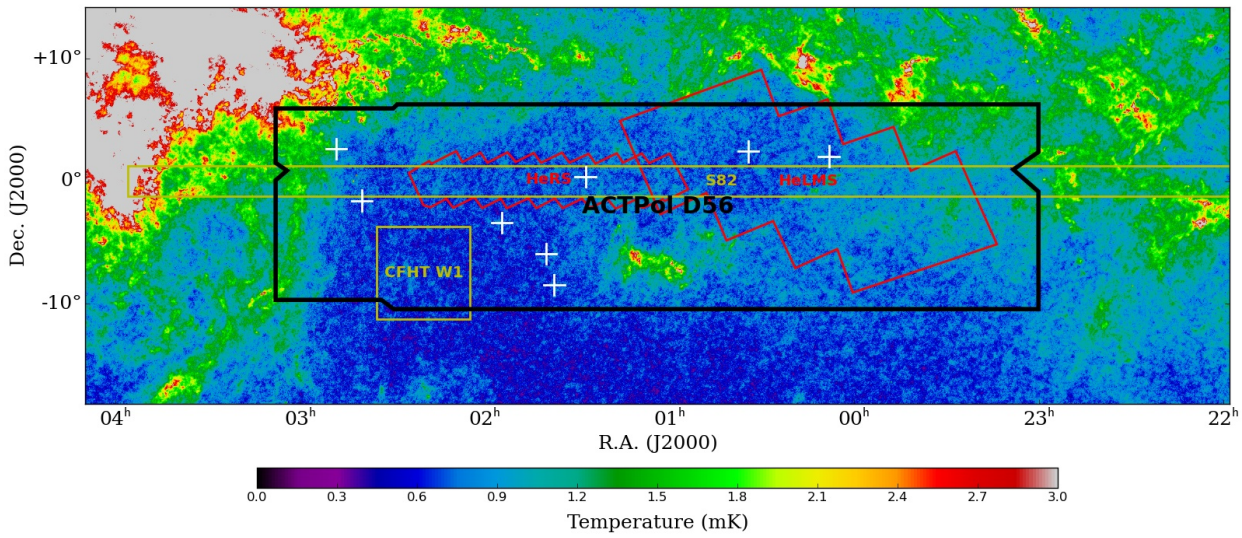

Figure 4.1: The location of the ≈ 900 deg^2 ACTPol D56 field overlaid on the Planck 353 GHz map. The locations of Herschel surveys (HeRS, HeLMS) and deep optical surveys (SDSS S82, CFHTLS W1) are also shown. The whole D56 field is covered by the SDSS legacy survey. Source: GMRT cycle 30 proposal (image by Dr. M. Hilton, PI: Dr. K. Knowles)

4.1 The Giant Metrewave Radio Telescope

The Giant Metrewave Radio Telescope (GMRT) (Swarup, 1990) is situated in Pune, India. It came into full operation in 1996. The full GMRT array is made up of 30 antennas that are 45 m in diameter. The array operates at a frequency range of 50 MHz to 1450 MHz. The antenna configuration does not fall into any categorized configuration, it is a hybrid of the Y-shaped configuration 4.2. It consists of 14 antennas that are randomly distributed in the central region within a radius of one kilometer. The random distribution of the antennas in the central region was made to strategically avoid the grating lobes. The remaining antennas are distributed in a Y-shaped configuration, the length of each arm is approximately 14 km, with the maximum baseline being 26 km. The dense central antennas provide a large number of relatively short baselines. This is very useful for imaging large extended sources since their visibilities are concentrated near the center of the uv-plane. This makes GMRT ideal for giant radio halo observations.

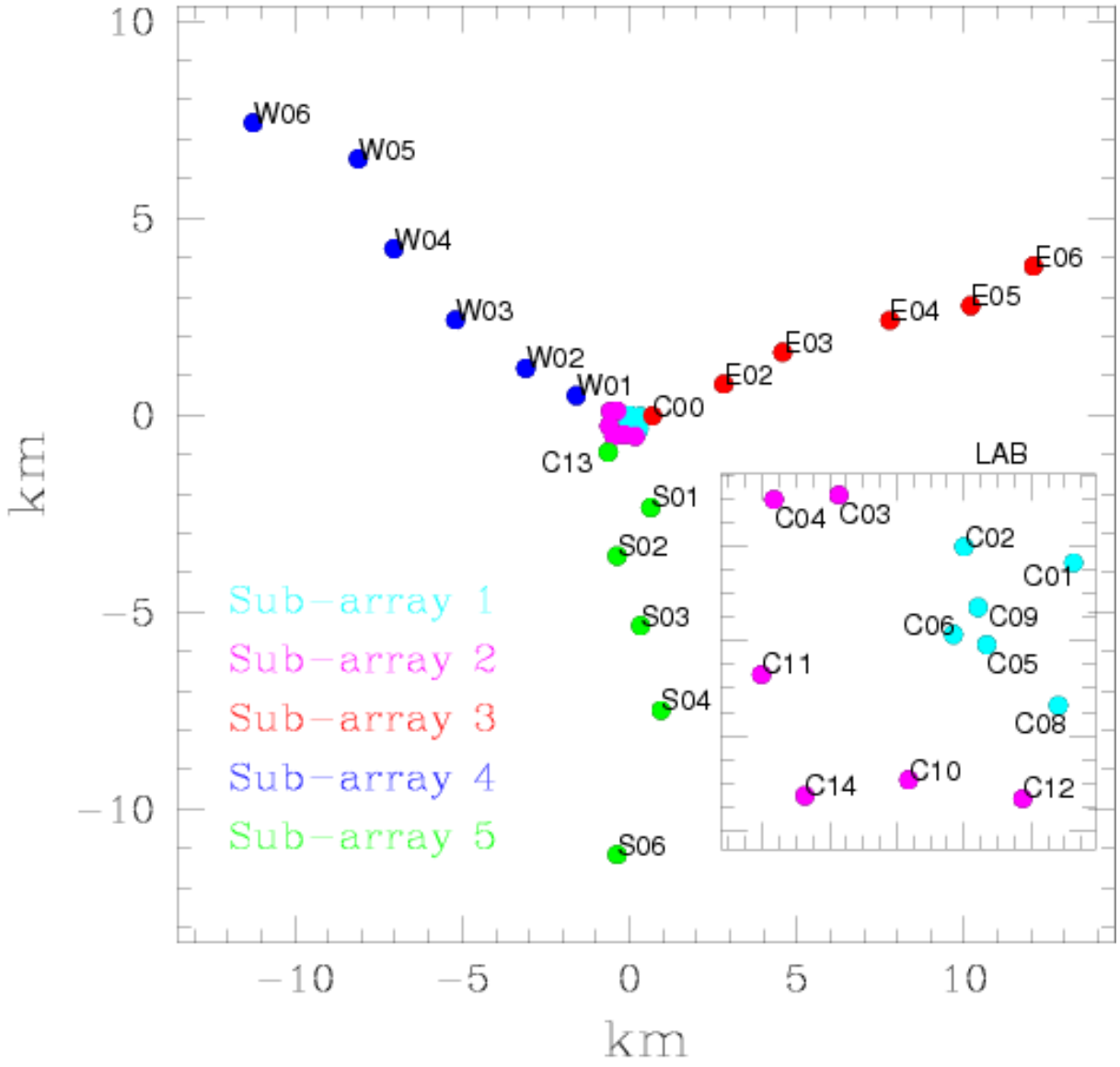

Figure 4.2: The GMRT antenna lay out. Source: (Bhat et al., 2013)

The antennas are parabolic reflectors and have a Gregorian design. The 610 MHz and 233 MHz feeds are of a dual frequency and have coaxial feeds, which meanins that observations of both frequencies can be simultaneously done. The principal back-end used for interferometric observations is a 32 MHz wide FX correlator. The correlator produces a maximum of 256 spectral channels for each of two polarizations (RR, LL) for each baseline.

Table 4.1: These are the measured system parameters of the GMRT taken from the July 2015 manual. This table gives the telescope specifications at different observing frequencies.

Frequency (MHz) :	151	235	325	610	1420
Primary Beam (HPBW, arcmin)	186 ± 6	114 ± 5	81 ± 4	43 ± 3	$(24 \pm 2) \times (1400/f)$
Receiver Temperature (K)	295	106	53	60	45
Sky Temperature (off galactic plane, K)	308	99	40	10	4
Ground Temperature (K)	12	32	13	32	24
Total System Temperature ($T_r + T_{sky} + T_{ground}$, K)	615	237	106	102	73
Antenna Gain ($KJy^{-1}Antenna^{-1}$)	0.33	0.33	0.32	0.32	0.22
Synthesized Beam (FEM, arcsec)	20	13	9	5	2
Largest detectable structure (arcmin)	68	44	32	17	7
Usable frequency range (MHz)	150-156	236-244	305-345	580-640	1000-1450
Fudge Factor (for long observations)	5	2	2	1	1
Best RMS Sensitivities (mJy)	0.7	0.25	0.04	0.02	0.03
Typical dynamic range achieved	> 1500	> 1500	> 1500	> 2000	> 2000

For our observations, we use the 610 MHz continuum bandwidth which is 32 MHz wide, antenna specifications for this observing bandwidth are stated in table 4.1. From simulations done for the proposal, we estimated that in our observations we required the sensitivity to be at least 40 μJy beam^{-1} in order to detect diffuse radio emission if it is present. We only used the RR and LL polarization channels.

4.2 The ACTPol Cluster Sample

We used the methods described in (Hasselfield et al., 2013) to construct the galaxy cluster list in the $\approx$ 900 deg^2 D56 field. This region currently consists of 75 optically confirmed clusters consisting of redshift measurements detected with SZ signal-to-noise-ratio (SNR) > 5. The clusters that have a SNR > 5 also corresponds to the massive clusters, as there is a positive correlation between mass and SNR. Preliminary M_{500} mass estimates, based on the SZ signal strength, were also obtained for the current ACTPol cluster sample using the method that is described in Hasselfield et al. (2013).

We proposed a radio wavelength follow-up for some of the observed ACTPol clusters, to search for diffuse radio emission, using the Giant Metrewave Telescope continuum mode at 610 MHz, which has a bandwidth of 32 MHz. For our proposal we implemented the following mass and redshift cuts on the ACTPol sample: $z < 0.6$, and $M_{500} > 4 \times 10^{14} M_{\odot}$.

This selection function left us with a sample of 16 uniformly selected clusters, eight of which have been previously observed with the GMRT.

4.2.1 Clusters with Archival Data

In this section, we give a summary of the eight clusters that have been observed with the GMRT telescope. We will briefly discuss the published results if they are available. In the case that the cluster is observed but there are no publications, we will give details of the GMRT observations.

ACT-CL J0152.7+0100

ACT-CL J0152.7+0100, well known as Abell 0267, was observed in GMRT's cycle 16 in 2009, the PI of the observations was R. Cassano. This cluster was observed at 610 MHz for 9.5 hours. The analysis of the dynamics of this cluster were published in Cassano et al. (2013), Cuciti et al. (2015) and Kale et al. (2015). Cassano et al. (2013) found that ACT-CL J0152.7+0100 did not host any diffuse emission. Cuciti et al. (2015) calculated the radio halo upper limit to be $P_{1.4} < 23.55$ W Hz^{-1}.

ACT-CL J2337.6+0016

ACT-CL J2337.6+0016, also known as Abell 2631, was observed in GMRT's cycle 18 in 2010, the PI of the observations was G. Brunetti. This cluster was observed at 610 MHz for 35.3 hours. The analysis of the dynamics of this cluster were published in Venturi et al. (2007), Cassano et al. (2013), Wen and Han (2013), Cuciti et al. (2015) and Kale et al. (2015). Venturi et al. (2007) discovered that this cluster did not host any diffuse emission and then calculated the upper limits. The radio halo upper limit to be $P_{1.4} < 24.13$ W Hz^{-1}. Cuciti et al. (2015) calculated tighter upper limits, these were calculated to be $P_{1.4} < 23.74$ W Hz^{-1}.

ACT-CL J0014.9−0057

ACT-CL J0014.9−0057 was observed in GMRT's cycle 22 in 2012, the PI of the observations was K. Knowles. This cluster was observed at 610 MHz for 6.4 hours. Currently, there are no publications of this cluster's dynamical state. However, it forms part of a sample observed in K. Knowles's Ph.D thesis (Knowles, 2016). In this thesis, it was found that ACT-CL

J0014.9−0057 does not host any diffuse emission. The radio halo power upper limit was calculated to be $P_{1.4} < 24.13$ W Hz^{-1}.

ACT-CL J0045.2−0152

ACT-CL J0014.9−0057 was observed in GMRT's cycle 26 in 2014 at 610 MHz. This cluster had two proposals, the PI for the first proposal was K. Knowles and the PI for the second proposal was A. Tej. K. Knowles observed the cluster for 10.0 hours and A. Tej observed it for 6 hours. Currently, there are no publications of this cluster's dynamical state. However, it forms part of a sample observed in K. Knowles's Ph.D thesis (Knowles, 2016). In this thesis, it was found that ACT-CL J0045.2−0152 does not host any diffuse emission. The radio halo power upper limit was calculated to be $P_{1.4} < 24.27$ W Hz^{-1}. This cluster also has spectroscopic data from Kirk et al. (2015). Hence, a multiwavelength analysis of this cluster could be done.

ACT-CL J0248.2−0216

ACT-CL J0248.2−0216, well known as Abell 0384, was observed in GMRT's cycle 26 in 2014, the PI of the observations was R. Cassano. This cluster was observed at 610 MHz for 3.7 hours. Currently, there are no published results for ACT-CL J0248.2−0216. This cluster will form part of the papers that will be published upon the completion of the observation of the full sample. The reduction of this data will form part of the future work.

ACT-CL J0019.6+0336

ACT-CL J0019.6+0336 was observed in GMRT's cycle 25 in 2013, the PI of the observations was A. Bonafede. This cluster was observed at 325 MHz for 6.5 hours. Currently, there are no published results for ACT-CL J0019.6+0336. This cluster will form part of the papers that will be published upon the completion of the observation of the full sample. The reduction of this data will form part of the future work.

ACT-CL J0003.2−0605

ACT-CL J0003.2−0605, also known as Abell 2631, was observed using the GMRT in 2005, the PI of the observations was R. Cassano. This cluster was observed at 610 MHz for 2 hours. The analysis of the dynamics of this cluster were published in Cassano et al. (2013)

and Kale et al. (2015). Cassano et al. (2013) discovered that this cluster did not host any diffuse emission. Kale et al. (2015) calculated the radio halo upper limit to be $P_{1.4} < 23.56$ W Hz^{-1}.

ACT-CL J0159.8−0859

ACT-CL J0019.6+0336 was observed in GMRT's cycle 21 in 2011, cycle 27 in 2014 and cycle 28 in 2015. The PI of the observations of cycle 21 was G. Macario, for cycle 27 it was G. Simona and for cycle 28 it was L. George. In cycle 21 it was observed at 325 MHz for 12.2 hours. In cycle 27 it was observed at 610 MHz for 3.8 hours. In cycle 28 it was observed at 1.4 GHz for 6.7 hours. The analysis of the cluster dynamics have been published in Wen and Han (2013). Wen found that the cluster is relaxed. Since it is relaxed, this cluster does not host any diffuse radio emission.

4.2.2 New Cluster Observations

We proposed to observe the remaining eight clusters to complete the sample of the ACTPol pilot project (PI: Dr. K. Knowles). To determine integration times for each of the clusters in our sample, we estimated the restframe 1.4 GHz radio power, $P_{1.4}$, for each cluster, assuming that it hosts a radio halo, by using the $P_{1.4}$–M500 scaling relation presented in Cassano et al. (2013). We were granted observation time sufficient for four clusters, hence, we applied a further mass cut of $M_{500} > 6 \times 10^{14} M_{\odot}$ and we ended up with the clusters listed in table 4.2. We will propose to observe the remaining clusters in the upcoming GMRT cycle 32 call. One of these clusters is a new SZ detection that is not detected in the Planck PSZ2 catalog (Planck Collaboration et al., 2016a). Three of the four clusters have existing archival X-ray data from either *Chandra* or *XMM*, and adding the optical data from SDSS means that we immediately have a multiwavelength view of these systems.

Table 4.2: The four clusters extracted from the list of our sample of 16 ACTPol clusters. This table gives details of the position, mass, redshift, and cluster size. The last column is the total *on-source* time.

Cluster Name	RA [h:m:s]	DEC [d:m:s]	M_{500} [$10^{14} M_{\odot}$]	z	θ_{500} [arcmin]	T_{source} [hrs]
ACT-CL J0034.4+0225	00:34:25:99	02:25:02.64	8.3	0.37	4.1	7
ACT-CL J0239.9-0135	02:39:59.22	-01:35:00.60	7.2	0.37	4.0	6
ACT-CL J0140.0-0555	01:40:00.01	-05:55:08.04	6.3	0.45	3.3	14
ACT-CL J0137.4-0827	01:37:23.99	-08:27:50.76	7.3	0.57	2.9	8

We used GMRT to observe our clusters at a radio wavelength of 610 MHz. The GMRT is most efficient when searching for diffuse radio emission because its antenna array layout has a dense core and extended antennas 4.2. This means that there are numerous short baselines which can be used to search for extended radio emission and long baselines can be used to subtract the bright point sources. During our observations, there were technical glitches that resulted in some clusters acquiring more observation time.

4.3 Data Reduction Pipeline

The GMRT array has baselines that are up to 26 km long, due to the length of these baselines the GMRT in a non-coplanar interferometer. This means, when analyzing the visibilities, one has to take into consideration the w-term which adds a third dimension to the uv-plane. As a result, observational data from this telescope is corrupted by the directional dependent effects such as the ionospheric phase errors (discussed in section 3.7). The Source Peeling and Atmospheric Modeling (SPAM) software package (Intema et al., 2009) was designed to deal with such effects. SPAM's reduction process tasks are based on the Astronomical Image Processing System (AIPS) (van Moorsel et al., 1996) and it uses Obit tools for tables and imaging (Cotton, 2008). The interactive interface SPAM uses is Parseltongue (Kettenis et al., 2006).

The latest SPAM package consists of a fully automated, python scripted, pipeline. The pipeline consist of two stages: pre-calibration and the processing of the target field. The pre-calibration process obtains the calibration and the flagging information from the flux and phase calibrators and the flagging file provided by the telescope operators. It then picks

the best calibrator (flux or phase) and transfers the flagging and calibration information, from this calibrator to all the other source visibilities present in the observations. The pre-calibrated visibility data from each observed field is exported in the form of UVFITS files. At the end of the pre-calibration process, three UVFITS files are produced: the main target source field, the flux calibrator, and the phase calibrator, this separation of fields method is adopted from (Cotton et al., 2004). The target source field UVFITS FILE is then used, in combination with a source list, in the second stage, which is processing the target. The source list is obtained from existing radio surveys such as the NRAO VLA Sky Survey (NVSS) (Condon et al., 1998) or the Very Large Array (VLA) Faint Images of the Radio Sky at Twenty-cm survey (FIRST) (Becker et al., 1994) and the catalog is created using PyBDSM (Mohan and Rafferty, 2015). The processing of the target field is done in three main steps: Main Calibration, Self-Calibration, and solving for Directional Dependent Effects. Below, we discuss these steps in detail using the reduction results of the ACT-CL J0140.0-0555 cluster as an example.

4.3.1 Main Calibration

The pipeline begins by applying the main calibration on the target field. The main calibration corrects for the antenna systematics and creates a sky model. The relevant steps for the main calibration stage are:

1. The pipeline automatically chooses a reference antenna. This reference antenna is required for calibration. This antenna needs to be stable for most of the observation, hence, GMRT reductions use the central antennas such as C09 or C02.

2. Cover the primary beam with a number of facets and also including facets at places of interfering outlier sources. The outlier sources are included because their sidelobes could be corrupting the data. Hence, the outlier sources also need to be modeled

3. Check the field for bright sources and make a primary beam sky model based on the existing radio survey catalogs. We obtain the source positions catalogs from surveys such as the NVSS.

4. Clip the visibility amplitudes based on the flagging information provided by the GMRT observers. Visibility amplitudes that have spikes and discontinuous phases are considered as corrupted data and are flagged.

5. Make an alternative sky model using the provided source list catalog that can be obtained from the online catalogs and create an image of the primary beam sky model (PBM). This source list catalog is created using a software package called the Python Blob Detection and Source Measurement software (PyBDSM) (Mohan and Rafferty, 2015).

6. Do a full primary beam calibration using the flux calibrator and flag bad antenna or periods. A flux calibrator is a primary bright source which is well studied that can provide the flux scale for the observation and initial phase solutions. Bad antennas are antennas that contain data that has visibility amplitude spikes and discontinuous phases.

7. Measure the initial noise, producing a calibrated primary beam image (CPB) of the sky model. The CPB image is obtained by calibrating the sky model using the flux calibrator. This image is placed at the center of the field of view.

8. Image the primary beam applying facets in outlier sources, producing the main calibration image MC1. The MC1 image is obtained from calibrating the data using the flux calibrator.

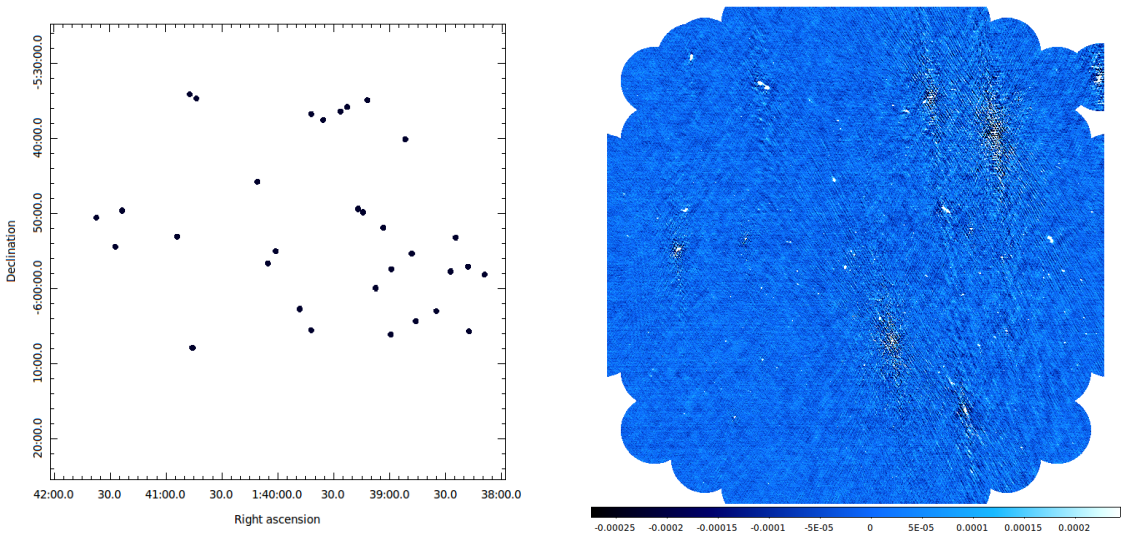

Figure 4.3: *left*: An image of the primary beam sky model, each dot represents a source it the field of view. *right*: The J0140.0-0555 full field of view image produced after the main calibration step, has a noise level of 73.89 μJy beam^{-1}. The colour units for this image are in Jy beam^{-1}.

4.3.2 Self-Calibration

The image produced after the main calibration still has a lot of residuals, phase errors, and high noise levels. To get rid of these artifacts and reduce noise levels, the pipeline does a self-calibration loop over three cycles. The relevant steps for the self-calibration stage are:

1. Correct for ionospheric delays (see section 3.5) per 5-minute observation and then calibrate against the true sky model, which is defaulted to the NVSS catalog.
2. Remove the instrumental phase errors through automated flagging.
3. Remove the primary beam source model from the data.
4. Apply automated baseline-by-baseline flagging of the model subtracted data.
5. Image the CLEAN primary beam facets producing the first self-calibration image SC1. These facets are imaged using a Cotton-Schwab CLEAN deconvolution using an iterative, automatic clean-boxing algorithm (see section 3.4.2.1).
6. Determine the amplitude self-calibration solutions and apply them to uv-data.
7. Calibrate the data against the sky model and re-image to produce the second self-calibration image SC2.
8. Repeat steps 3 and 4.
9. Use Obit tasks to subtract lower level RFI. RFI is radio frequency interference, which is also considered as a source of corrupt data.
10. Apply bandpass calibration on the target field.
11. Make global astrometric corrections by correcting for source positions using the NVSS catalog. The positions of sources can appear to have shifted if the time-average of the residual phase errors in the direction of the sources has a non-zero spatial gradient (Intema et al., 2009). This effect can be introduced during any of the calibration processes, but particularly if during peeling, a source is centered on the incorrect catalog position.
12. Calibrate against the true sky model and re-image creating the final self-calibration image SC3.

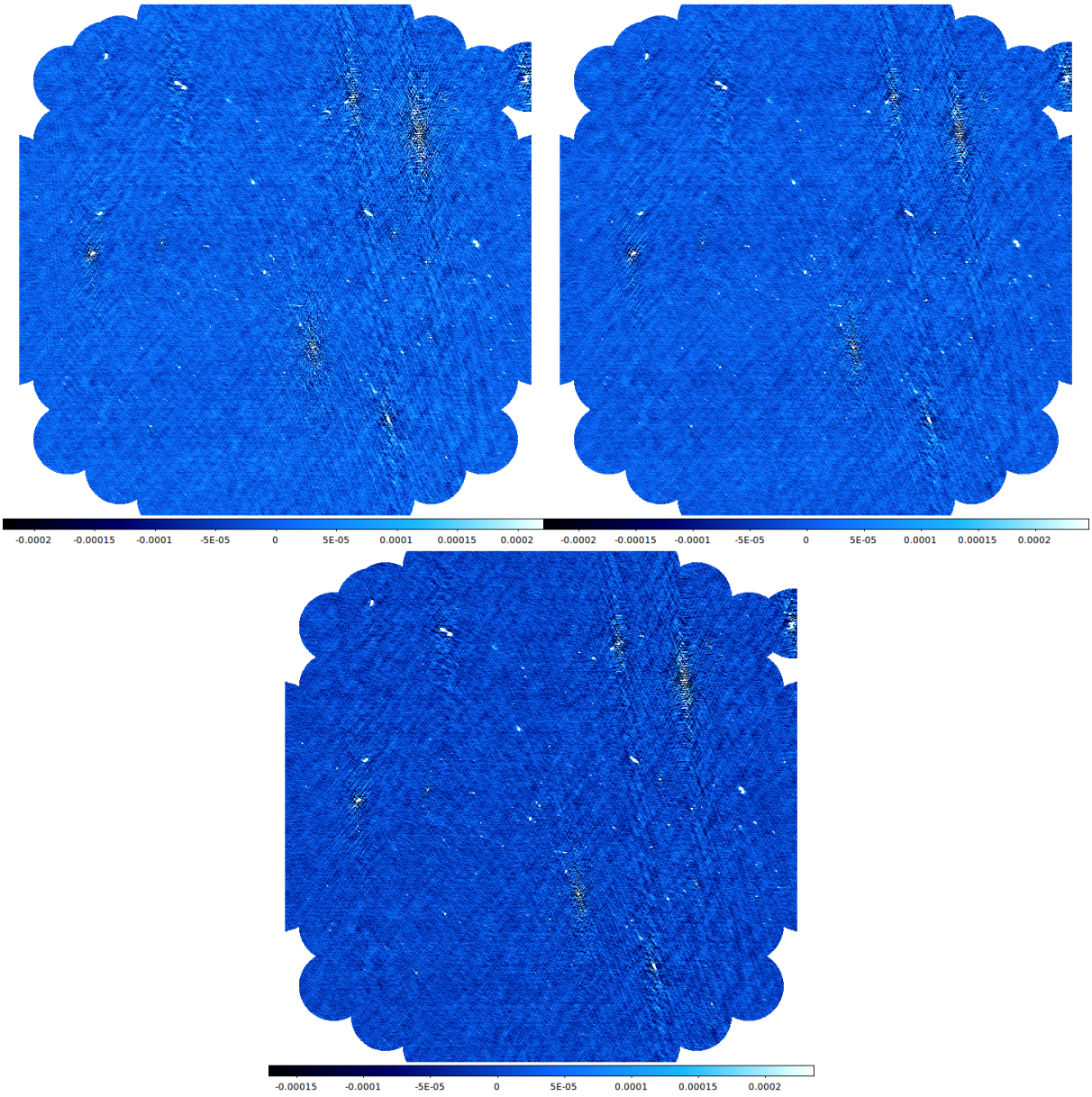

Figure 4.4: The self-calibration images of J0140.0-0555. The colour units for the images are in Jy beam^{-1}. *left*: The first self-calibration image with noise levels 65.01 μJy beam^{-1}, there is a significant improvement in both noise and residuals compared to the main calibration image. *right*: The second self-calibration image with noise levels 53.48 μJy beam^{-1}. *bottom*: The final self-calibration image with noise levels 50.54 μJy beam^{-1}. Although there is a significant improvement compared to the main calibration image there are still north-south residuals around bright point sources.

4.3.3 Directional Dependent Effects

The north-south residuals around the bright point sources are due to directional dependent effects such as ionospheric phase errors. The SPAM pipeline deals with these by applying peeling over the brightest sources in the field. In short, peeling is when the bright sources in the field of view are identified and a measurement for the atmospheric phase structure

is made by phase calibrating on these sources over short time intervals. From these bright sources, an ionospheric model is derived and fitted to the rest of the image. This process is repeated until all bright sources have been individually calibrated. The peeling process is discussed in detail in Noordam (2004). SPAM builds the ionospheric model through peeling and fits this model to the data to correct for directional dependent effects. To remove the north-south residuals, the pipeline applies the peeling method to the self-calibrated images. The relevant steps for the peeling stage are:

1. Update calibration, reference antenna, and global astrometric corrections before applying peeling.

2. Identify the bright sources in the self-calibrated data, using the primary beam facets and peel the bright sources.

3. Fit the ionospheric model to the selected sources. Approximately twelve sources are found in the first peeling attempt. The ionospheric model is obtained from the peeling process explained above.

4. Filter out systematic phase effects by smoothing the solutions in time and re-sampling the solutions.

5. Re-fit the ionospheric model and automatically flag the bad solutions.

6. Combine the model phase solutions, peeling amplitude solutions and delays to replace the model solutions.

7. Re-image producing the first source peeling image SP1.

8. Calibrate the bandpass phases on the target field and determine the amplitude calibration.

9. Filter the amplitude solutions and the outliers.

10. Calibrate and re-image producing SP1A.

11. Flag the image undulations, subtract the primary beam sources and flag again.

12. Flag based on the residual amplitudes, calibrate and re-image producing SP1B.

13. Repeat steps 2 to 12 producing images: SP2, SP2A, and SP2B. SP2B is the final image produced from the peeling process. The second round of peeling picks up more sources (∼20), hence, it produces a better ionospheric model fit.

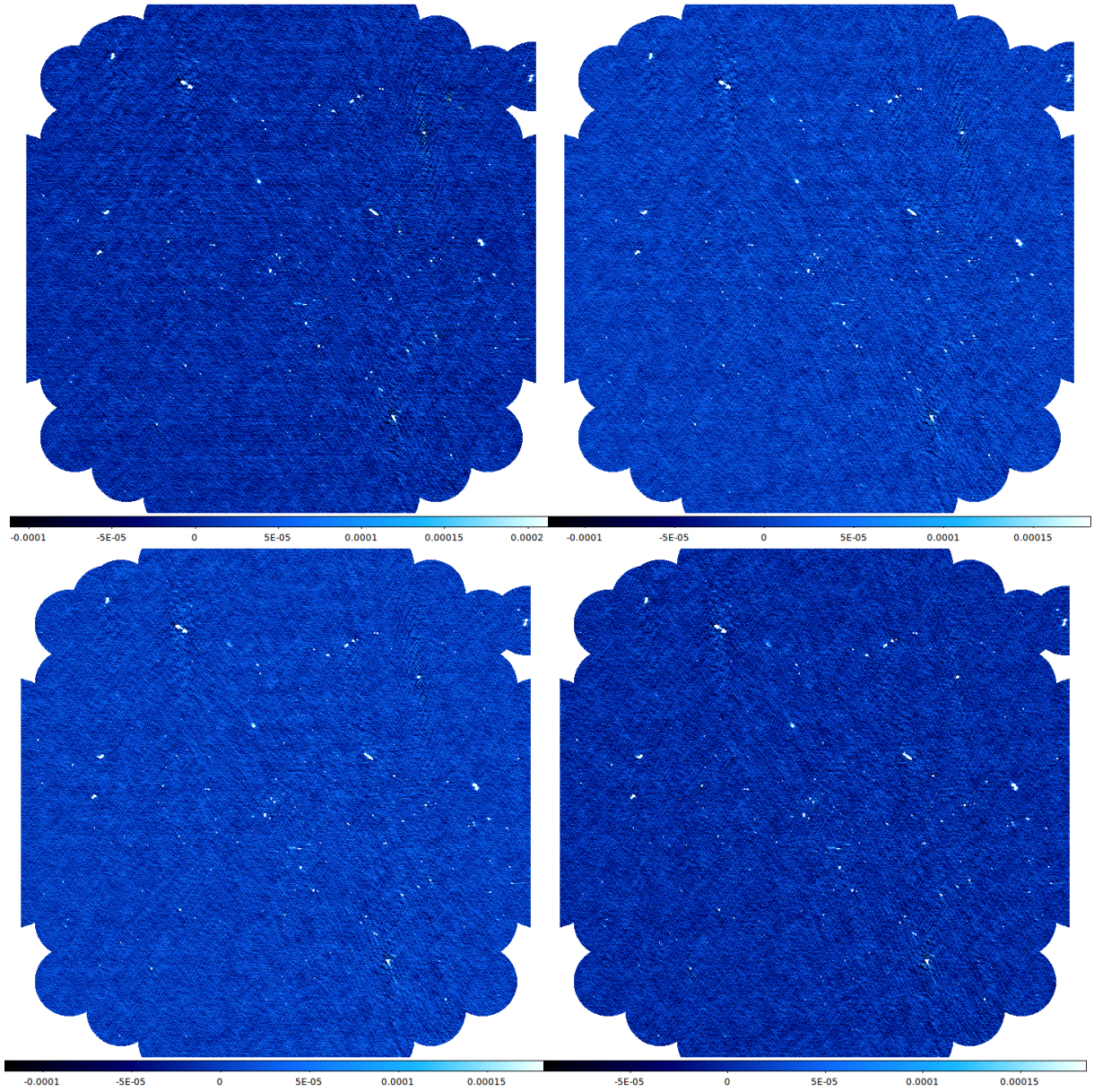

Figure 4.5: Removing the directional dependent effect in the J0140.0-0555 clusters field of view. The colour units for the images are in Jy beam^{-1}. *top left*: The first image produced after the first round of source peeling has noise levels of 44.82 μJy beam^{-1}. There is a significant improvement in both noise and residuals compared to the final self-calibration image. *top right*: The final image of the first round of source peeling produces an image with noise levels 39.65 μJy beam^{-1}. *bottom left*: The first image produced after the second round of source peeling has noise levels of 36.98 μJy beam^{-1}. *bottom right*: The final image produced after the second round of source peeling has noise levels of 34.45 μJy beam^{-1}. In this image the north-south residuals are barely visible, hence, we have achieved the best ionospheric model for the data.

4.3.4 Primary Beam Correction and Residuals

After obtaining the best fit ionospheric model for the target field, the pipeline then applies a primary beam and a flux scale correction to the targeted field. The primary beam corrected image is circular corresponding to the actual primary beam scale. The flux scale of the final image is corrected for by using the system temperature measurements from the Haslam sky survey (Haslam et al., 1981). The image produced is appropriate for scientific analysis such as computation of the fluxes of the radio sources in the target field. Finally, the pipeline creates a flagged and calibrated residual uv-data file with outliers removed. This uv-data file is used to create the residual image. The residual image is most useful for checking how well the model fits the data.

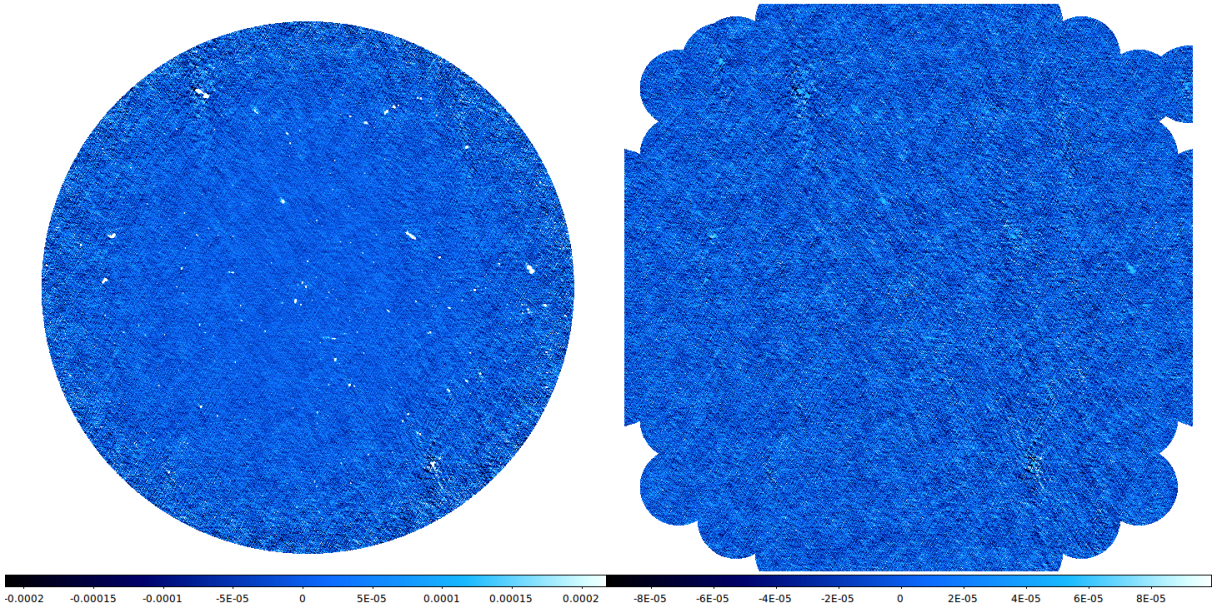

Figure 4.6: The final pipeline steps in reducing J0140.0-0555. The colour units for the images are in Jy beam^{-1}. *left*: The first primary beam corrected image with noise levels of 35.48 μJy beam^{-1}. *right*: The produced residual image. From the image, we gather that the model fits the data very well as the residuals are mainly noise structure.

For three of the four clusters the pipeline produced the best image, in terms of noise level and residuals, however, for one cluster, ACT-CL J0034.4+0225, the north-south residuals were still visible and the noise levels were high. For the ACT-CL J0034.4+0225 cluster, we had to modify the pipeline. To remove the radio-frequency interference (RFI), we applied more flagging using specific code from the pipeline. To obtain the best fit ionospheric models we added extra iterations of the peeling step. After adding these extra steps we obtained the best image. Table 4.3 summarizes the noise levels for the best case, full-resolution primary beam corrected, images. These images can be found in the appendix.

Table 4.3: A summary of the image properties obtained for the full-resolution images of the clusters and an indication of whether the cluster hosts diffuse radio emission or not.

Clusters	FR		Diffuse Radio Emission
	beam ($''$ × $''$, p.a^o)	RMS Noise (μJy beam^{-1})	Yes or No
ACT-CL J0034.4+0225	5.90 × 4.99, 22.20	34.60	Yes
ACT-CL J0239.9-0135	6.62 × 3.79, 42.20	37.89	No
ACT-CL J0140.0-0555	5.32 × 4.44, 12.52	34.00	No
ACT-CL J0137.4-0827	6.19 × 4.17, 23.04	21.83	Yes

Once we obtained the best image for all the galaxy clusters we then proceeded to search for faint diffuse radio emission in short baselines.

4.4 Searching for Diffuse Radio Emission

Diffuse radio sources in the form of giant radio halos (GRHs) and radio relics (RRs) often have faint flux, on the order of mJy, which is not immediately visible from the full-resolution reduced image. The field of view of the target source is usually filled with bright point sources that can overpower the low-lying emission. This point source emission can be modeled using the long baseline information, while the short baselines have the greatest sensitivity to extended emission.

To search for diffuse radio emission in the target fields cluster region we take advantage of the GMRT's antenna layout (Swarup, 1990). The GMRT has a dense core and extended arms of antennas (Y-shaped). This means that we can use the short baselines in the dense core for imaging the extended sources and the extended arms for subtracting bright point sources. For all the target fields, we obtained a high-resolution image by applying a visibility constraint of uv-range > 4 kλ. We used this image to subtract the point sources from the full-resolution image, creating the point source subtracted image. We checked the point source subtracted full-resolution image for point source residuals. Once happy with the image we proceeded to make low-resolution images.

We used the short baseline's visibility data to construct the low-resolution images from the point source subtracted full-resolution image. We applied uniform uv-range cuts and tapers to all the four target fields. The uv-taper controls the radial weighting of visibilities in the uv-plane. The visibilities are "tapered" with weights decreasing as a function of uv-radius. While the uv-range cuts get rid of all the information beyond the specified uv-distance, this sharp cut creates ringing in the image plane and this results in bad images.

A combination of the uv-tapering and cuts is advantageous for ensuring that we minimize the amount of data discarded. For the first low-resolution image, we applied a Gaussian uv-taper at 10 kλ and did not use a uv-range cut. For the second low-resolution image, we applied a uv-range cut of < 5 kλ and uv-taper at 4 kλ. The results obtained in each target field are discussed in depth in the following sections.

4.4.1 ACT-CL J0034.4+0225

ACT-CL J0034.4+0225 is not a new ACTPol survey detection as it is also detected in the Planck SZ source catalog (Planck Collaboration et al., 2016a). The archival XMM-Chandra data revealed that it is a dynamically disturbed system. In searching for diffuse radio emission the uv-tapers and range restrictions were applied as explained in the text above. The image gallery in figure 4.7 reveals that there was a detection in the first low-resolution image. Table 4.4 provides a summary of the noise and beam properties of these images.

We could not categorize the detected diffuse radio emission due to its morphology and position not directly falling under GRH or RR category. This emission is not symmetrical and it is not centered on the cluster's SZ peak, with the peak of the extended emission offset from the SZ peak by 33.07 arcseconds. This morphology does not fit that of a typical GRH, however, it could be a low signal-to-noise detection. Although radio relics come in different sizes, morphologies, and locations, this emission is quite close to the cluster's SZ peak and is thus unlikely to be a radio relic. Another possibility is that this extended radio emission is a radio phoenix. Radio phoenix sources are also a group of diffuse radio sources. These objects have been rarely studied and do not have a well-defined model that describes their formation and morphology. They are believed to be old radio galaxy lobes that are energetically revived by adiabatic compression during cluster mergers (de Gasperin et al., 2015). A multiwavelength analysis and a radio wavelength follow up using an interferometer with higher sensitivity will help us with the classification of this tentatively detected extended radio emission.

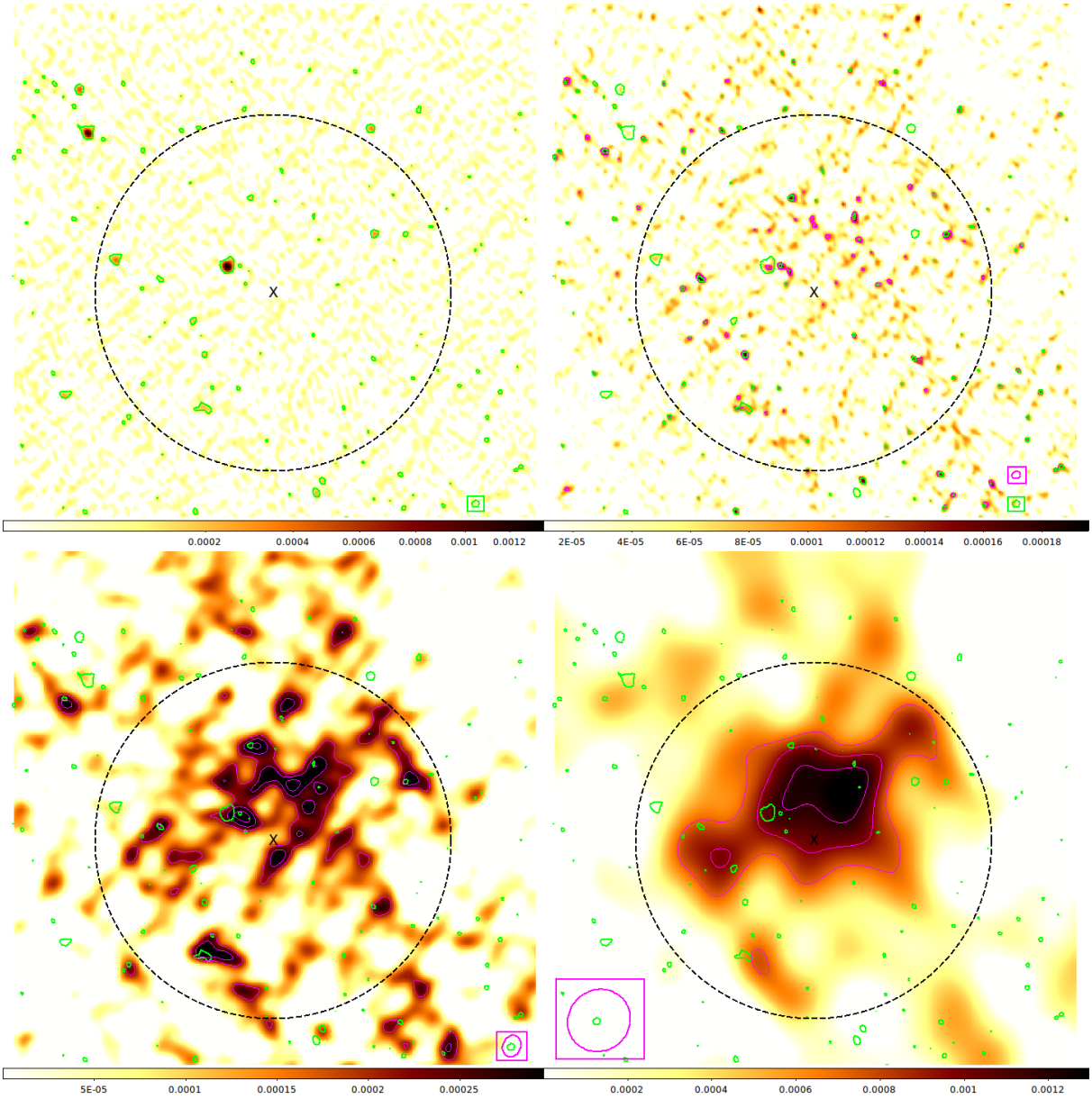

Figure 4.7: A gallery of the images of J0034.4+0225 produced during the search for diffuse radio emission. The colour units for the images are in Jy beam^{-1}. The black dashed indicates the θ_{500} cluster region with a diameter of 4.1′. The 'x' indicates the cluster center. The green contours indicate the point source emission and are at 3σ level, The 1σ level in this image corresponds to 42 μJy beam^{-1}. For all the images the magenta contours indicate diffuse radio emission detected above the noise level of the image. The ellipses enclosed by a box represent the beam size of the contours with the corresponding colour. *top left*: The high-resolution image with the point source contours. *top right*: Point source subtracted image. The image has a 1σ level of 35 μJy beam^{-1}, the contours show a 2σ and 6 σ detection increasing inwards. *bottom left*: Point source subtracted low-resolution image (uv-taper 10 kλ). The diffuse radio emission is outlined with contour levels as follows: (3σ,4σ,5σ) increasing inwards. The 1σ level in this image corresponds to 70 μJy beam^{-1}. *bottom right*: Point source subtracted low-resolution image (uv-range cut $<$ 5 kλ, uv-taper 4 kλ). The diffuse radio emission is outlined with contour levels as follows: (3σ,4σ,5σ) increasing inwards. The 1σ level in this image corresponds to 240 μJy beam^{-1}.

Table 4.4: A summary of the image properties obtained in the diffuse radio emission search in the ACT-CL J0034.4+0225 cluster. This table contains image properties for the high-resolution, point source subtracted and low-resolution images.

Image Name	Beam Size ($'' \times ''$, p.a ^{o})	RMS Noise μJy beam^{-1}
HR	5.42 × 4.47, 26.40	42.0
PSSUBFR	5.90 × 4.99, 22.16	35.0
PSSUBLR1	15.23 × 12.23, -68.10	70.4
PSSUBLR2	44.37 × 41.72, -38.75	240.0

Our observing fields had several point sources and the full-resolution images had a very low noise level, hence, we used this to our advantage and searched for point sources in the cluster region. When searching for the compact sources in the cluster region we used the primary beam corrected image because it is corrected for the fluxes of the radio sources, hence, it yields the appropriate source flux measurement. We calculated the radio fluxes using the ds9 (Buzzi et al., 2013) add-on function called 'radio flux'.

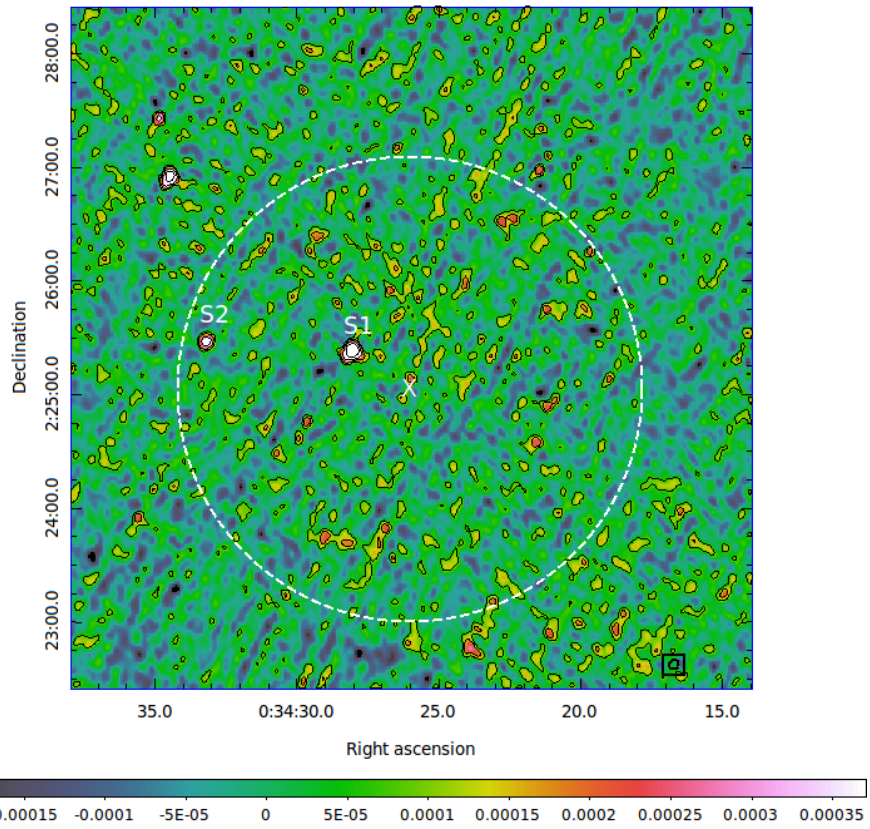

Figure 4.8: The J0034.4+0225 θ_{500} cluster region is indicated by the dashed circle. The projected size of this region is 1.3 Mpc. The 'x' is positioned at the cluster center. The colour units for this image are in Jy beam^{-1}. The 1σ noise level in the cluster region corresponds to 37 μJy beam $^{-1}$ and the contour levels indicate (3σ,6σ,12σ,24σ), increasing inwards. The beam size is ($5.90'' \times 4.99''$) and the beam orientation angle is 22.20° indicated by the ellipse enclosed by a box. The source fluxes for S1 and S2 can be found in table 4.5.

Table 4.5: The radio fluxes of the compact sources within the θ_{500} cluster region of J0034+0025, cross-matched with FIRST and NVSS.

Sources	RA [h:m:s]	DEC [d:m:s]	S_{610MHz} mJy
S1	00:34:33.19	02:25:27.05	0.59 ± 0.16
S2	00:34:28.02	02:25:25.83	2.06 ± 0.20

Two sources were detected in the cluster region, as shown in figure 4.8. We cross-matched the sources in both the FIRST and the NVSS surveys and none of them have been detected in these surveys. The positions and flux measurements of these sources are summarized in table 4.5. We searched for optical counterparts using the Sloan Digital Sky Survey DR10

archival data (Ahn et al., 2014). We used a combination of the *rgi* images to create the optical image. Although we do not have spectroscopy to determine galaxy members for this cluster, the cluster is clearly visible and consists of mainly red galaxies owing to the cluster redshift of 0.37. A visual inspection of figure 4.9 shows a possible BCG at S1 (RA: 00:34:33.19, DEC: 02:25:27.05), however this cannot be confirmed without spectroscopic data. S2 has no visible optical counterpart.

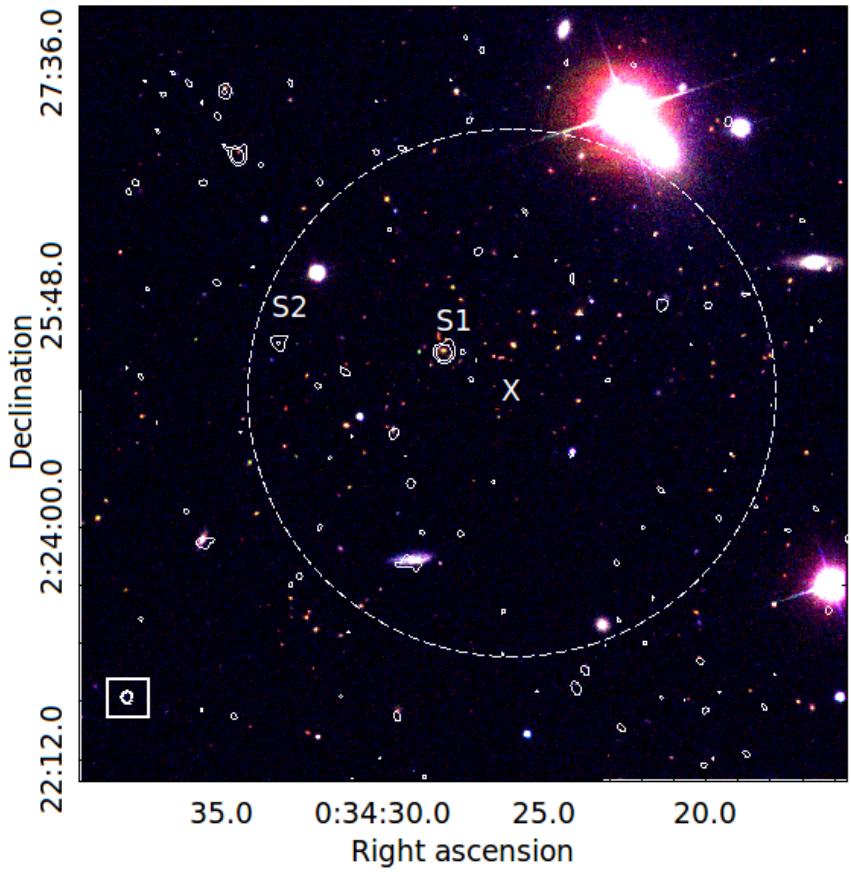

Figure 4.9: The SDSS image of J0034.4+0225 created using the compilation of the 3-colour *gri* images. The white contours denote the 37 μJy beam^{-1} 1σ noise of the cluster region of the primary beam corrected image, with contour levels of (3σ,9σ). The ellipse enclosed by a box represents the beam size of the contours with the corresponding colour. The dashed circle indicates the θ_{500} cluster region and the 'x' is the cluster center. The fluxes of S1 and S2 can be found in table 4.5.

4.4.2 ACT-CL J0239.9-0135

ACT-CL J0239.9-0135 is not a new ACTPol survey detection as it has been found in the Planck survey. This cluster had no archival XMM-Chandra data. After applying the uv constraints, there was no diffuse radio emission detected in both the first and the second

low-resolution images.

An extended radio source (labeled S2 in figure 4.10) was found in the cluster region. This radio source could not be removed by point source subtraction. This extended source is also visible in the low-resolution images. Five sources are imbedded in the extended emission seen in the low-resolution image. The sum of the fluxes of these five sources (S1 to S4 in table 4.7) is 22.30 ± 0.24 mJy. The flux measures for the extended emission is 26.83 ± 0.13 mJy. Although this flux is greater than that of the combined sources we cannot confirm that this flux is from diffuse emission as there might be embedded sources that are not picked up in the full resolution image. To confirm that this extended radio emission in the low-resolution images, is not real diffuse radio emission, the point source contours from the high-resolution image, overlaid in the low-resolution image, were found to coincide with the emission. This indicates that this emission is due to residual flux from the point sources. We summarize the noise and beam properties of figure 4.10 in table 4.6.

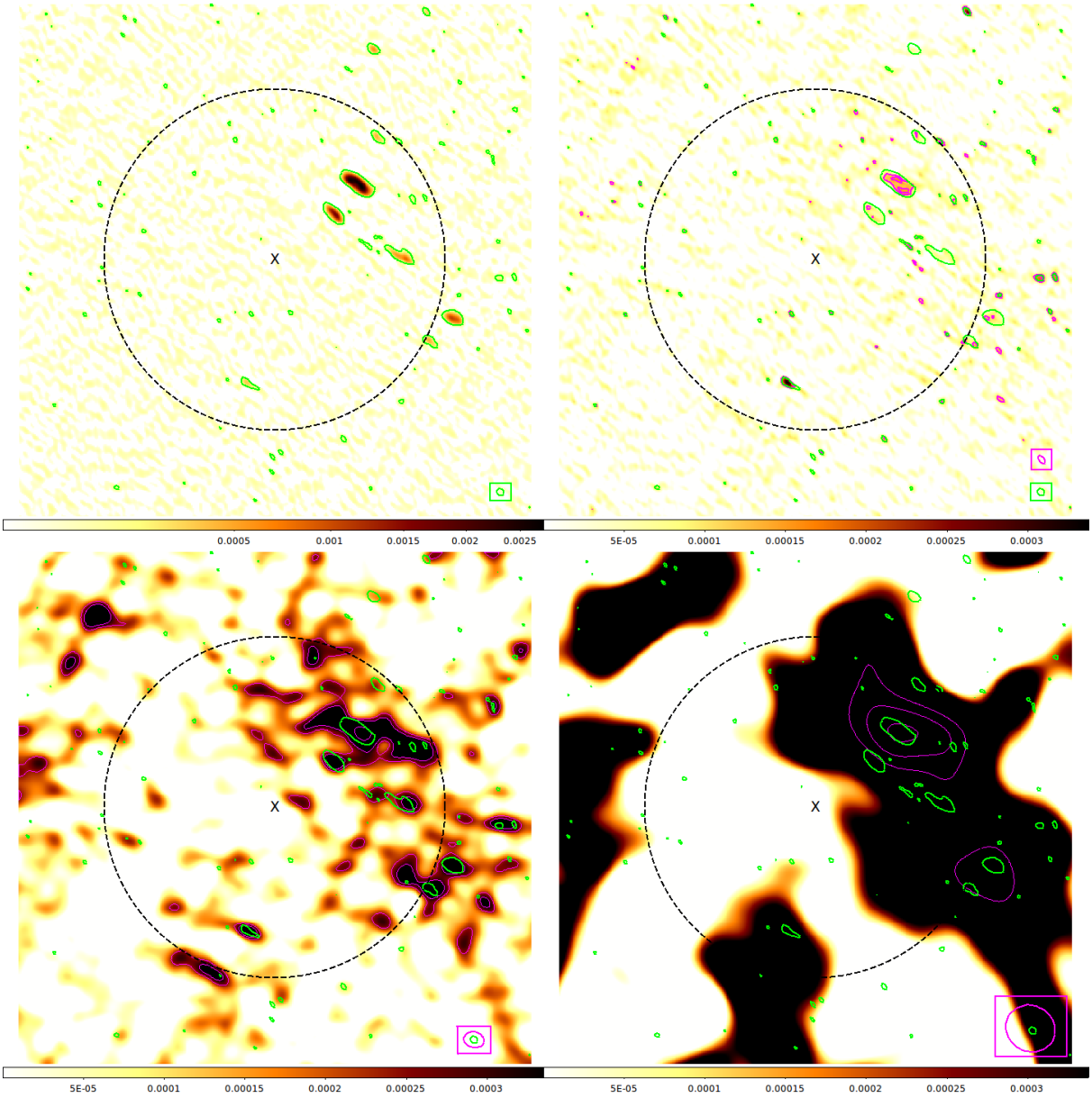

Figure 4.10: A gallery of the J0239.9-0135 cluster images produced during the low-resolution analysis. The colour units for the images are in Jy beam^{-1}. The black dashed indicates the θ_{500} cluster region with a diameter of 4.0′. The 'x' indicates the cluster center. The green contours indicate the point source emission and are at 3σ level, with the 1σ level corresponding to 40.1 μJy beam^{-1}. For all the images the magenta contours indicate diffuse radio emission detected above the noise level of the image. The ellipses enclosed by a box represent the beam size of the contours with the corresponding colour. *top left*: The high-resolution image with the point source contours. *top right*: Point source subtracted image. The image has a 1σ level of 35.3 μJy beam^{-1}, the contours show a 3 and 4 σ detection increasing inwards. *bottom left*: Point source subtracted low-resolution image (uv-taper 10 kλ). The diffuse radio emission is outlined with contour levels as follows: (3σ,4σ,5σ) increasing inwards. The 1σ level in this image corresponds to 80 μJy beam^{-1}. *bottom right*: Point source subtracted low-resolution image (uv-range cut $<$ 5 kλ, uv-taper 4 kλ). The diffuse radio emission is outlined with contour levels as follows: (3σ,4σ,5σ) increasing inwards. The 1σ level in this image corresponds to 540 μJy beam^{-1}.

Table 4.6: A summary of the image properties obtained in the diffuse radio emission search in the ACT-CL J0239.9-0135 cluster. This table contains image properties for the high-resolution, point source subtracted and low-resolution images.

Image Name	Beam Size ($'' \times ''$, p.a ^{o})	RMS Noise μJy beam^{-1}
HR	5.41 × 4.47, 40.16	40.1
PSSUBFR	6.62 × 3.79, 42.19	35.3
PSSUBLR1	14.45 × 10.90, 76.20	120.0
PSSUBLR2	35.42 × 32.07, 60.45	540.0

We then searched for point sources in the cluster region and measured their fluxes. In ds9 we used the FIRST survey (Helfand et al., 2015) to cross-match these compact sources. The FIRST survey has a primary beam size of ∼5" which is very similar to the GMRT, hence, when a source is cross-matched we were able to calculate the spectral index of the source. We further cross-matched these sources in the NVSS (Condon et al., 1998). For compact sources that were also detected in FIRST, we calculated the spectral index using

$$S_\nu \propto \nu^{-\alpha}. \tag{4.1}$$

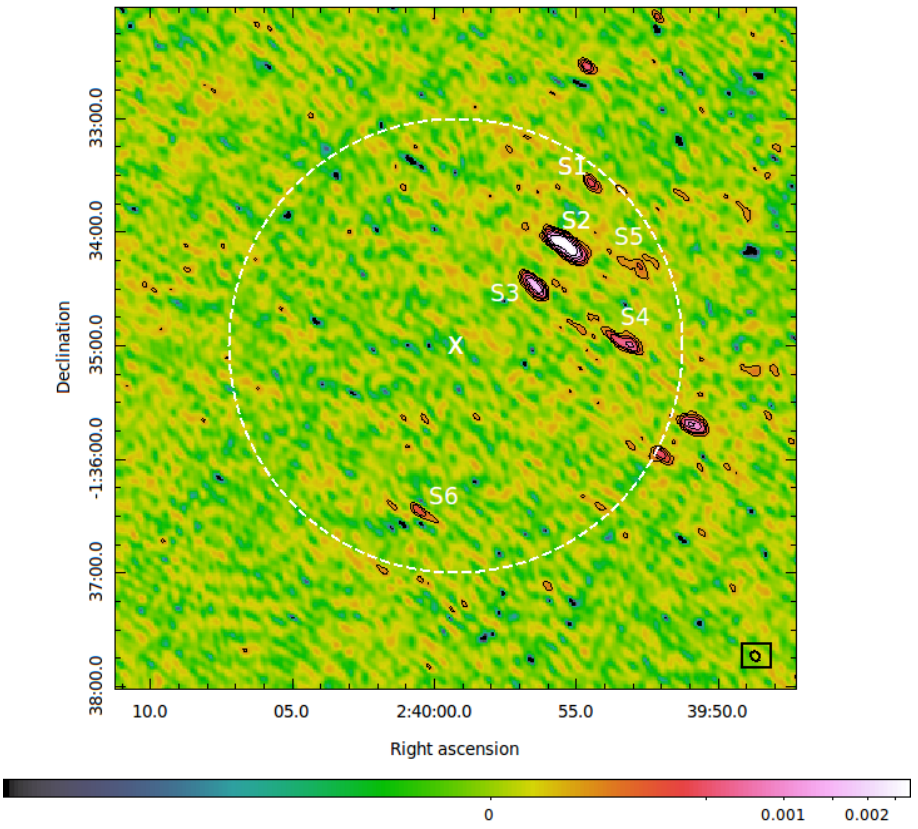

Figure 4.11: The θ_{500} cluster region of J0239.9-0135 is indicated by the dashed circle. The projected size of this region is 1.2 Mpc. The 'x' indicates the cluster center. The colour units for this image are in Jy beam^{-1}. The 1σ noise level in the cluster region corresponds to 37.5 μJy beam^{-1} and the contour level are (3σ,6σ,10σ,20σ,30σ,50σ). The beam size is (6.22$''$ $\times$ 3.79$''$) and the beam orientation angle is 42.20°, indicated by the ellipse enclosed by a box. The source fluxes, S1 to S3, can be found in table 4.7.

Table 4.7: The radio fluxes of the compact sources within the θ_{500} cluster region of J0239.9-0135, cross-matched with FIRST and NVSS.

Sources	RA [h:m:s]	DEC [d:m:s]	S_{610MHz} mJy	FIRST flux mJy	NVSS flux mJy	α_{610}^{1400}
S1	02:39:54.37	-01:33:35.85	0.76 ± 0.12	-	*10.69 ± 0.40	-
S2	02:39:55.30	-01:34:05.24	13.43 ± 0.22	3.41 ± 0.77	*	1.59
S3	02:39:56.50	-01:34:28.75	3.93 ± 0.16	0.85 ± 0.20	*	1.93
S4	02:39:53.33	-01:34:56.67	2.69 ± 0.21	2.11 ± 0.72	*	0.28
S5	02:39:52.66	-01:34:17.13	1.49 ± 0.23	-	*	-
S6	02:40:00.27	-01:36:30.00	0.40 ± 0.18	-	-	-

* The NVSS source corresponds to a combination of five GMRT sources: S1, S2, S3, S4 and S5.

Four sources were detected within the cluster region, as seen if figure 4.14. Three of the sources were found in FIRST, hence, we calculated the spectral indices for these sources.

In NVSS a source was that detected matched with the combination of all the four GMRT sources.

We proceeded to the SDSS image to cross-match for optical counterparts. A visual inspection of 4.12 show S2 (RA: 02:39:55.30, DEC: -01:34:05.24) as a possible BCG of the cluster, and S1, S3 to S6 could be galaxy cluster members, however this cannot be confirmed without spectroscopy.

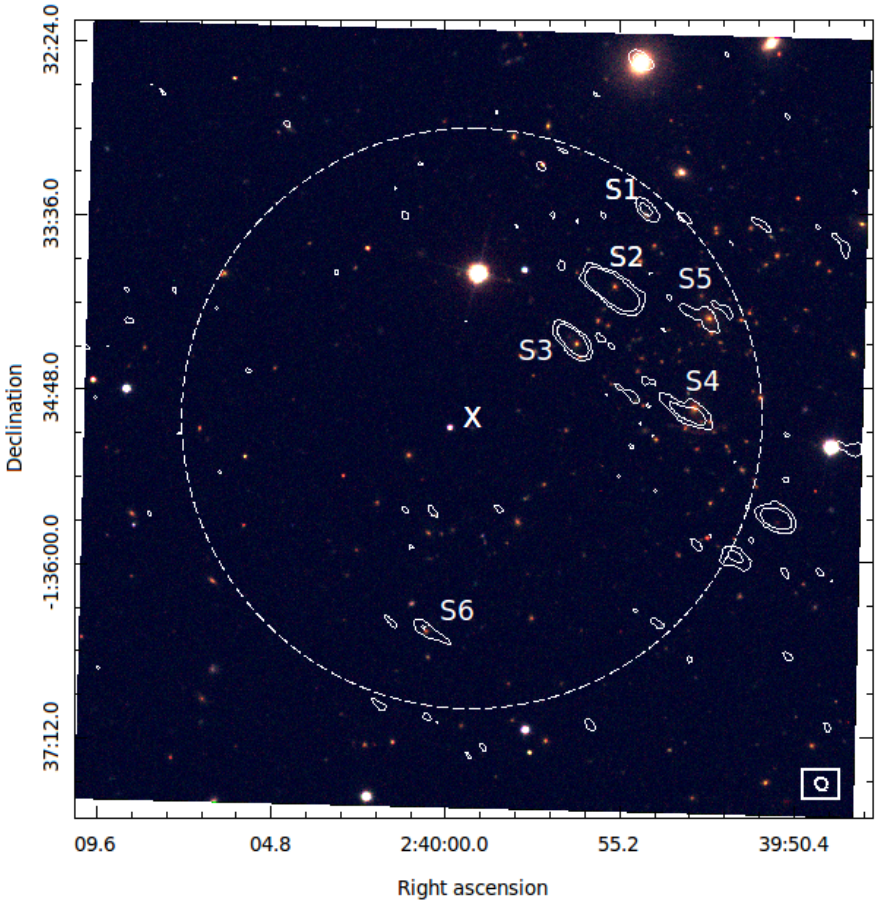

Figure 4.12: The SDSS image of J0239.9-0135 created using the compilation of the 3-colour *gri* images. The white contours denote the 37.5 μJy beam^{-1} 1σ noise of the cluster region of the primary beam corrected image, with contour levels of (3σ,9σ). The ellipse enclosed by a box represents the beam size of the contours with the corresponding colour. The dashed circle indicates the θ_{500} cluster region and the 'x' is the cluster center. The fluxes of S1 to S6 can be found in table 4.11.

4.4.3 ACT-CL J0140.0-0555

This cluster has been detected in the Planck SZ-selected cluster catalog and the archival X-ray data image revealed that it was dynamically disturbed. The different uv-range cuts

and tapers were applied and no diffuse radio emission was detected in the cluster region.

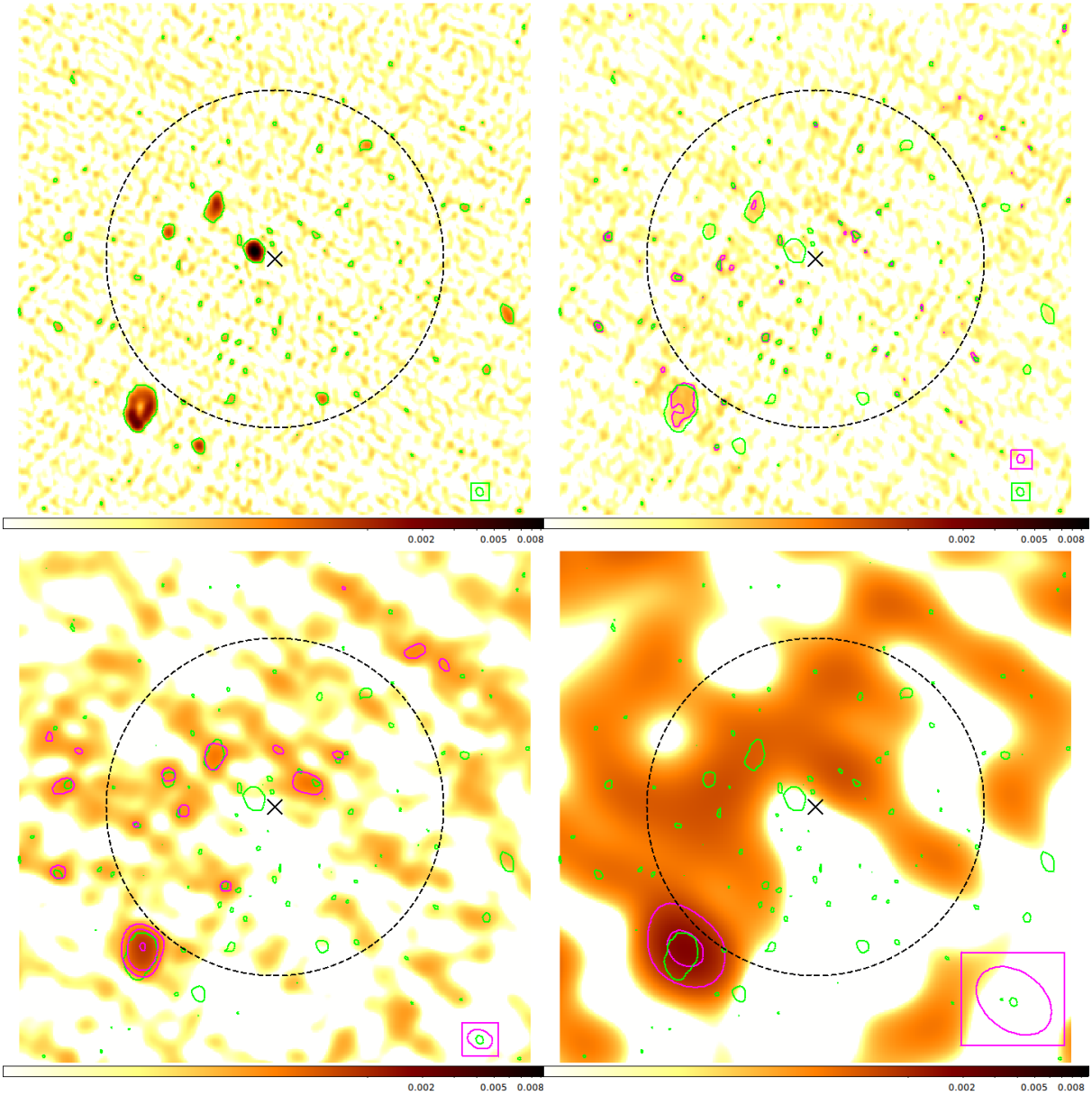

Figure 4.13: A gallery of the J0140.0-0555 images produced during the search for diffuse radio emission. The colour units for the images are in Jy beam^{-1}. The dashed circle indicates the θ_{500} cluster region with a diameter 3.3′. The 'x' indicates the cluster center. The green contours indicate the point source emission. The 1σ level in this image corresponds to 36 μJy beam^{-1} and the contour levels indicate a 3σ detection. For all the images the magenta contours indicate diffuse radio emission detected above the noise level of the image. The ellipses enclosed by a box represent the beam size of the contours with the corresponding colour. *top left*: The high-resolution image with the 3σ point source contours. *top right*: Point source subtracted image. The 1σ level in this image corresponds to 31 μJy beam^{-1} and the contour levels increase inwards in levels (3σ,6σ). *bottom left*: Point source subtracted low-resolution image (uv-taper 10 kλ). The magenta contours indicate emission at (3σ,6σ,12σ) with a 1σ level of 70 μJy beam^{-1}. *bottom right*: Point source subtracted low-resolution image (uv-range cut < 5 kλ, uv-taper 4 kλ). The magenta contours indicate a detection of (3σ,6σ,12σ) increasing inwards, with a 1σ of 240 μJy beam^{-1}.

In figure 4.13 are the high-resolution, point source subtracted, and low-resolution images, zoomed into the cluster region followed by the noise and beam properties in table 4.8.

Table 4.8: A summary of the image properties obtained in the diffuse radio emission search in the ACT-CL J0140.0-0555 cluster. This table contains image properties for the high-resolution, point source subtracted and low-resolution images.

Image Name	Beam Size ($'' \times ''$, p.a ^{o})	RMS Noise μJy beam^{-1}
HR	4.95 × 4.03, 17.45	38.0
PSSUBFR	5.33 × 4.45, 12.52	30.6
PSSUBLR1	14.96 × 10.65, 70.59	69.8
PSSUBLR2	48.69 × 34.34, 53.84	240.0

A final step in the radio analysis of this cluster would be to do simulations by injecting 'fake' halos in the cluster region, and hence, calculate the diffuse radio emission upper limits.

To conclude our radio analysis study we searched for compact sources within the cluster region. We found that there were five sources in the cluster region and proceeded to measure their fluxes and cross-matched them in the NVSS and FIRST surveys.

Only one source was cross-matched in the FIRST survey. Since this survey has a similar primary beam size ($\sim 5''$) compared to GMRT we proceeded to calculate the spectral index of the source. In NVSS one large source corresponded to a combination of three sources. This is because the NVSS has a much larger primary beam ($\sim 45''$) compared to GMRT (Condon et al., 1998). A summary of the flux measurements is given in table 4.9.

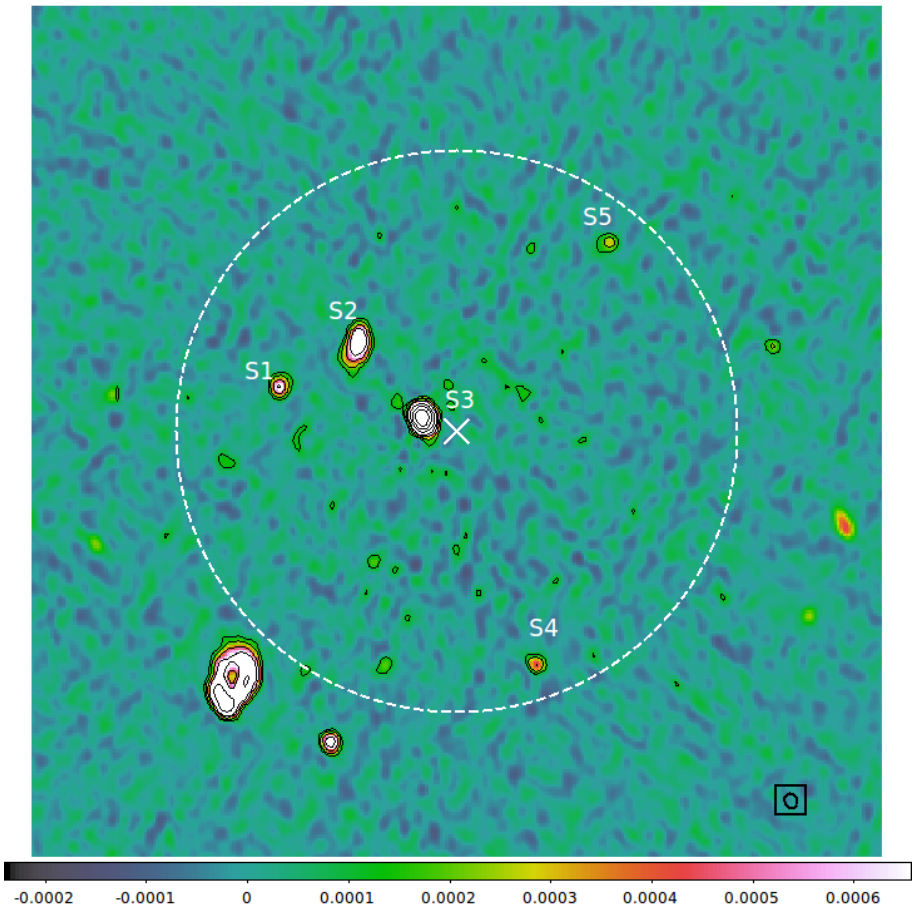

Figure 4.14: The J0140.0-0555 θ_{500} cluster region is indicated by the dashed circle. The projected size of this region is 1.0 Mpc. The 'x' indicates the cluster center. The colour units for this image are in Jy beam^{-1}. The 1σ noise level in the cluster region is 36.0 μJy beam^{-1} and the contour level are (3σ,6σ,12σ,20σ,50σ,200σ). The beam size corresponds to (5.32$''$ $\times$ 4.44$''$) and the beam orientation angle is 12.52° indicated by the ellipse enclosed by a box. The source fluxes, S1 to S5, can be found in table 4.9.

Table 4.9: The radio fluxes of the compact sources within the θ_{500} cluster region of J0140.0-0555, cross-matched with FIRST and NVSS.

Sources	RA [h:m:s]	DEC [d:m:s]	S_{610MHz} mJy	FIRST flux mJy	NVSS flux mJy	α_{610}^{1400}
S1	01:40:04.16	-05:54:52.23	0.91 ± 0.12	-	*12.41 ± 1.43	-
S2	01:40:02.35	-05:54:38.77	3.31 ± 0.13	-	*	-
S3	01:40:00.77	-05:55:03.54	16.35 ± 0.12	4.89 ± 0.39	*	1.46
S4	01:39:58.09	-05:56:30.23	0.38 ± 0.10	-	-	-
S5	01:39:39.80	-05:54:02.16	0.42 ± 0.10	-	-	-

* The NVSS source corresponded to a combination of three GMRT sources: S1, S2 and S3.

We searched for optical counterparts of the compact sources found in figure 4.14. A visual inspection of 4.15 shows a possible BCG at S3 (RA: 01:40:00.77, DEC: -05:55:03.54). S5 in the radio image possibly corresponds with a blue foreground source, however this

cannot be confirmed without spectroscopic data. The rest of these radio sources had no visible optical counterparts.

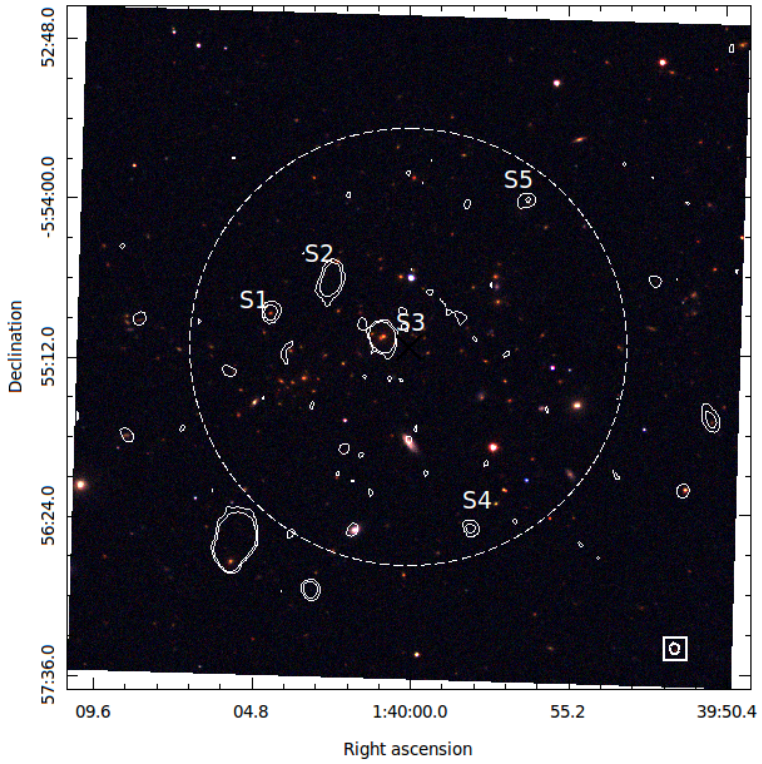

Figure 4.15: The SDSS image of the J0140.0-0555 cluster created using the compilation of the 3-colour *gri* images. The white contours denote the 36.0 μJy beam^{-1} 1σ noise level in the cluster region of the primary beam corrected image, with contour levels of (3σ,9σ). The ellipse enclosed by a box represents the beam size of the contours with the corresponding colour. The dashed indicates the θ_{500} cluster region and the 'x' is the cluster center. The fluxes of S1 to S5 can be found in table 4.9.

4.4.4 ACT-CL J0137.4-0827

ACT-CL J0137.4-0827 is a new ACTPol survey detection and is not detected in any of the Planck SZ and SPT cluster catalogs. The archival XMM-Chandra data showed that this cluster is dynamically disturbed. The ACT-CL J0137.4-0827 cluster is the least massive cluster in our sample and is at the highest redshift (z = 0.57). In applying the low-resolution imaging analysis we found that this cluster hosted diffuse radio emission. Figure 4.16 shows the high-resolution, point source subtracted full-resolution and low-resolution image. The tentatively detected extended radio emission is located along the cluster center. Table 4.10 indicates the noise and beam properties of these images.

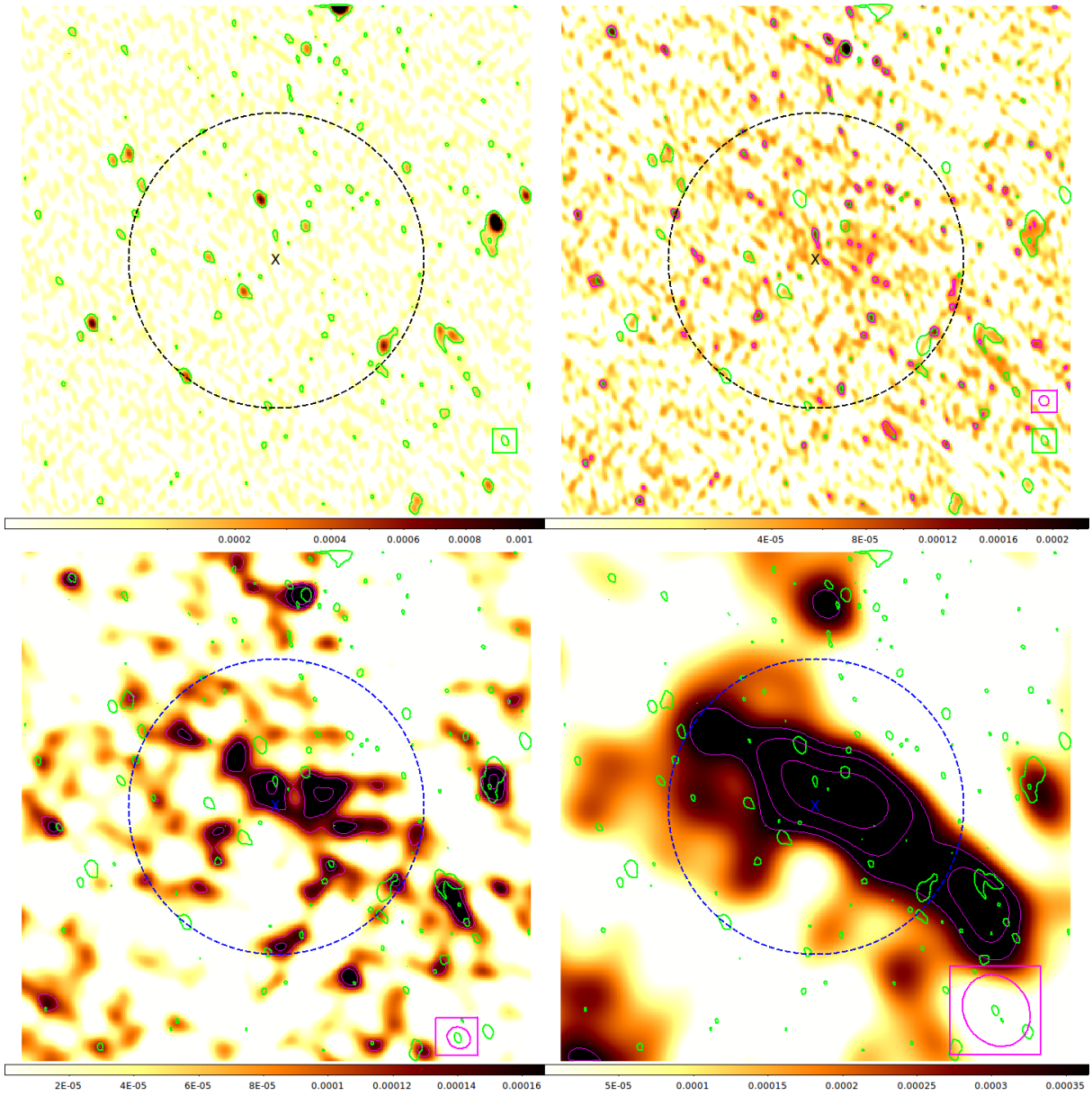

Figure 4.16: A gallery of the images produced when searching for diffuse radio emission in J0137.4-0827, The dashed circle indicates the θ_{500} cluster region with a diameter of 2.9′. The colour units for the images are in Jy beam^{-1}. The 'x' indicates the cluster center. The green contours indicate the point source emission. 3σ level is 75 μJy beam^{-1}. For all the images the magenta contours indicate diffuse radio emission detected above the noise level of the image. The ellipses enclosed by a box represent the beam size of the contours with the corresponding colour. *top left*: The high-resolution image with point source contours overlaid. *top right*: Point source subtracted image. The 1σ noise level is 20 μJy beam^{-1} and the contours indicate diffuse radio emission detection of 3σ. *bottom left*: Point source subtracted low-resolution image (uv-taper 10 kλ). The 1σ noise level in this image corresponds to 40 μJy beam^{-1} and the contours indicate diffuse radio emission detection of (3σ,4σ,6σ). *bottom right*: Point source subtracted low-resolution image (uv-range cut < 5 kλ, uv-taper 4 kλ). The 1σ noise level in this image corresponds to 120 μJy beam^{-1} and the contours indicate diffuse radio emission detection of (3σ,4σ,6σ).

Table 4.10: A summary of the image properties obtained in the diffuse radio emission search in the ACT-CL J0137.4-0827 cluster. This table contains image properties for the high-resolution, point source subtracted and low-resolution images.

Image Name	Beam Size ($'' \times ''$, p.a ^{o})	RMS Noise μJy beam^{-1}
HR	5.61 × 3.66, 22.77	24.5
PSSUBFR	6.19 × 5.75, 25.04	19.4
PSSUBLR1	14.03 × 12.11, 58.78	40.0
PSSUBLR2	44.09 × 37.67, 34.38	120.0

In the low-resolution image, we found evidence of faint diffuse radio emission. This emission is extended and is located in the central region of the cluster. We could not immediately categorize the detected diffuse radio emission due to its morphology and position not directly falling under GRH or RR category. It is not of spherical shape and although some GRHs have an irregular shape, this source is rather too elongated to be considered as a GRH. It is also located along the cluster's SZ peak and hence cannot be categorized as a radio relic. A multiwavelength study and a radio follow up with higher sensitivity will help in the classification of this tentatively detected extended radio source. From the current data, we assume that it is possibly AGN radio lobes. We make this assumption because of the location and the symmetry of the extended radio emission.

We then searched for compact sources in the cluster region and detected six sources, as shown in figure 4.17. We did a cross-match of these sources using the FIRST and NVSS surveys. None of the sources were cross-matched in the FIRST survey. In NVSS we found that one source in the cluster region contained emission from three of the GMRT sources, however, due to the difference in primary beam sizes we did not calculate the spectral indices for these sources. A summary of the measurements of the radio fluxes is presented in table 4.11.

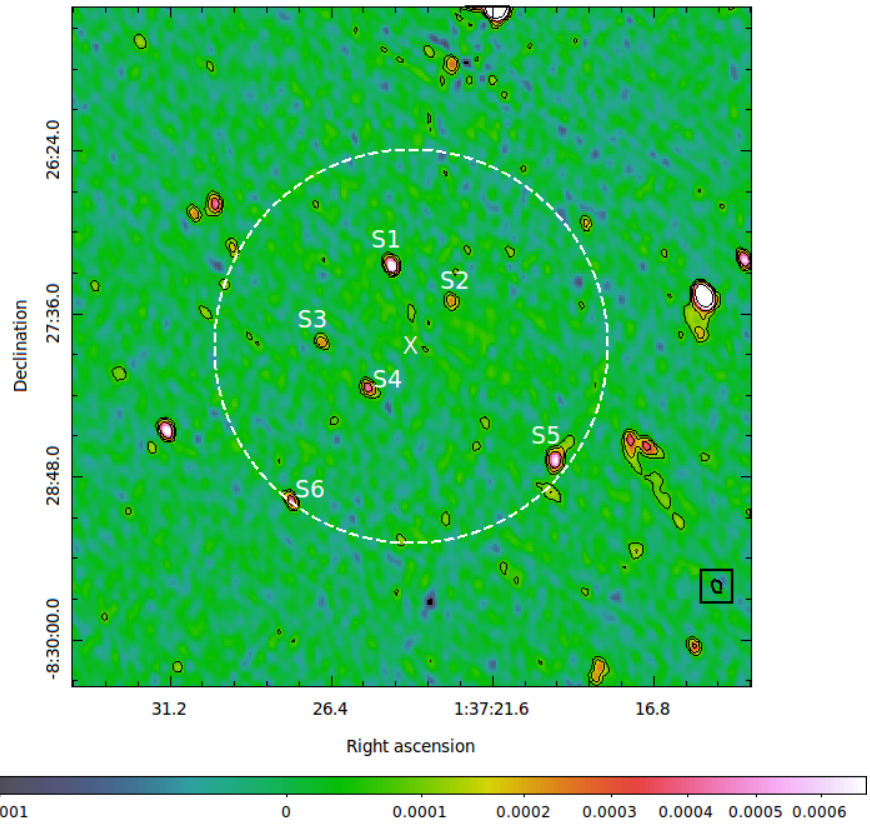

Figure 4.17: The J0137.4-0827 θ_{500} cluster region is indicated by the dashed circle. The projected size of this region is 0.90 Mpc. The 'x' indicates the cluster center. The colour units for this image are in Jy beam^{-1} The 1σ noise level in the cluster region is 23.33 μJy beam^{-1} and contours levels detect emission at (3σ,6σ,12σ,24σ). The beam size is (6.19$''$ $\times$ 4.17$''$) and the beam orientation angle is 23.04° indicated by the ellipse enclosed by a box. The source fluxes, S1 to S3, can be found in table 4.11.

Table 4.11: The radio fluxes of the compact sources within the θ_{500} cluster region of J0137.4-0827, cross-matched with FIRST and NVSS.

Sources	RA [h:m:s]	DEC [d:m:s]	S_{610MHz} mJy	NVSS flux mJy
S1	01:37:24.57	-08:27:14.02	0.90 ± 0.06	*1.3 ± 0.22
S2	01:37:22.80	-08:27:31.00	0.32 ± 0.06	-
S3	01:37:26.64	-08:27:49.20	0.17 ± 0.06	*
S4	01:37:25.17	-08:28:09.42	0.49 ± 0.06	*
S5	01:37:19.71	-08:28:40.55	0.97 ± 0.06	-
S6	01:37:27.54	-08:28:58.34	0.40 ± 0.06	-

* The NVSS source corresponded to a combination of three GMRT sources: S1, S3 and S4.

We searched for optical counterparts of the compact sources in the SDSS archival data. Figure 4.18 shows that S2 has no visible optical counterpart. Sources S1, S3, S4 and S5, from colour inspection, could all be galaxy cluster members, however this cannot be confirmed without spectroscopy.

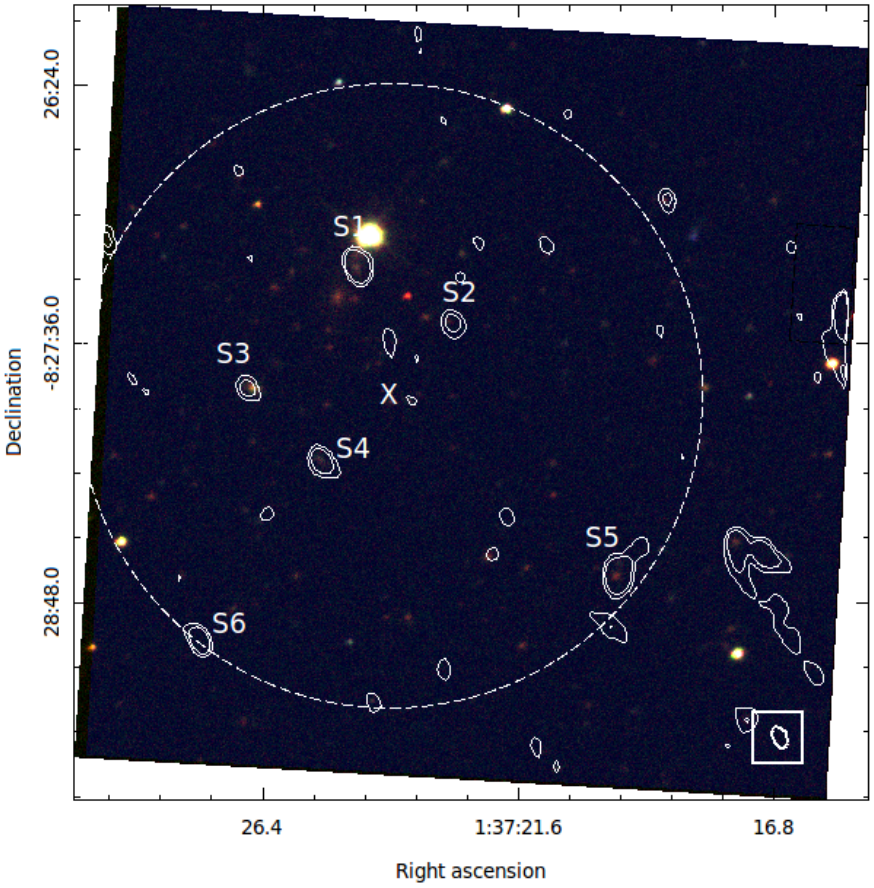

Figure 4.18: The SDSS image of J0137.4-0827 created using the compilation of the 3-colour *gri* images. The white contours denote the 23.33 μJy beam^{-1} 1σ noise of the cluster region of the primary beam corrected image, with contour levels of (3σ,9σ). The ellipses enclosed by a box represent the beam size of the contours with the corresponding colour. The dashed circle indicates the θ_{500} cluster region and the 'x' is the cluster center. The fluxes of S1 to S5 can be found in table 4.11.

CHAPTER 5

Conclusion and Future Work

Current generation cosmology and astrophysics studies are largely focused on constraining and understanding the ΛCDM model. Galaxy cluster counts play a major role in constraining dark energy, which is the dominant component in the current epoch. It is therefore very important that galaxy clusters and their evolution are fully understood in order to accurately constrain dark energy models. The understanding of these cluster systems is directly dependent on the understanding of the intracluster medium (ICM). Diffuse radio emission provides a unique insight into the evolution and energetics of the intracluster medium.

The aim of this thesis was to search for diffuse radio emission in the uniformly selected ACTPol cluster sample. Our sample was a sub-sample of a pilot project (PI: Dr.K. Knowles) which aims to obtain a statistically complete ACTPol sample. This sample consists of 16 uniformly selected clusters, eight of which already have archival GMRT data. We proposed to observe the remaining eight in GMRT cycle 30 observations. We were successful in observing GMRT data on four of these clusters, the analysis of which is presented in this thesis. With this complete sample, scaling relations of diffuse radio emission in SZ-selected clusters will be investigated.

We began by giving a theoretical background of the cosmological model in Chapter 2. We provided a literature review of galaxy cluster formation and evolution and highlighted the importance of galaxy clusters as cosmological probes. We pointed out the key future surveys, such as the SKA, that will improve the observation and detection of galaxy clusters.

Finally, we discussed the formation theories for non-thermal diffuse radio emission in the form of giant radio halos, radio mini-halos, and radio relics. In Chapter 3 we provided an overview of the analysis methods in radio astronomy. We paid attention to the CLEAN algorithm and the SPAM software package.

In Chapter 4 we briefly reviewed the GMRT specifications and indicated why this interferometer is ideal for diffuse radio emission observations. We gave a brief review of the ACT project with a focus on its detection of galaxy clusters via the thermal SZ effect. There were 75 clusters that were detected in our field with an SZ SNR > 5. We then introduced our uniformly selected cluster sample which consisted of 16 clusters that were obtained by applying a mass cut of $M_{500} > 4{\times}10^{14}$ $M_{\odot}$ and a redshift cut of $z < 0.6$. From our sample, eight clusters had existing GMRT archival data. We briefly discussed the eight clusters with archival data. We applied to observe the remaining clusters using the GMRT telescope.

The GMRT data was reduced using the SPAM software package. Our final images had lower noise than anticipated, hence, we detected many point sources in the cluster region. We did a search for point sources in the cluster region of our sample and cross-matched them with the NVSS and FIRST surveys. For those sources that were found in FIRST, we calculated the spectral indices. We detected optical counterparts for these sources using SDSS. These sources were either BCGs, cluster members, background sources or foreground sources. After a systematic search for diffuse radio emission in the short baseline visibilities, we found that two of the clusters hosted diffuse radio emission. This diffuse radio emission was detected in the low-resolution images for both the clusters. We obtained the low-resolution images by applying a uv-taper at 10 kλ. We did not categorize the diffuse radio emission hosted in both the clusters because they did not match the observational characteristics radio halos or radio relics. We conclude that a higher sensitivity radio observation follow-up will improve the noise levels of the low-resolution images, which will give a clearer indication of what these objects are. We also required a multiwavelength study in order to fully understand the dynamics of these cluster systems. Once we observe the complete sample we will be able to do a statistical study of the sample, as a precursor to a larger ACTPol cluster study.

5.1 Future Work

Non-thermal diffuse radio emission in the ICM is important for both astrophysical and cosmological studies. Understanding the ICM will improve the theory of plasma physics

and our understanding of galaxy cluster evolution. Using the SZ signal as a mass selection proxy has proven to be a robust technique compared to the X-ray luminosity selection proxy. It is, therefore, important that statistically complete cluster samples are used to measure the scaling relations of the SZ-selected clusters. These will be important for the development of formation theories of the non-thermal diffuse radio emission and to see how these scaling relations compare to the X-ray selected cluster samples. The main goal of our study is to observe the complete sample of the ACTPol SZ-selected clusters and calculate scaling relations from this sample.

To complete the study on the cluster sample presented in this thesis we need to calculate upper limits for the clusters with undetected diffuse radio emission and undertake multiwavelength studies of the clusters with diffuse radio emission. We then aim to obtain follow-up observations of the four clusters presented here, and the remaining four unobserved clusters in the sample of 16 clusters, using the upgraded Giant Metrewave Radio Telescope uGMRT (Rao Bandari et al., 2013) which will have three times more sensitivity and a larger bandwidth. A better sensitivity for our observations will result in a more accurate interpretation of the diffuse radio emission signal. To carry out the multiwavelength studies of these clusters, we will obtain X-ray data from the Chandra telescope (Weisskopf et al., 2002) which will give us an insight of the morphology of these systems. In addition, optical spectroscopy will be essential for our multiwavelength studies as it will provide the spectroscopic information for cluster members, which will allow us to understand the internal dynamics of the cluster. We will then derive scaling relations for our complete sample, including the clusters observed in this thesis, and compare our results to those of X-ray selected cluster samples. Comparing these results will also indicate if the bimodality observed in the X-ray cluster samples also exists in the SZ clusters samples.

To advance the study of diffuse radio emission in galaxy clusters, we plan to observe clusters at high redshift and low mass. Due to limited telescope sensitivity, clusters that exist in such regimes have not been studied yet, hence, their behaviour is not fully understood. However, with the upcoming generation of radio telescopes, we will be able to observe these, high redshift and low mass clusters. Our goal is to observe a much larger ($\sim$200) sample of ACTPol and Advance ACT clusters using the MeerKAT telescope (Brederode et al., 2016). From this sample, we will be able to study the formation and evolution of diffuse radio emission in very high redshift and low mass clusters. These studies will further validate or disprove the current formation models.

APPENDIX A

Full Field Of View GMRT Images

In Appendix A we have inserted all the images of the newly observed four clusters. We include the primary beam corrected full resolution images, high resolution images, point source subtracted full resolution images and point source subtracted low-resolution images.

A.1 ACT-CL J0034.4+0225

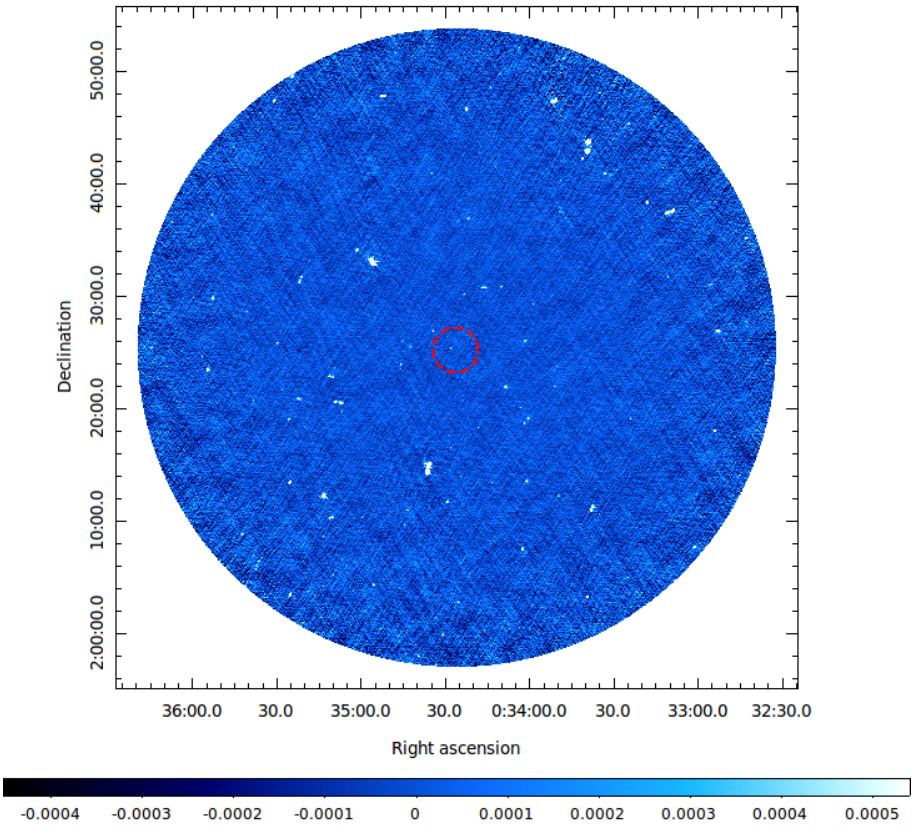

Figure A.1: The full-resolution image of the primary beam corrected ACT-CL J0034.4+0225. The red circle indicates the SZ cluster scale, $\theta_{500} = 4.1'$ centered at the SZ peak. The rms noise level of the full image is 34.6 μJy beam^{-1}. The colour units for this image are in Jy beam^{-1}.

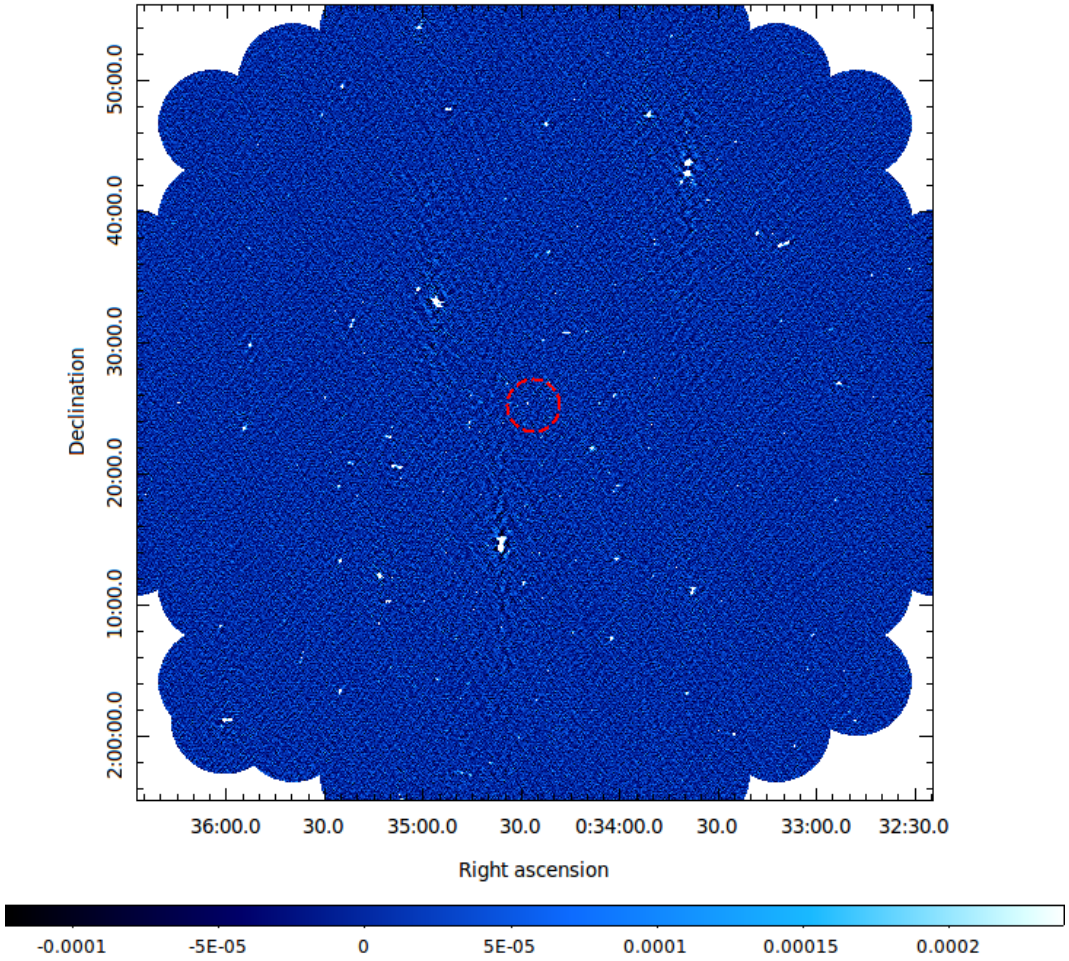

Figure A.2: The full field of view of the high-resolution image of ACT-CL J0034.4+0225. The red circle indicates the SZ cluster scale, $\theta_{500} = 4.1'$ centered at the SZ peak. The rms noise level of the full image is 42.0 μJy beam^{-1}. The colour units for this image are in Jy beam^{-1}.

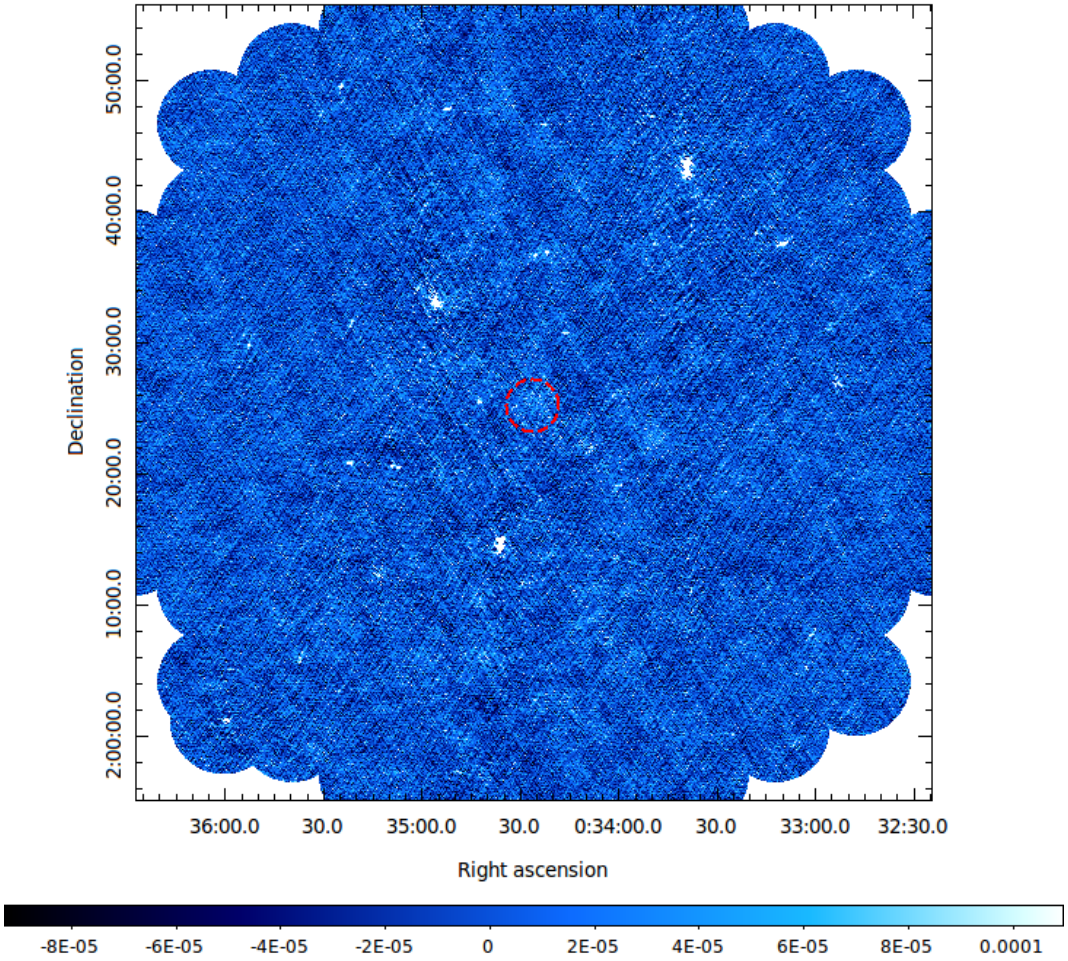

Figure A.3: The full-resolution image of the point source subtracted ACT-CL J0034.4+0225 field. The red circle indicates the SZ cluster scale, $\theta_{500} = 4.1'$ centered at the SZ peak. The rms noise level of the full image is 35.0 μJy beam^{-1}. The colour units for this image are in Jy beam^{-1}.

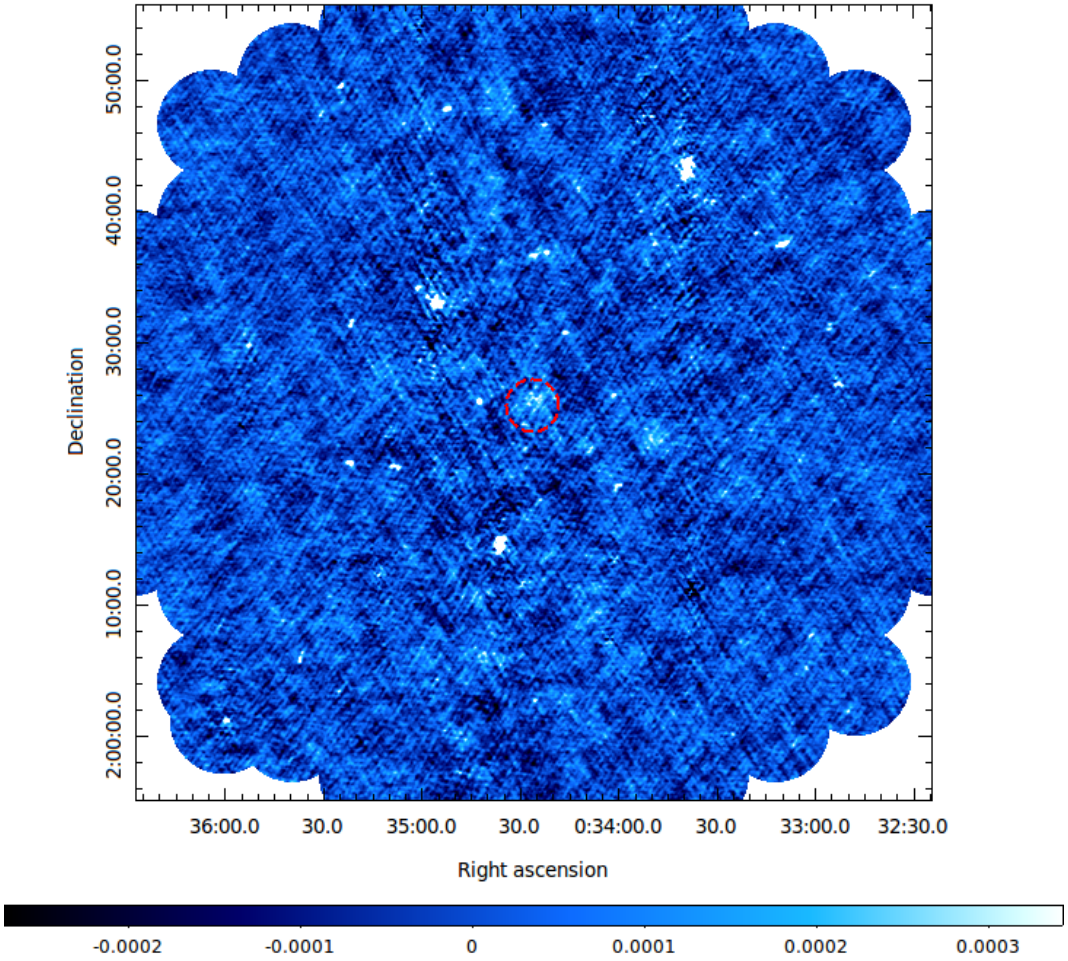

Figure A.4: The low-resolution image of the point source subtracted ACT-CL J0034.4+0225 field. A uv-taper at 10 kλ was applied. The red circle indicates the SZ cluster scale, $\theta_{500} = 4.1'$ centered at the SZ peak. The rms noise level of the full image is 70.0 μJy beam^{-1}. The colour units for this image are in Jy beam^{-1}.

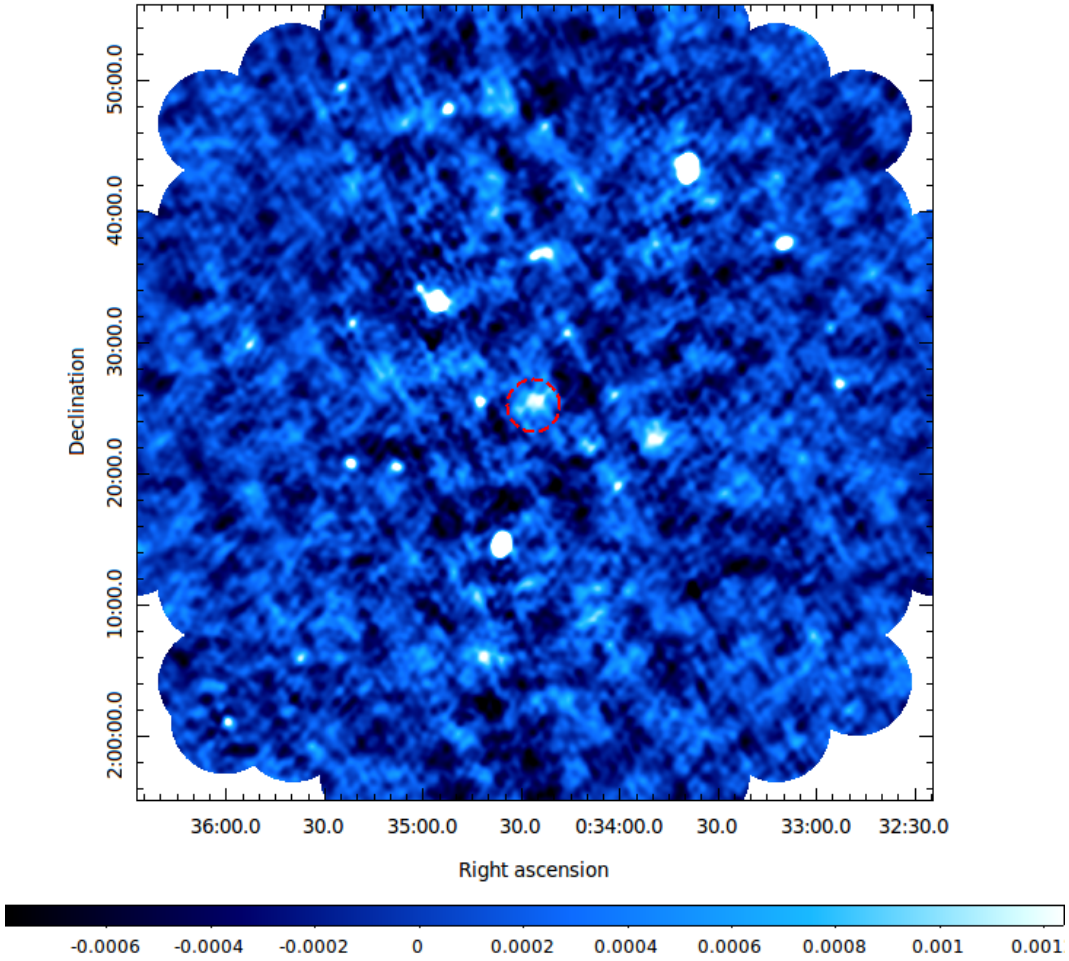

Figure A.5: The low-resolution image of the point source subtracted ACT-CL J0034.4+0225 field. The following uv restrictions were applied: uv-range < 5 kλ and uv-taper at 4 kλ. The red circle indicates the SZ cluster scale, $\theta_{500} = 4.1'$ centered at the SZ peak. The rms noise level of the full image is 240 μJy beam^{-1}. The colour units for this image are in Jy beam^{-1}.

A.2 ACT-CL J0239.9-0135

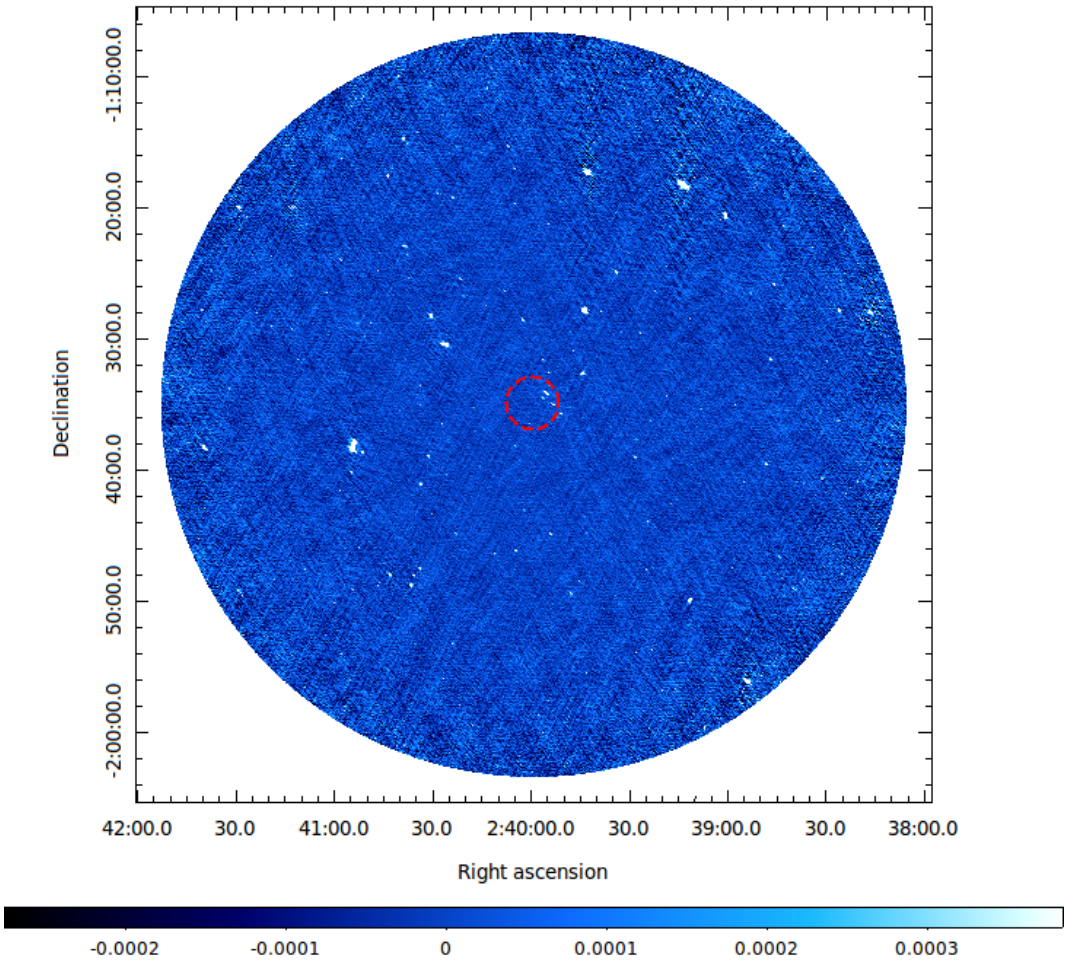

Figure A.6: The full-resolution image of the primary beam corrected ACT-CL J0239.9-0135. The red circle indicates the SZ cluster scale, $\theta_{500} = 4.0'$ centered at the SZ peak. The rms noise level of the full image is 37.89 μJy beam^{-1}. The colour units for this image are in Jy beam^{-1}.

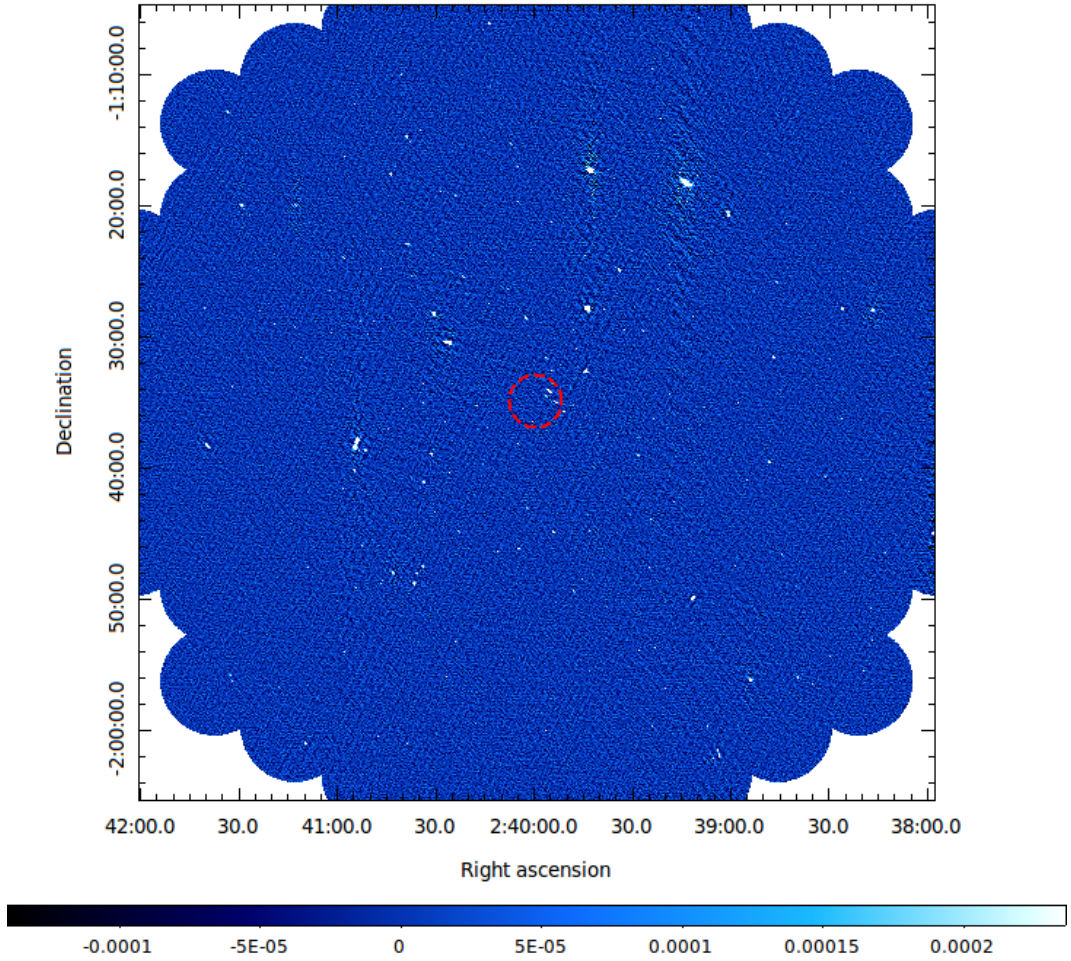

Figure A.7: The full field of view of the high-resolution image of ACT-CL J0239.9-0135. The red circle indicates the SZ cluster scale, $\theta_{500} = 4.0'$ centered at the SZ peak. The rms noise level of the full image is 40.1 μJy beam^{-1}. The colour units for this image are in Jy beam^{-1}.

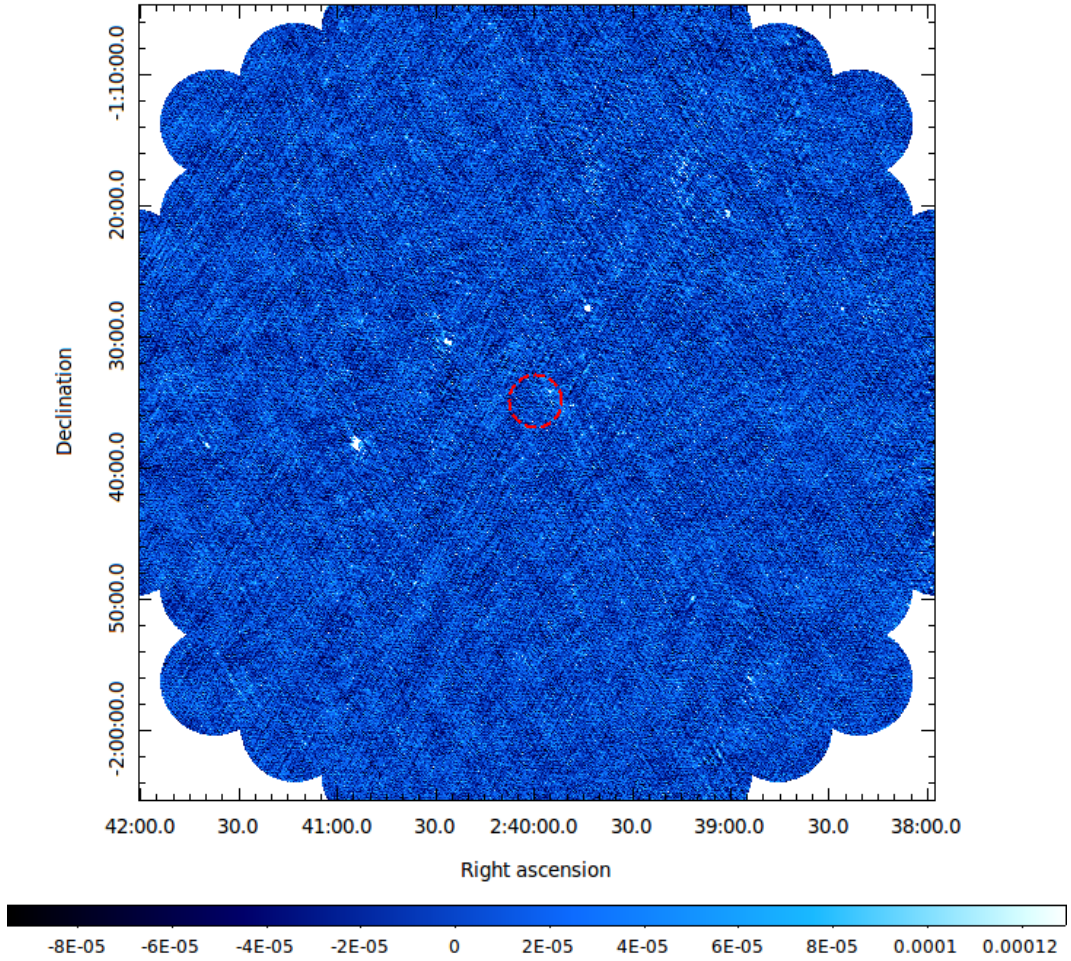

Figure A.8: The full-resolution image of the point source subtracted ACT-CL J0239.9-0135 field. The red circle indicates the SZ cluster scale, $\theta_{500} = 4.0'$ centered at the SZ peak. The rms noise level of the full image is 35.3 μJy beam^{-1}. The colour units for this image are in Jy beam^{-1}.

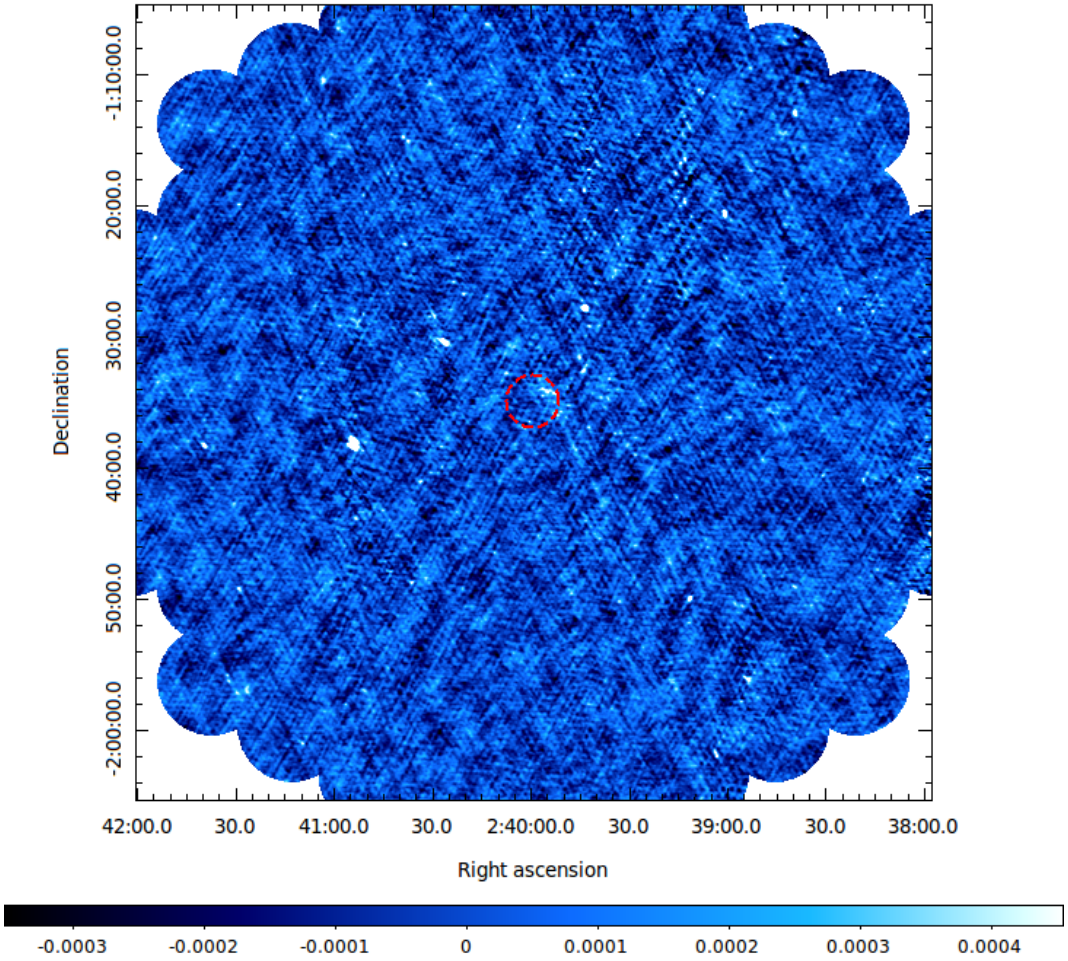

Figure A.9: The low-resolution image of the point source subtracted ACT-CL J0239.9-0135 field. A uv-taper at 10 kλ was applied. The red circle indicates the SZ cluster scale, $\theta_{500} = 4.0'$ centered at the SZ peak. The rms noise level of the full image is 80.3 μJy beam^{-1}. The colour units for this image are in Jy beam^{-1}.

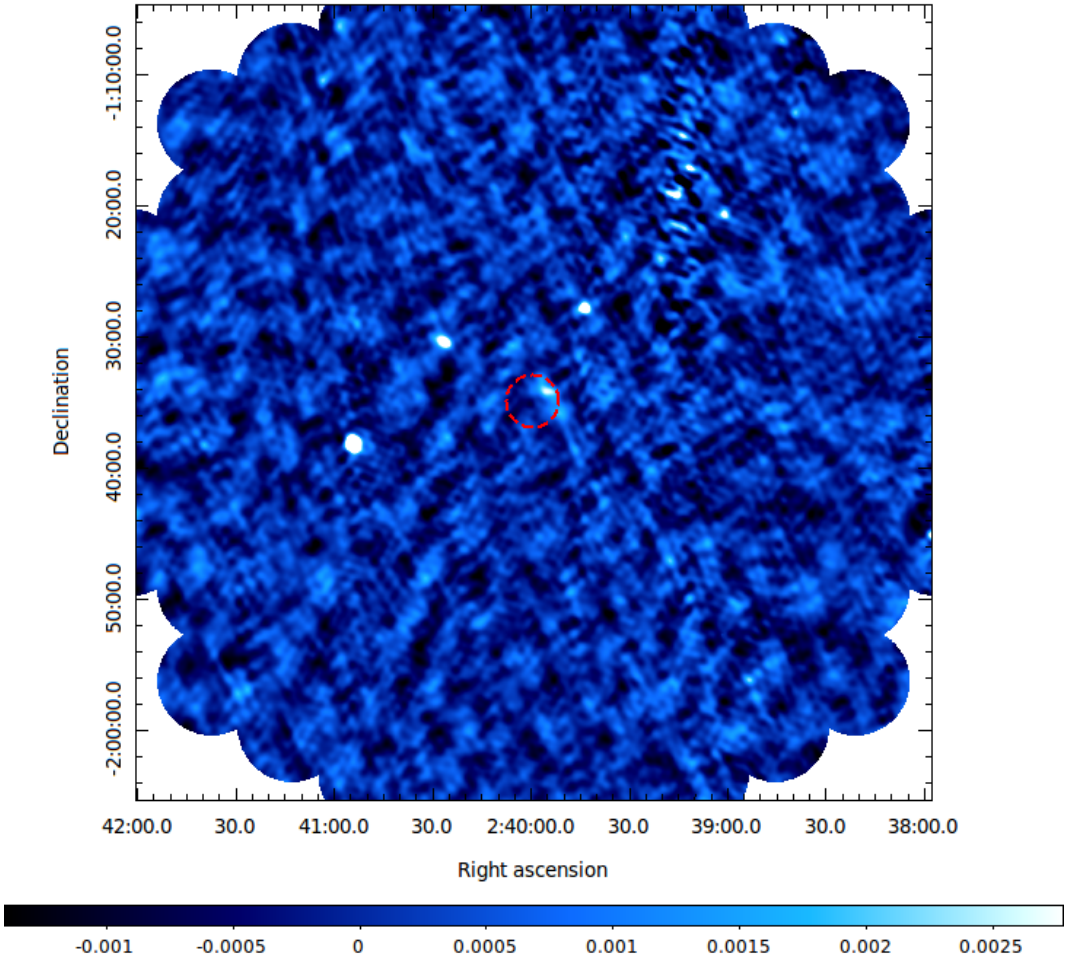

Figure A.10: The low-resolution image of the point source subtracted ACT-CL J0239.9-0135 field. The following uv restrictions were applied: uv-range < 5 kλ and uv-taper at 4 kλ. The red circle indicates the SZ cluster scale, $\theta_{500} = 4.0'$ centered at the SZ peak. The rms noise level of the full image is 540 μJy beam^{-1}. The colour units for this image are in Jy beam^{-1}.

A.3 ACT-CL J0140.0-0555

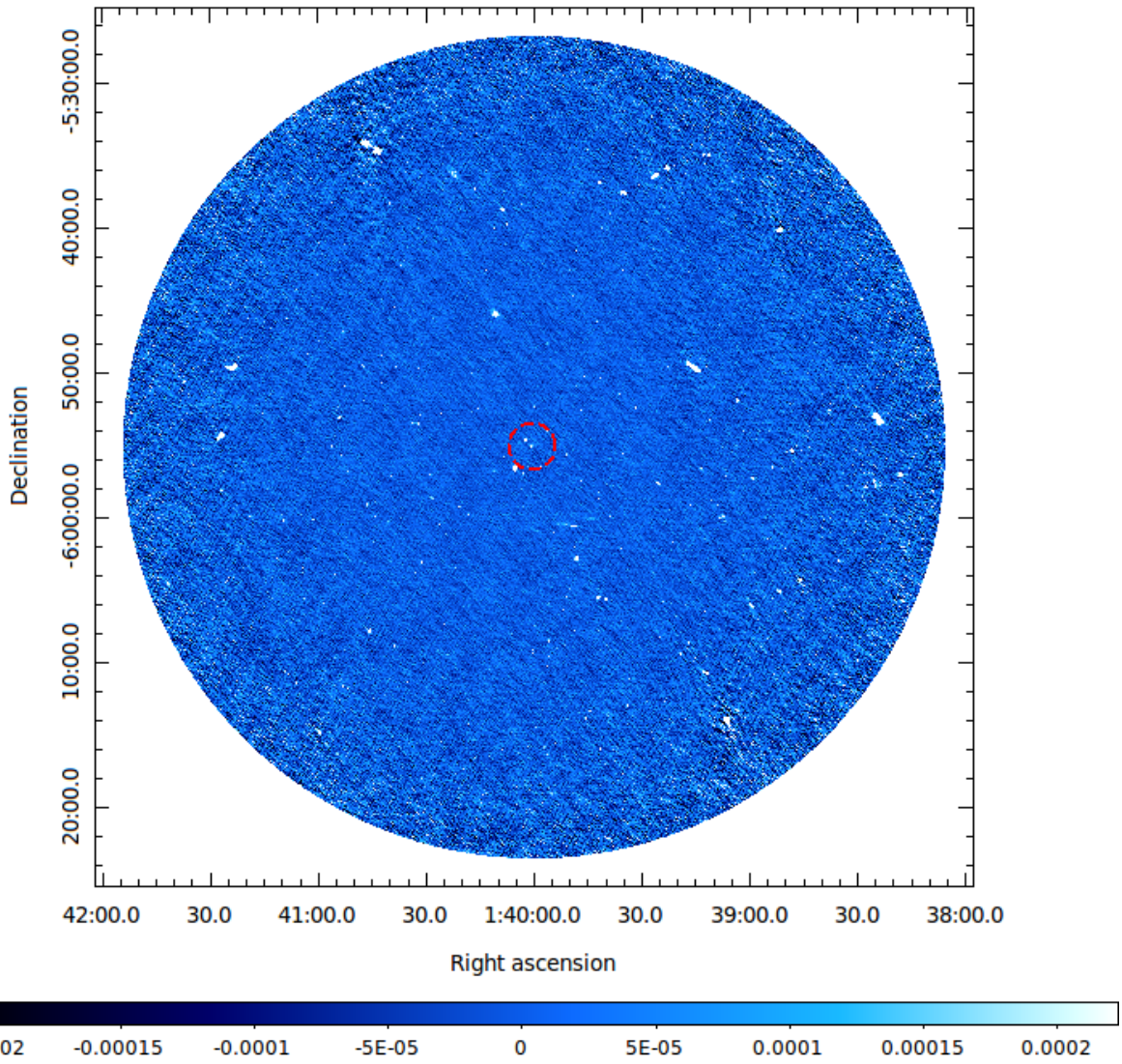

Figure A.11: The full-resolution image of the primary beam corrected ACT-CL J0140.0-0555. The red circle indicates the SZ cluster scale, $\theta_{500} = 3.3'$ centered at the SZ peak. The rms noise level of the full image is 34.0 μJy beam^{-1}. The colour units for this image are in Jy beam^{-1}.

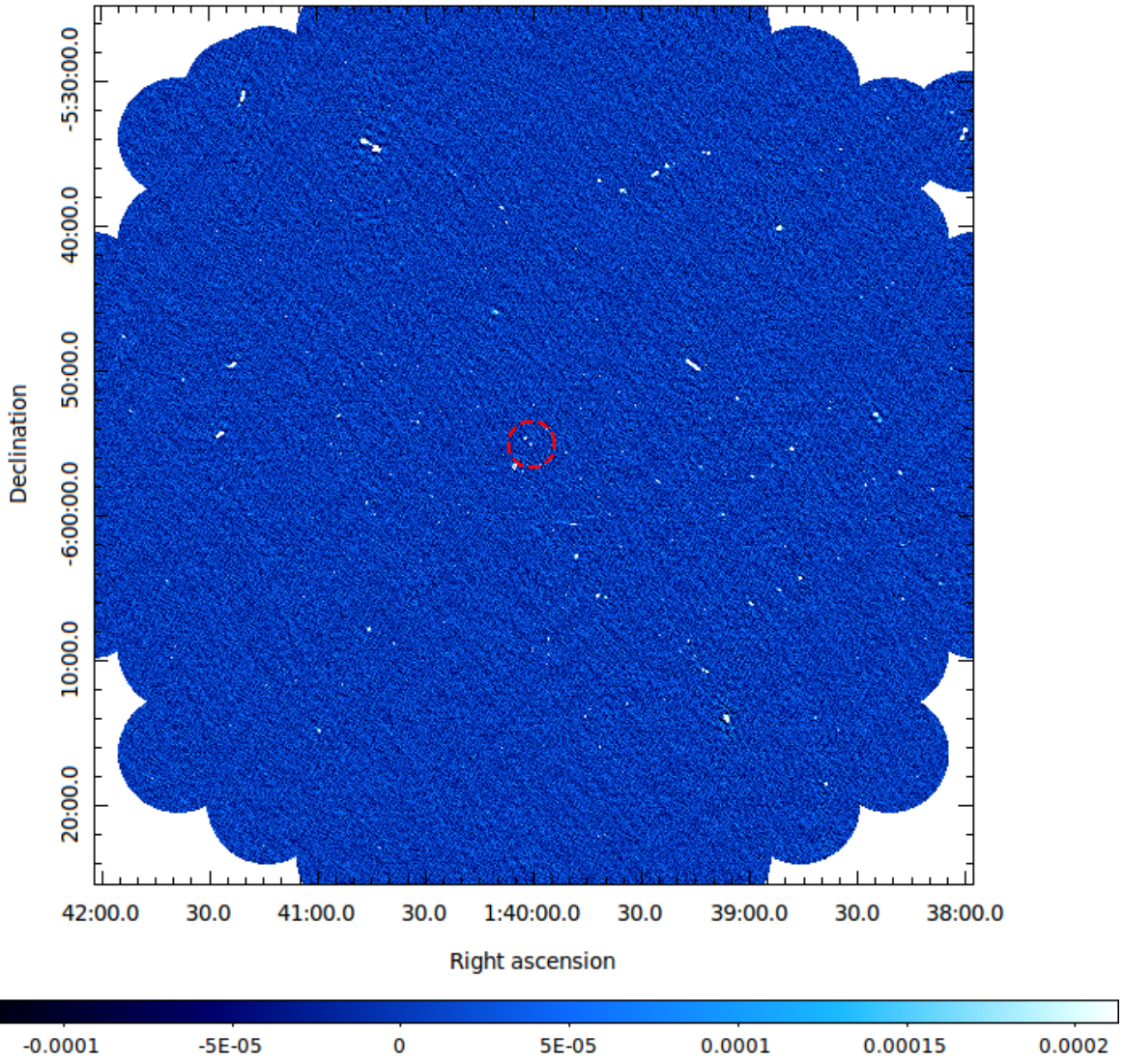

Figure A.12: The full field of view of the high-resolution image of ACT-CL J0140.0-0555. The red circle indicates the SZ cluster scale, $\theta_{500} = 3.3'$ centered at the SZ peak. The rms noise level of the full image is 37.95 μJy beam^{-1}. The colour units for this image are in Jy beam^{-1}.

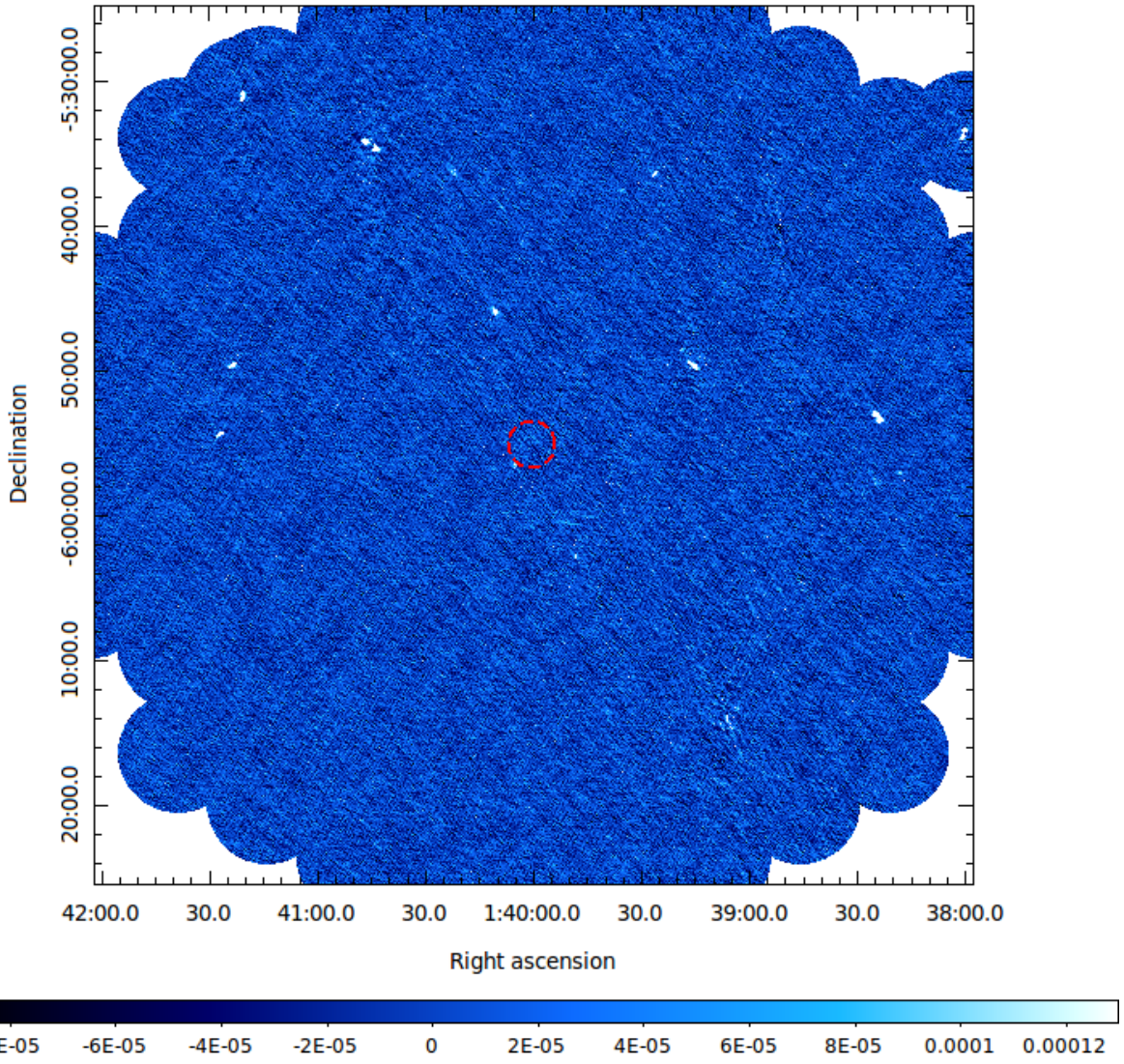

Figure A.13: The full-resolution image of the point source subtracted ACT-CL J0140.0-0555 field. The red circle indicates the SZ cluster scale, $\theta_{500} = 3.3'$ centered at the SZ peak. The rms noise level of the full image is 30.59 μJy beam^{-1}. The colour units for this image are in Jy beam^{-1}.

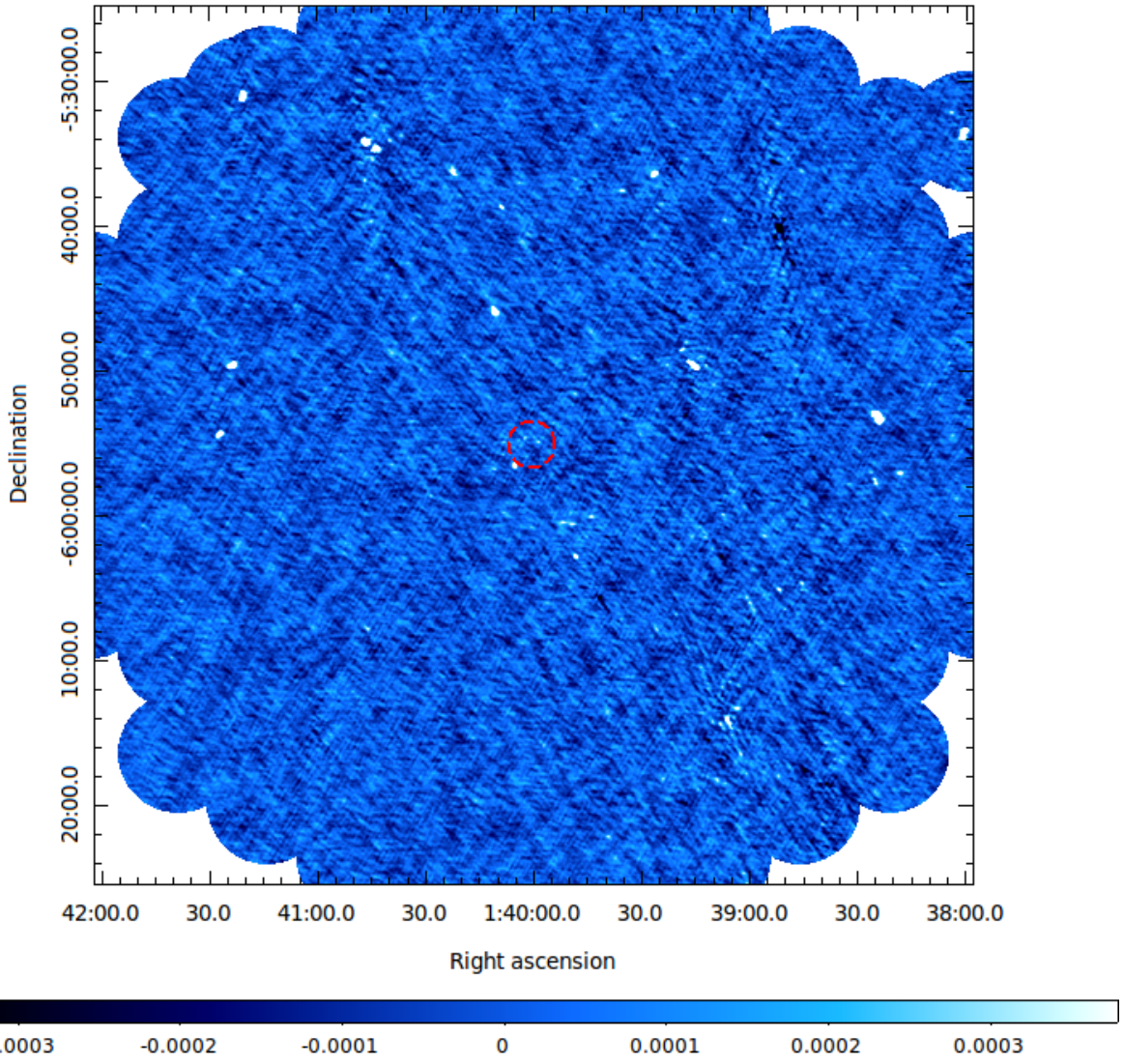

Figure A.14: The low-resolution image of the point source subtracted ACT-CL J0140.0-0555 field. A uv-taper at 10 kλ was applied. The red circle indicates the SZ cluster scale, $\theta_{500} = 3.3'$ centered at the SZ peak. The rms noise level of the full image is 69.84 μJy beam^{-1}. The colour units for this image are in Jy beam^{-1}.

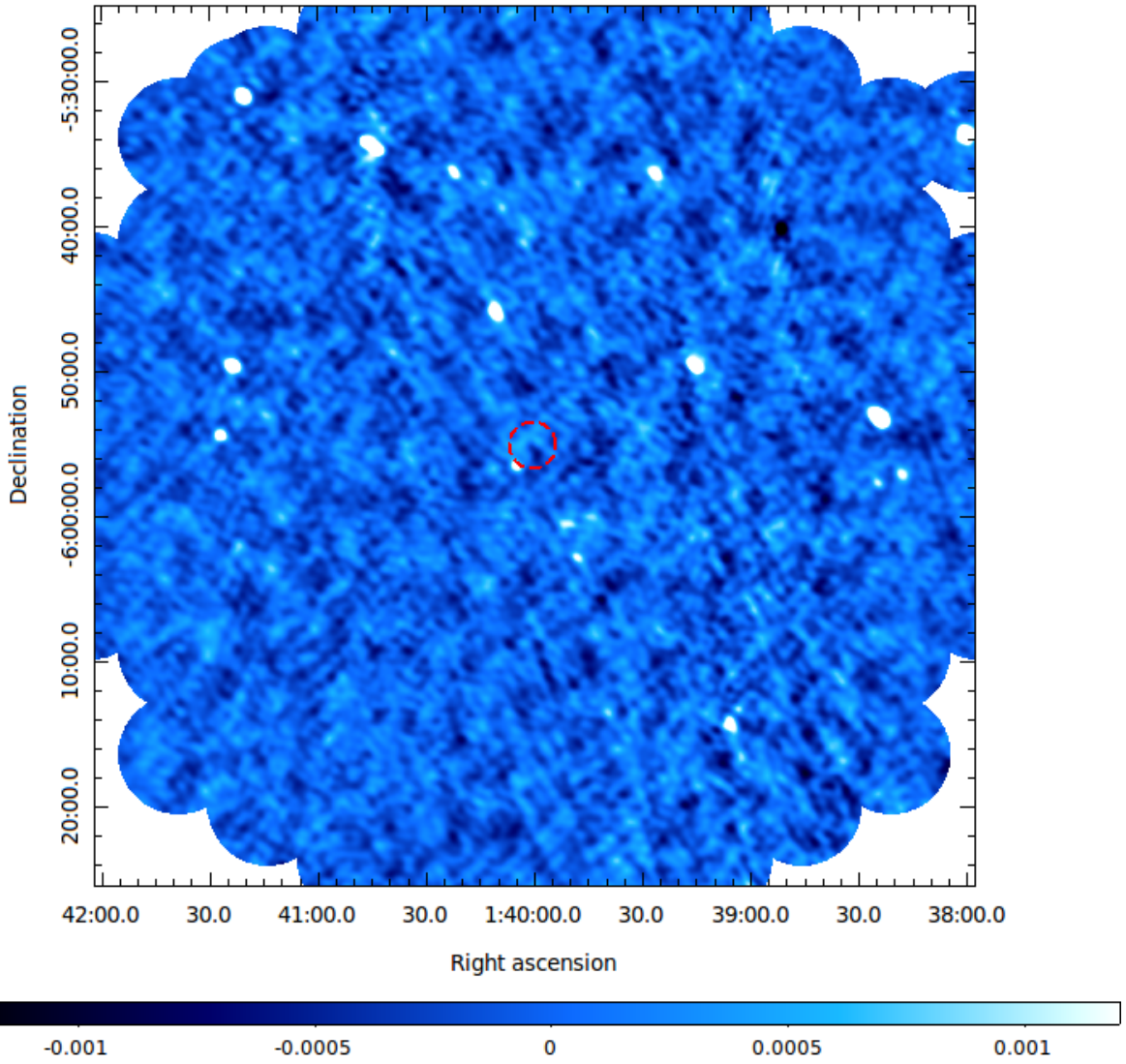

Figure A.15: The low-resolution image of the point source subtracted ACT-CL J0140.0-0555 field. The following uv restrictions were applied: uv-range < 5 kλ and uv-taper at 4 kλ. The red circle indicates the SZ cluster scale, $\theta_{500} = 3.3'$ centered at the SZ peak. The rms noise level of the full image is 238 μJy beam^{-1}. The colour units for this image are in Jy beam^{-1}.

A.4 ACT-CL J0137.4-0827

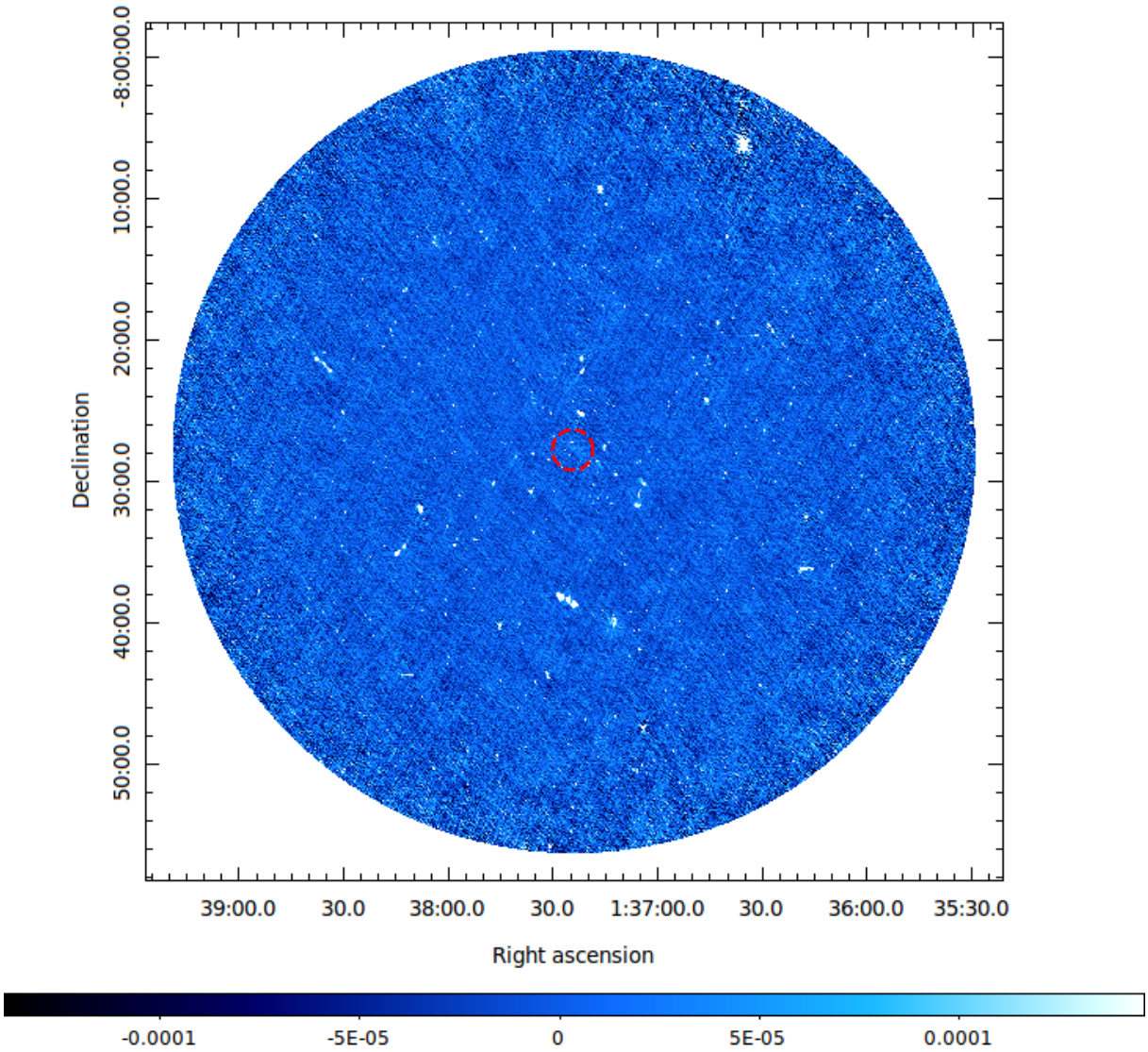

Figure A.16: The full-resolution image of the primary beam corrected ACT-CL J00137.4-0827. The red circle indicates the SZ cluster scale, $\theta_{500} = 2.9'$ centered at the SZ peak. The rms noise level of the full image is 21.83 μJy beam^{-1}. The colour units for this image are in Jy beam^{-1}.

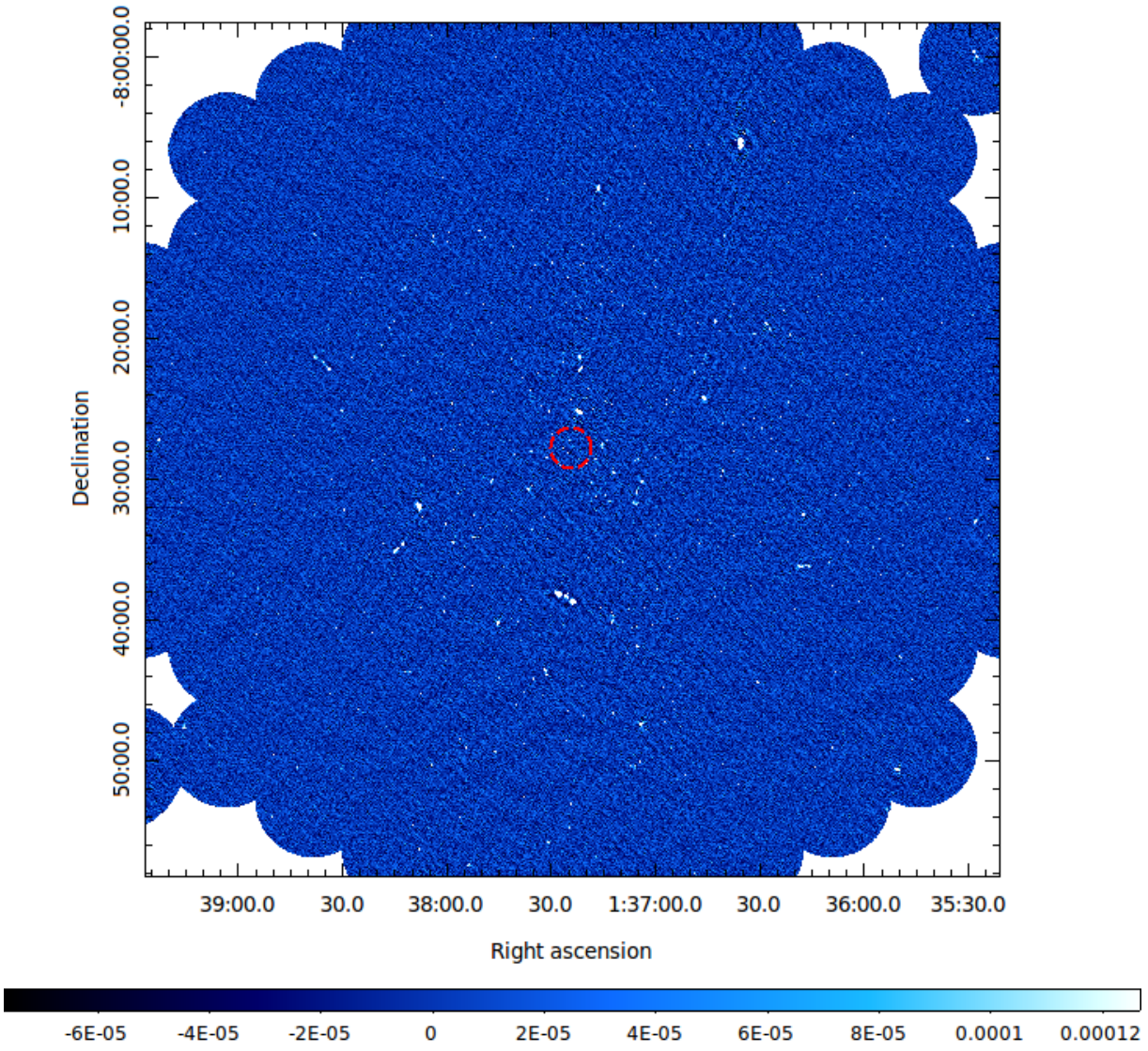

Figure A.17: The full field of view of the high-resolution image of ACT-CL J0137.4-0827. The red circle indicates the SZ cluster scale, $\theta_{500} = 2.9'$ centered at the SZ peak. The rms noise level of the full image is 24.5 μJy beam^{-1}. The colour units for this image are in Jy beam^{-1}.

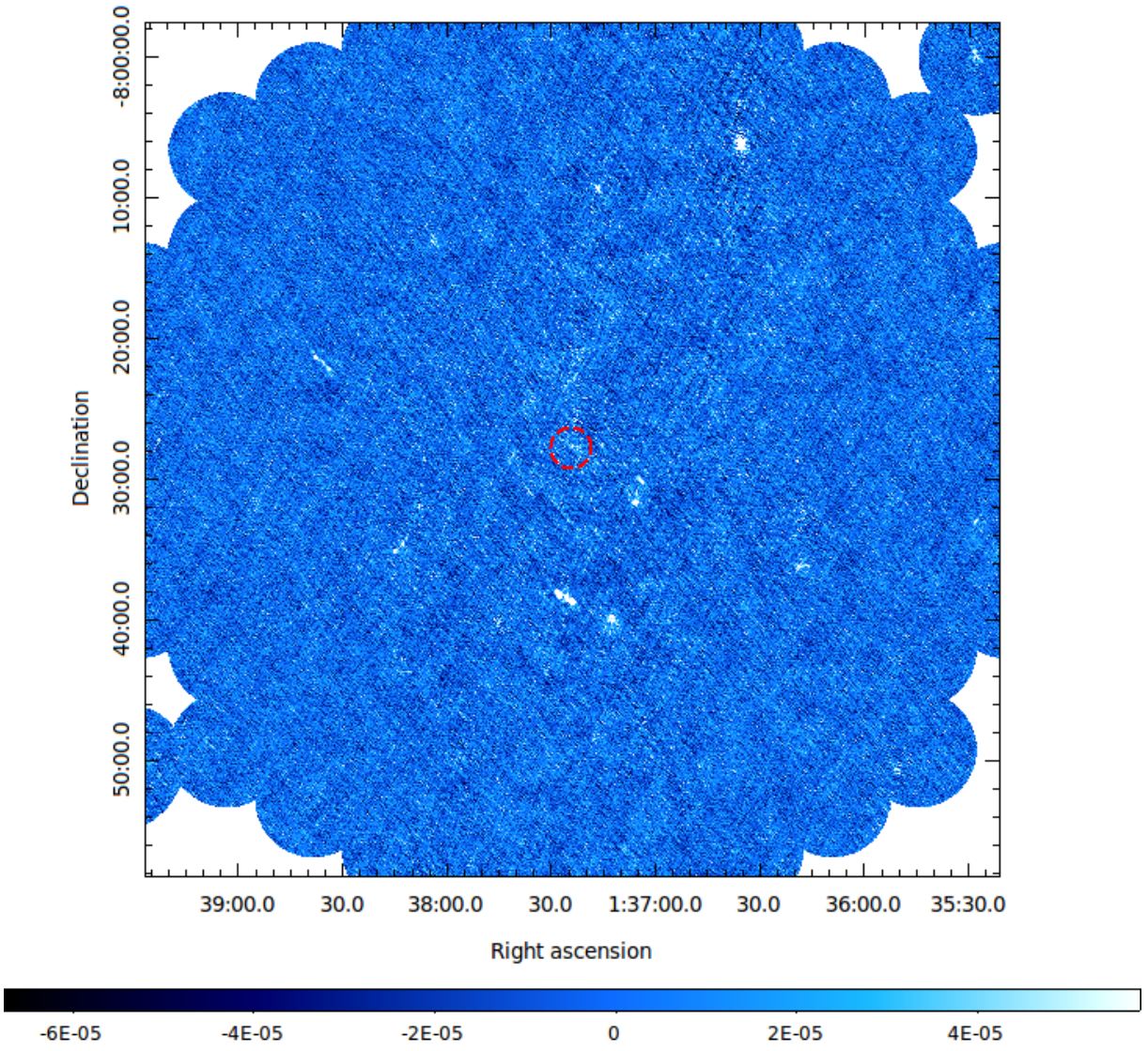

Figure A.18: The full-resolution image of the point source subtracted ACT-CL J0137.4-0827 field. The red circle indicates the SZ cluster scale, $\theta_{500} = 2.9'$ centered at the SZ peak. The rms noise level of the full image is 19.38 μJy beam^{-1}. The colour units for this image are in Jy beam^{-1}.

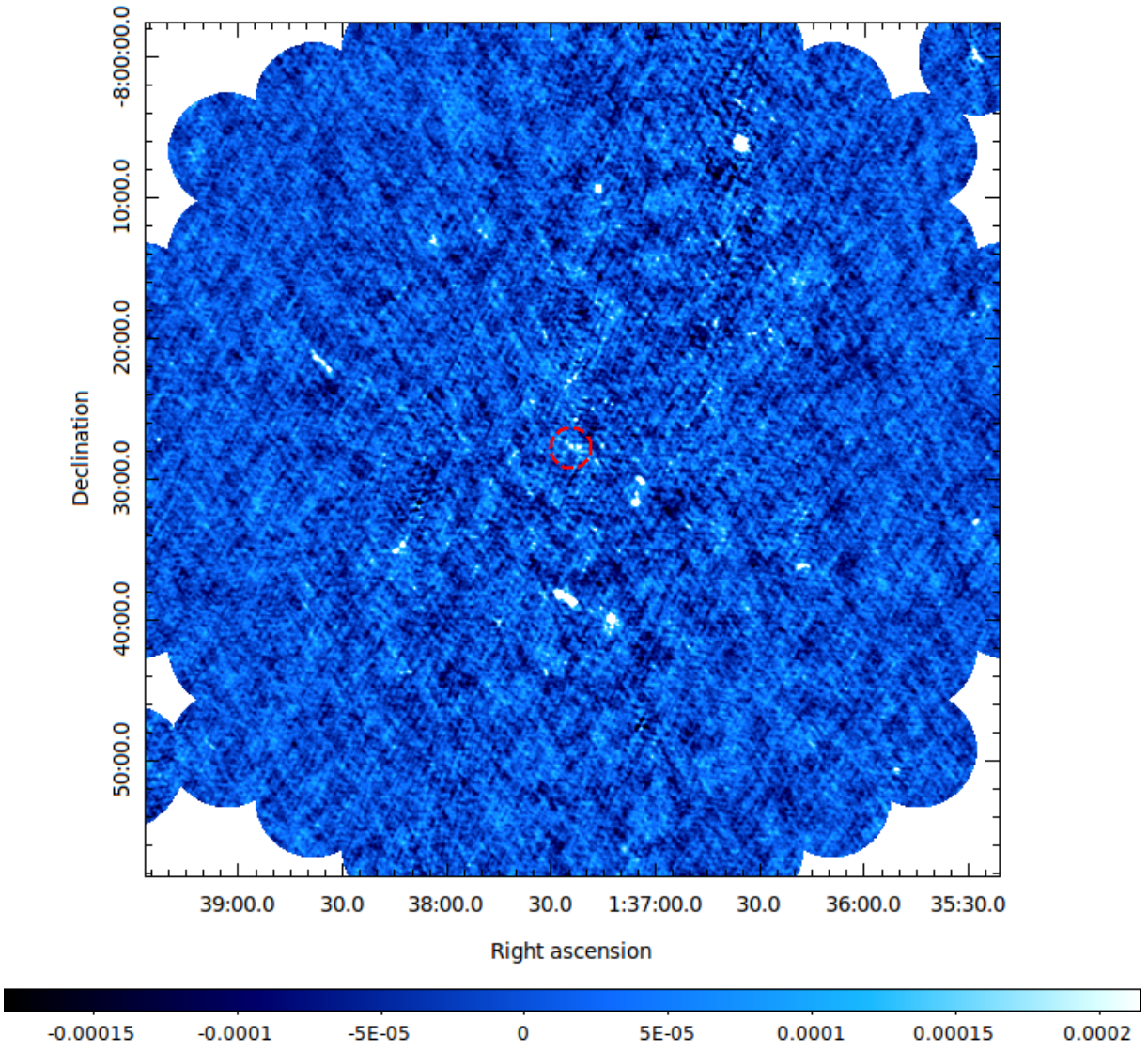

Figure A.19: The low-resolution image of the point source subtracted ACT-CL J0137.4-0827 field. A uv-taper at 10 kλ was applied. The red circle indicates the SZ cluster scale, $\theta_{500} = 2.9'$ centered at the SZ peak. The rms noise level of the full image is 40.0 μJy beam^{-1}. The colour units for this image are in Jy beam^{-1}.

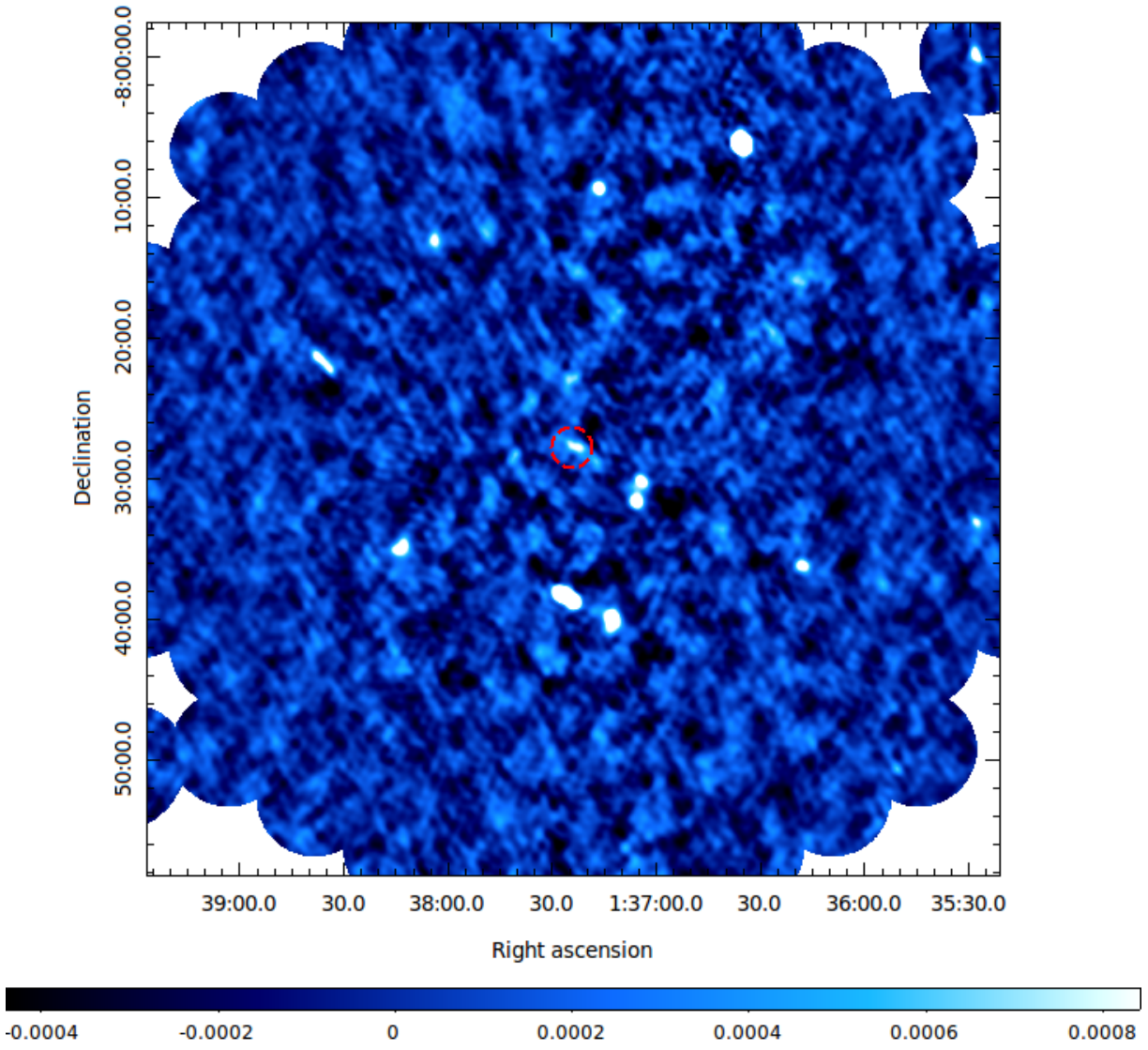

Figure A.20: The low-resolution image of the point source subtracted ACT-CL J0137.4-0827 field. The following uv restrictions were applied: uv-range < 5 kλ and uv-taper at 4 kλ. The red circle indicates the SZ cluster scale, $\theta_{500} = 2.9'$ centered at the SZ peak. The rms noise level of the full image is 120 μJy beam^{-1}. The colour units for this image are in Jy beam^{-1}.

APPENDIX B

Derivations

The following is a derivation of Let us label ϵ as a small deviation from the desired reflector surface. This can be expressed as a Gaussian random variable with a probability distribution given by

$$p(\epsilon) = \frac{1}{\sqrt{2\pi\sigma}} e^{[\frac{-\epsilon^2}{2\sigma^2}]}, \tag{B.1}$$

where $< \epsilon >= 0$ and $< \epsilon^2 >= \sigma^2$. From the probability distribution function we can derive the following relation

$$\langle e^{j\epsilon} \rangle = \langle \cos\epsilon \rangle + \langle j \sin\epsilon \rangle = \langle \cos\epsilon \rangle = \int_{-\infty}^{\infty} \cos(\epsilon) p(\epsilon) d\epsilon = e^{\frac{-\sigma 2}{2}}. \tag{B.2}$$

The small deviation causes a phase shift of approximately $\frac{4\pi\epsilon}{\lambda}$. Let us assume that the parabolic reflector surfaces are made up of N independent sections. The total collecting area is

$$A = A_0 \langle | \frac{1}{N} \sum_i e^{j\phi_i} |^2 \rangle = \frac{A_0}{N^2} \sum_{i,k} \langle e^{j(\phi_i - \phi_k)} \rangle = A_0 \langle e^{j\phi_i} \rangle^2. \tag{B.3}$$

If N is large enough the collecting area reduces to

$$A = A_0 e^{-(\frac{4\pi\epsilon}{\lambda})^2}. \tag{B.4}$$

The aperture efficiency is defined as $\frac{A}{A_0}$. Future generation telescopes aim to maximize aperture efficiency and effective collecting area.

Bibliography

Abazajian, K. N., Adelman-McCarthy, J. K., Agüeros, M. A., Allam, S. S., Allende Prieto, C., An, D., Anderson, K. S. J., Anderson, S. F., Annis, J., Bahcall, N. A., and et al. (2009). The Seventh Data Release of the Sloan Digital Sky Survey. *Astrophys. J. Supp.*, 182:543–558.

Abbott, T., Abdalla, F. B., Allam, S., Amara, A., Annis, J., Armstrong, R., Bacon, D., Banerji, M., Bauer, A. H., Baxter, E., Becker, M. R., Benoit-Lévy, A., Bernstein, R. A., Bernstein, G. M., Bertin, E., Blazek, J., Bonnett, C., Bridle, S. L., Brooks, D., Bruderer, C., Buckley-Geer, E., Burke, D. L., Busha, M. T., Capozzi, D., Carnero Rosell, A., Carrasco Kind, M., Carretero, J., Castander, F. J., Chang, C., Clampitt, J., Crocce, M., Cunha, C. E., D'Andrea, C. B., da Costa, L. N., Das, R., DePoy, D. L., Desai, S., Diehl, H. T., Dietrich, J. P., Dodelson, S., Doel, P., Drlica-Wagner, A., Efstathiou, G., Eifler, T. F., Erickson, B., Estrada, J., Evrard, A. E., Fausti Neto, A., Fernandez, E., Finley, D. A., Flaugher, B., Fosalba, P., Friedrich, O., Frieman, J., Gangkofner, C., Garcia-Bellido, J., Gaztanaga, E., Gerdes, D. W., Gruen, D., Gruendl, R. A., Gutierrez, G., Hartley, W., Hirsch, M., Honscheid, K., Huff, E. M., Jain, B., James, D. J., Jarvis, M., Kacprzak, T., Kent, S., Kirk, D., Krause, E., Kravtsov, A., Kuehn, K., Kuropatkin, N., Kwan, J., Lahav, O., Leistedt, B., Li, T. S., Lima, M., Lin, H., MacCrann, N., March, M., Marshall, J. L., Martini, P., McMahon, R. G., Melchior, P., Miller, C. J., Miquel, R., Mohr, J. J., Neilsen, E., Nichol, R. C., Nicola, A., Nord, B., Ogando, R., Palmese, A., Peiris, H. V., Plazas, A. A., Refregier, A., Roe, N., Romer, A. K., Roodman, A., Rowe, B., Rykoff, E. S., Sabiu, C., Sadeh, I., Sako, M., Samuroff, S., Sanchez, E., Sánchez, C.,

Seo, H., Sevilla-Noarbe, I., Sheldon, E., Smith, R. C., Soares-Santos, M., Sobreira, F., Suchyta, E., Swanson, M. E. C., Tarle, G., Thaler, J., Thomas, D., Troxel, M. A., Vikram, V., Walker, A. R., Wechsler, R. H., Weller, J., Zhang, Y., Zuntz, J., and Dark Energy Survey Collaboration (2016). Cosmology from cosmic shear with Dark Energy Survey Science Verification data. *Physical Review D.*, 94(2):022001.

Abell, G. O. (1958). The Distribution of Rich Clusters of Galaxies. *Astrophys. J. Supp.*, 3:211.

Ackermann, M., Ajello, M., Albert, A., Allafort, A., Atwood, W. B., Baldini, L., Ballet, J., Barbiellini, G., Bastieri, D., Bechtol, K., Bellazzini, R., Bloom, E. D., Bonamente, E., Bottacini, E., Brandt, T. J., Bregeon, J., Brigida, M., Bruel, P., Buehler, R., Buson, S., Caliandro, G. A., Cameron, R. A., Caraveo, P. A., Cavazzuti, E., Chaves, R. C. G., Chiang, J., Chiaro, G., Ciprini, S., Claus, R., Cohen-Tanugi, J., Conrad, J., D'Ammando, F., de Angelis, A., de Palma, F., Dermer, C. D., Digel, S. W., Drell, P. S., Drlica-Wagner, A., Favuzzi, C., Franckowiak, A., Funk, S., Fusco, P., Gargano, F., Gasparrini, D., Germani, S., Giglietto, N., Giordano, F., Giroletti, M., Godfrey, G., Gomez-Vargas, G. A., Grenier, I. A., Guiriec, S., Gustafsson, M., Hadasch, D., Hayashida, M., Hewitt, J., Hughes, R. E., Jeltema, T. E., Jóhannesson, G., Johnson, A. S., Kamae, T., Kataoka, J., Knödlseder, J., Kuss, M., Lande, J., Larsson, S., Latronico, L., Llena Garde, M., Longo, F., Loparco, F., Lovellette, M. N., Lubrano, P., Mayer, M., Mazziotta, M. N., McEnery, J. E., Michelson, P. F., Mitthumsiri, W., Mizuno, T., Monzani, M. E., Morselli, A., Moskalenko, I. V., Murgia, S., Nemmen, R., Nuss, E., Ohsugi, T., Orienti, M., Orlando, E., Ormes, J. F., Perkins, J. S., Pesce-Rollins, M., Piron, F., Pivato, G., Rainò, S., Rando, R., Razzano, M., Razzaque, S., Reimer, A., Reimer, O., Ruan, J., Sánchez-Conde, M., Schulz, A., Sgrò, C., Siskind, E. J., Spandre, G., Spinelli, P., Storm, E., Strong, A. W., Suson, D. J., Takahashi, H., Thayer, J. G., Thayer, J. B., Thompson, D. J., Tibaldo, L., Tinivella, M., Torres, D. F., Troja, E., Uchiyama, Y., Usher, T. L., Vandenbroucke, J., Vianello, G., Vitale, V., Winer, B. L., Wood, K. S., Zimmer, S., Fermi-LAT Collaboration, Pinzke, A., and Pfrommer, C. (2014). Search for Cosmic-Ray-induced Gamma-Ray Emission in Galaxy Clusters. *Astrophys. J.*, 787:18.

Acosta-Pulido, J. A., Agudo, I., Alberdi, A., Alcolea, J., Alfaro, E. J., Alonso-Herrero, A., Anglada, G., Arnalte-Mur, P., Ascasibar, Y., Ascaso, B., Azulay, R., Bachiller, R., Baez-Rubio, A., Battaner, E., Blasco, J., Brook, C. B., Bujarrabal, V., Busquet, G.,

Caballero-Garcia, M. D., Carrasco-Gonzalez, C., Casares, J., Castro-Tirado, A. J., Colina, L., Colomer, F., de Gregorio-Monsalvo, I., del Olmo, A., Desmurs, J.-F., Diego, J. M., Dominguez-Tenreiro, R., Estalella, R., Fernandez-Soto, A., Florido, E., Font, J., Font, J. A., Fuente, A., Garcia-Benito, R., Garcia-Burillo, S., Garcia-Lorenzo, B., Gil de Paz, A., Girart, J. M., Goicoechea, J. R., Gomez, J. F., Gonzalez-Garcia, M., Gonzalez-Martin, O., Gonzalez-Serrano, J. I., Gorgas, J., Gorosabel, J., Guijarro, A., Guirado, J. C., Hernandez-Garcia, L., Hernandez-Monteagudo, C., Herranz, D., Herrero-Illana, R., Hu, Y.-D., Huelamo, N., Huertas-Company, M., Iglesias-Paramo, J., Jeong, S., Jimenez-Serra, I., Knapen, J. H., Lineros, R. A., Lisenfeld, U., Marcaide, J. M., Marquez, I., Marti, J., Marti, J. M., Marti-Vidal, I., Martinez-Gonzalez, E., Martin-Pintado, J., Masegosa, J., Mayen-Gijon, J. M., Mezcua, M., Migliari, S., Mimica, P., Moldon, J., Morata, O., Negueruela, I., Oates, S. R., Osorio, M., Palau, A., Paredes, J. M., Perea, J., Perez-Gonzalez, P. G., Perez-Montero, E., Perez-Torres, M. A., Perucho, M., Planelles, S., Pons, J. A., Prieto, A., Quilis, V., Ramirez-Moreta, P., Ramos Almeida, C., Rea, N., Ribo, M., Rioja, M. J., Rodriguez Espinosa, J. M., Ros, E., Rubiño-Martin, J. A., Ruiz-Granados, B., Sabater, J., Sanchez, S., Sanchez-Contreras, C., Sanchez-Monge, A., Sanchez-Ramirez, R., Sintes, A. M. andSolanes, J. M., Sopuerta, C. F., Tafalla, M., Tello, J. C., Tercero, B., Toribio, M. C., Torrelles, J. M., Torres, M. A. P., Usero, A., Verdes-Montenegro, L., Vidal-Garcia, A., Vielva, P., Vilchez, J., and Zhang, B.-B. (2015). The Spanish Square Kilometre Array White Book. *ArXiv e-prints 1506.03474*.

Ahn, C. P., Alexandroff, R., Allende Prieto, C., Anders, F., Anderson, S. F., Anderton, T., Andrews, B. H., Aubourg, É., Bailey, S., Bastien, F. A., and et al. (2014). The Tenth Data Release of the Sloan Digital Sky Survey: First Spectroscopic Data from the SDSS-III Apache Point Observatory Galactic Evolution Experiment. *Astrophys. J. Supp.*, 211:17.

Alam, S., Ata, M., Bailey, S., Beutler, F., Bizyaev, D., Blazek, J. A., Bolton, A. S., Brownstein, J. R., Burden, A., Chuang, C.-H., Comparat, J., Cuesta, A. J., Dawson, K. S., Eisenstein, D. J., Escoffier, S., Gil-Marín, H., Grieb, J. N., Hand, N., Ho, S., Kinemuchi, K., Kirkby, D., Kitaura, F., Malanushenko, E., Malanushenko, V., Maraston, C., McBride, C. K., Nichol, R. C., Olmstead, M. D., Oravetz, D., Padmanabhan, N., Palanque-Delabrouille, N., Pan, K., Pellejero-Ibanez, M., Percival, W. J., Petitjean, P., Prada, F., Price-Whelan, A. M., Reid, B. A., Rodríguez-Torres, S. A., Roe, N. A., Ross, A. J., Ross, N. P., Rossi, G., Rubiño-Martín, J. A., Sánchez, A. G., Saito, S., Salazar-

Albornoz, S., Samushia, L., Satpathy, S., Scóccola, C. G., Schlegel, D. J., Schneider, D. P., Seo, H.-J., Simmons, A., Slosar, A., Strauss, M. A., Swanson, M. E. C., Thomas, D., Tinker, J. L., Tojeiro, R., Vargas Magaña, M., Vazquez, J. A., Verde, L., Wake, D. A., Wang, Y., Weinberg, D. H., White, M., Wood-Vasey, W. M., Yèche, C., Zehavi, I., Zhai, Z., and Zhao, G.-B. (2016). The clustering of galaxies in the completed SDSS-III Baryon Oscillation Spectroscopic Survey: cosmological analysis of the DR12 galaxy sample. *ArXiv e-prints 1607.03155*.

Albrecht, A., Amendola, L., Bernstein, G., Clowe, D., Eisenstein, D., Guzzo, L., Hirata, C., Huterer, D., Kirshner, R., Kolb, E., and Nichol, R. (2009). Findings of the Joint Dark Energy Mission Figure of Merit Science Working Group. *ArXiv e-prints 0901.0721*.

Allen, S. W., Schmidt, R. W., Ebeling, H., Fabian, A. C., and van Speybroeck, L. (2004). Constraints on dark energy from Chandra observations of the largest relaxed galaxy clusters. *Mon. Not. R. Astron. Soc.*, 353:457–467.

Anderson, L., Aubourg, E., Bailey, S., Beutler, F., Bolton, A. S., Brinkmann, J., Brownstein, J. R., Chuang, C.-H., Cuesta, A. J., Dawson, K. S., Eisenstein, D. J., Ho, S., Honscheid, K., Kazin, E. A., Kirkby, D., Manera, M., McBride, C. K., Mena, O., Nichol, R. C., Olmstead, M. D., Padmanabhan, N., Palanque-Delabrouille, N., Percival, W. J., Prada, F., Ross, A. J., Ross, N. P., Sánchez, A. G., Samushia, L., Schlegel, D. J., Schneider, D. P., Seo, H.-J., Strauss, M. A., Thomas, D., Tinker, J. L., Tojeiro, R., Verde, L., Wake, D., Weinberg, D. H., Xu, X., and Yeche, C. (2014). The clustering of galaxies in the SDSS-III Baryon Oscillation Spectroscopic Survey: measuring D_A and H at z = 0.57 from the baryon acoustic peak in the Data Release 9 spectroscopic Galaxy sample. *Mon. Not. R. Astron. Soc.*, 439:83–101.

Ascaso, B., Mei, S., and Benítez, N. (2015). Apples to apples A^2 - I. Realistic galaxy simulated catalogues and photometric redshift predictions for next-generation surveys. *Mon. Not. R. Astron. Soc.*, 453:2515–2532.

Bagchi, J., Enßlin, T. A., Miniati, F., Stalin, C. S., Singh, M., Raychaudhury, S., and Humeshkar, N. B. (2002). Evidence for shock acceleration and intergalactic magnetic fields in a large-scale filament of galaxies ZwCl 2341.1+0000. *New Astron.*, 7:249–277.

Bahcall, N. A. (1977). Clusters of galaxies. *Annu. Rev. Astron. Astrophys.*, 15:505–540.

Barrena, R., Boschin, W., Girardi, M., and Spolaor, M. (2007). Internal dynamics of the radio halo cluster Abell 773: a multiwavelength analysis. *Astron. Astrophys.*, 467:37–48.

Basu, K. (2012). A Sunyaev-Zel'dovich take on cluster radio haloes - I. Global scaling and bi-modality using Planck data. *Mon. Not. R. Astron. Soc.*, 421:L112–L116.

Battistelli, E. S., Burigana, C., de Bernardis, P., Kirillov, A. A., Neto, G. B. L., Masi, S., Norgaard-Nielsen, H. U., Ostermann, P., Roman, M., Rosati, P., and Rossetti, M. (2016). Galaxy clusters as probes for cosmology and dark matter. *International Journal of Modern Physics D*, 25:1630023.

Bautz, L. P. and Morgan, W. W. (1970). On the Classification of the Forms of Clusters of Galaxies. *Astrophys. J. Lett.*, 162:L149.

Becker, R. H., White, R. L., and Helfand, D. J. (1994). The VLA's FIRST Survey. In Crabtree, D. R., Hanisch, R. J., and Barnes, J., editors, *Astronomical Data Analysis Software and Systems III*, volume 61 of *Astronomical Society of the Pacific Conference Series*, page 165.

Bennett, C. L., Boggess, N. W., Cheng, E. S., Hauser, M. G., Kelsall, T., Mather, J. C., Moseley, Jr., S. H., Murdock, T. L., Shafer, R. A., and Silverberg, R. F. (1993). Scientific results from COBE. *Advances in Space Research*, 13.

Bennett, C. L., Larson, D., Weiland, J. L., Jarosik, N., Hinshaw, G., Odegard, N., Smith, K. M., Hill, R. S., Gold, B., Halpern, M., Komatsu, E., Nolta, M. R., Page, L., Spergel, D. N., Wollack, E., Dunkley, J., Kogut, A., Limon, M., Meyer, S. S., Tucker, G. S., and Wright, E. L. (2013). Nine-year Wilkinson Microwave Anisotropy Probe (WMAP) Observations: Final Maps and Results. *Astrophys. J. Supp.*, 208:20.

Beresnyak, A., Xu, H., Li, H., and Schlickeiser, R. (2013). Magnetohydrodynamic Turbulence and Cosmic-Ray Reacceleration in Galaxy Clusters. *Astrophys. J.*, 771:131.

Berger, J. P. and Segransan, D. (2007). An introduction to visibility modeling. *New Astron. Rev.*, 51:576–582.

Berrington, R. C. and Dermer, C. D. (2002). Nonthermal Particles Accelerated by Cluster Merger Shocks: Radiation and Pressure. In *American Astronomical Society Meeting Abstracts*, volume 34 of *Bulletin of the American Astronomical Society*, page 1207.

Betoule, M., Kessler, R., Guy, J., Mosher, J., Hardin, D., Biswas, R., Astier, P., El-Hage, P., Konig, M., Kuhlmann, S., Marriner, J., Pain, R., Regnault, N., Balland, C., Bassett, B. A., Brown, P. J., Campbell, H., Carlberg, R. G., Cellier-Holzem, F., Cinabro, D., Conley, A., D'Andrea, C. B., DePoy, D. L., Doi, M., Ellis, R. S., Fabbro, S., Filippenko, A. V., Foley, R. J., Frieman, J. A., Fouchez, D., Galbany, L., Goobar, A., Gupta, R. R., Hill, G. J., Hlozek, R., Hogan, C. J., Hook, I. M., Howell, D. A., Jha, S. W., Le Guillou, L., Leloudas, G., Lidman, C., Marshall, J. L., Möller, A., Mourão, A. M., Neveu, J., Nichol, R., Olmstead, M. D., Palanque-Delabrouille, N., Perlmutter, S., Prieto, J. L., Pritchet, C. J., Richmond, M., Riess, A. G., Ruhlmann-Kleider, V., Sako, M., Schahmaneche, K., Schneider, D. P., Smith, M., Sollerman, J., Sullivan, M., Walton, N. A., and Wheeler, C. J. (2014). Improved cosmological constraints from a joint analysis of the SDSS-II and SNLS supernova samples. *Astron. Astrophys.*, 568:A22.

Beutler, F. and BOSS Collaboration (2015). The Baryon Oscillation Spectroscopic Survey (BOSS): Constraining dark energy with Baryon Acoustic Oscillations. In *APS April Meeting Abstracts*.

Bhat, N. D. R., Chengalur, J. N., Cox, P. J., Gupta, Y., Prasad, J., Roy, J., Bailes, M., Burke-Spolaor, S., Kudale, S. S., and van Straten, W. (2013). Detection of Fast Transients with Radio Interferometric Arrays. *Astrophys. J. Supp.*, 206:2.

Biffi, V., Borgani, S., Murante, G., Rasia, E., Planelles, S., Granato, G. L., Ragone-Figueroa, C., Beck, A. M., Gaspari, M., and Dolag, K. (2016). On the Nature of Hydrostatic Equilibrium in Galaxy Clusters. *Astrophys. J.*, 827:112.

Bolton, J. G., Stanley, G. J., and Slee, O. B. (1949). Positions of Three Discrete Sources of Galactic Radio-Frequency Radiation. *Nature.*, 164:101–102.

Bonafede, A., Intema, H., Brüggen, M., Vazza, F., Basu, K., Sommer, M., Ebeling, H., de Gasperin, F., Röttgering, H. J. A., van Weeren, R. J., and Cassano, R. (2015). Radio haloes in Sunyaev-Zel'dovich-selected clusters of galaxies: the making of a halo? *Mon. Not. R. Astron. Soc.*, 454:3391–3402.

Bonafede, A., Intema, H. T., Brüggen, M., Girardi, M., Nonino, M., Kantharia, N., van Weeren, R. J., and Röttgering, H. J. A. (2014). Evidence for Particle Re-acceleration in the Radio Relic in the Galaxy Cluster PLCKG287.0+32.9. *Astrophys. J.*, 785:1.

Boschin, W., Girardi, M., Barrena, R., and Nonino, M. (2012). Abell 1758N from an optical point of view: new insights on a merging cluster with diffuse radio emission. *Astron. Astrophys.*, 540:A43.

Botteon, A., Gastaldello, F., Brunetti, G., and Dallacasa, D. (2016). A shock at the radio relic position in Abell 115. *Mon. Not. R. Astron. Soc.*, 460:L84–L88.

Bravi, L., Gitti, M., and Brunetti, G. (2015). On the connection between radio mini-halos and gas heating in cool-core clusters. In *The Many Facets of Extragalactic Radio Surveys: Towards New Scientific Challenges*, page 47.

Brederode, L. R., van den Heever, L., Esterhuyse, W., and Jonas, J. L. (2016). MeerKAT: a project status report. In *Society of Photo-Optical Instrumentation Engineers (SPIE) Conference Series*, volume 9906 of , page 990625.

Bridger, A., Clarke, D. A., Chavan, A. M., Schwarz, J., Schilling, M., Testi, L., and Sommer, H. (2004). Proposal and observing preparation for ALMA. In Quinn, P. J. and Bridger, A., editors, *Optimizing Scientific Return for Astronomy through Information Technologies*, volume 5493 of , pages 392–400.

Briel, U. G., Henry, J. P., and Boehringer, H. (1992). Observation of the Coma cluster of galaxies with ROSAT during the all-sky survey. *Astron. Astrophys.*, 259:L31–L34.

Briggs, D. S. (1995). High Fidelity Interferometric Imaging: Robust Weighting and NNLS Deconvolution. In *American Astronomical Society Meeting Abstracts*, volume 27 of *Bulletin of the American Astronomical Society*, page 1444.

Brunetti, G. (2004a). Non-thermal phenomena in galaxy clusters. In Diaferio, A., editor, *IAU Colloq. 195: Outskirts of Galaxy Clusters: Intense Life in the Suburbs*, pages 148–154.

Brunetti, G. (2004b). Particle Acceleration and Non-Thermal Emission from Galaxy Clusters. *Journal of Korean Astronomical Society*, 37:493–500.

Brunetti, G. (2011a). Cosmic rays and diffuse non-thermal emission in galaxy clusters: an introduction. *Mem. Societa Astronomica Italiana*, 82:515.

Brunetti, G. (2011b). Giant Radio Halos in Galaxy Clusters as Probes of Particle Acceleration in Turbulent Regions. *Journal of Astrophysics and Astronomy*, 32:437–445.

Brunetti, G. and Blasi, P. (2005). Alfvénic reacceleration of relativistic particles in galaxy clusters in the presence of secondary electrons and positrons. *Mon. Not. R. Astron. Soc.*, 363:1173–1187.

Brunetti, G., Blasi, P., Reimer, O., Rudnick, L., Bonafede, A., and Brown, S. (2012). Probing the origin of giant radio haloes through radio and γ-ray data: the case of the Coma cluster. *Mon. Not. R. Astron. Soc.*, 426:956–968.

Brunetti, G. and Cassano, R. (2010). Radio Halos and the importance of future observations at low frequency. In *ISKAF2010 Science Meeting*, page 8.

Brunetti, G., Giacintucci, S., Cassano, R., Lane, W., Dallacasa, D., Venturi, T., Kassim, N. E., Setti, G., Cotton, W. D., and Markevitch, M. (2008). A low-frequency radio halo associated with a cluster of galaxies. *Nature.*, 455:944–947.

Brunetti, G. and Jones, T. W. (2014). Cosmic Rays in Galaxy Clusters and Their Nonthermal Emission. *International Journal of Modern Physics D*, 23:30007.

Brunetti, G. and Lazarian, A. (2011). Acceleration of primary and secondary particles in galaxy clusters by compressible MHD turbulence: from radio haloes to gamma-rays. *Mon. Not. R. Astron. Soc.*, 410:127–142.

Buote, D. A. (2001). On the Origin of Radio Halos in Galaxy Clusters. *Astrophys. J. Lett.*, 553:L15–L18.

Buzzi, L., Cozzi, E., Kowalski, R. A., Boattini, A., Christensen, E. J., Gibbs, A. R., Grauer, A. D., Hill, R. E., Johnson, J. A., Larson, S. M., McNaught, R. H., Holmes, R., Devore, H., Foglia, S., Vorobjov, T., Linder, T., Losse, F., and Birtwhistle, P. (2013). 2013 DS9. *Minor Planet Electronic Circulars*, 46.

Camera, S., Harrison, I., Bonaldi, A., and Brown, M. L. (2016). SKA Weak Lensing III: Added Value of Multi-Wavelength Synergies for the Mitigation of Systematics. *ArXiv e-prints 1606.03451*.

Carozzi, T. D. and Woan, G. (2009). A generalized measurement equation and van Cittert-Zernike theorem for wide-field radio astronomical interferometry. *Mon. Not. R. Astron. Soc.*, 395:1558–1568.

Cassano, R. (2010). The radio-X-ray luminosity correlation of radio halos at low radio frequency. Application of the turbulent re-acceleration model. *Astron. Astrophys.*, 517:A10.

Cassano, R., Brunetti, G., Giocoli, C., and Ettori, S. (2016). Can giant radio halos probe the merging rate of galaxy clusters? *Astron. Astrophys.*, 593:A81.

Cassano, R., Ettori, S., Brunetti, G., Giacintucci, S., Pratt, G. W., Venturi, T., Kale, R., Dolag, K., and Markevitch, M. (2013). Revisiting Scaling Relations for Giant Radio Halos in Galaxy Clusters. *Astrophys. J.*, 777:141.

Cassano, R., Ettori, S., Giacintucci, S., Brunetti, G., Markevitch, M., Venturi, T., and Gitti, M. (2010). On the Connection Between Giant Radio Halos and Cluster Mergers. *Astrophys. J. Lett.*, 721:L82–L85.

Cavagnolo, K. W., Donahue, M., Voit, G. M., and Sun, M. (2009). Intracluster Medium Entropy Profiles for a Chandra Archival Sample of Galaxy Clusters. *Astrophys. J. Supp.*, 182:12–32.

Chengular, J. N., Gupta, Y., and Dwarakanath, K. (2003). *Low Frequency Radio Astronomy.* Rajaram Nityananda, Pune, India.

Clark, B. G. (1980). An efficient implementation of the algorithm 'CLEAN'. *Astron. Astrophys.*, 89:377.

Clowe, D., Gonzalez, A., and Markevitch, M. (2004). Weak-Lensing Mass Reconstruction of the Interacting Cluster 1E 0657-558: Direct Evidence for the Existence of Dark Matter. *Astrophys. J.*, 604:596–603.

Condon, J. J., Cotton, W. D., Greisen, E. W., Yin, Q. F., Perley, R. A., Taylor, G. B., and Broderick, J. J. (1998). The NRAO VLA Sky Survey. *Astron. J.*, 115:1693–1716.

Cornwell, T. J. and Perley, R. A. (1992). Radio-interferometric imaging of very large fields - The problem of non-coplanar arrays. *Astron. Astrophys.*, 261:353–364.

Cotton, W. D. (2008). Obit: A Development Environment for Astronomical Algorithms. *Pub. Astron. Soc. Pacific*, 120:439–448.

Cotton, W. D., Condon, J. J., Perley, R. A., Kassim, N., Lazio, J., Cohen, A., Lane, W., and Erickson, W. C. (2004). Beyond the isoplanatic patch in the VLA Low-frequency Sky

Survey. In Oschmann, Jr., J. M., editor, *Ground-based Telescopes*, volume 5489 of , pages 180–189.

Croston, J. H., Pratt, G. W., Böhringer, H., Arnaud, M., Pointecouteau, E., Ponman, T. J., Sanderson, A. J. R., Temple, R. F., Bower, R. G., and Donahue, M. (2008). Galaxy-cluster gas-density distributions of the representative XMM-Newton cluster structure survey (REXCESS). *Astron. Astrophys.*, 487:431–443.

Cuciti, V., Cassano, R., Brunetti, G., Dallacasa, D., Kale, R., Ettori, S., and Venturi, T. (2015). Occurrence of radio halos in galaxy clusters. Insight from a mass-selected sample. *Astron. Astrophys.*, 580:A97.

Czakon, N. G., Sayers, J., Mantz, A., Golwala, S. R., Downes, T. P., Koch, P. M., Lin, K.-Y., Molnar, S. M., Moustakas, L. A., Mroczkowski, T., Pierpaoli, E., Shitanishi, J. A., Siegel, S., and Umetsu, K. (2015). Galaxy Cluster Scaling Relations between Bolocam Sunyaev-Zel'dovich Effect and Chandra X-Ray Measurements. *Astrophys. J.*, 806:18.

Das, S., Louis, T., Nolta, M. R., Addison, G. E., Battistelli, E. S., Bond, J. R., Calabrese, E., Crichton, D., Devlin, M. J., Dicker, S., Dunkley, J., Dünner, R., Fowler, J. W., Gralla, M., Hajian, A., Halpern, M., Hasselfield, M., Hilton, M., Hincks, A. D., Hlozek, R., Huffenberger, K. M., Hughes, J. P., Irwin, K. D., Kosowsky, A., Lupton, R. H., Marriage, T. A., Marsden, D., Menanteau, F., Moodley, K., Niemack, M. D., Page, L. A., Partridge, B., Reese, E. D., Schmitt, B. L., Sehgal, N., Sherwin, B. D., Sievers, J. L., Spergel, D. N., Staggs, S. T., Swetz, D. S., Switzer, E. R., Thornton, R., Trac, H., and Wollack, E. (2014). The Atacama Cosmology Telescope: temperature and gravitational lensing power spectrum measurements from three seasons of data. *Journal of Cosmology and Astroparticle Physics.*, 4:014.

de Gasperin, F., Ogrean, G. A., van Weeren, R. J., Dawson, W. A., Brüggen, M., Bonafede, A., and Simionescu, A. (2015). Abell 1033: birth of a radio phoenix. *Mon. Not. R. Astron. Soc.*, 448:2197–2209.

Dicke, R. H. (1954). Coherence in Spontaneous Radiation Processes. *Physical Review*, 93:99–110.

Donnert, J., Dolag, K. andBrunetti, G., and Cassano, R. (2013). Rise and fall of radio haloes in simulated merging galaxy clusters. *Mon. Not. R. Astron. Soc.*, 429:3564–3569.

Donnert, J., Dolag, K., Cassano, R., and Brunetti, G. (2010). Radio haloes from simulations and hadronic models - II. The scaling relations of radio haloes. *Mon. Not. R. Astron. Soc.*, 407:1565–1580.

Donnert, J. M. F. (2013). Modelling giant radio halos. Doctoral Thesis Award Lecture 2012. *Astronomische Nachrichten*, 334:515.

Dvali, G., Gabadadze, G., and Porrati, M. (2000). 4D gravity on a brane in 5D Minkowski space. *Physics Letters B*, 485:208–214.

Einstein, A. (1917). Kosmologische Betrachtungen zur allgemeinen Relativitätstheorie. *Sitzungsberichte der Königlich Preußischen Akademie der Wissenschaften (Berlin), Seite 142-152.*

Enßlin, T. A., Biermann, P. L., Klein, U., and Kohle, S. (1998). Cluster radio relics as a tracer of shock waves of the large-scale structure formation. *Astron. Astrophys.*, 332:395–409.

Enßlin, T. A. and Brüggen, M. (2002). On the formation of cluster radio relics. *Mon. Not. R. Astron. Soc.*, 331:1011–1019.

Enßlin, T. A. and Röttgering, H. (2002). The radio luminosity function of cluster radio halos. *Astron. Astrophys.*, 396:83–89.

Erickson, W. C. (1984). Ionospheric refraction in radio source observations at long radio wavelengths. *Journal of Astrophysics and Astronomy*, 5:55–65.

Ettori, S., Gastaldello, F., Leccardi, A., Molendi, S., Rossetti, M., Buote, D., and Meneghetti, M. (2010). Mass profiles and c-M_{DM} relation in X-ray luminous galaxy clusters. *Astron. Astrophys.*, 524:A68.

Feretti, L., Giovannini, G., Govoni, F., and Murgia, M. (2012). Clusters of galaxies: observational properties of the diffuse radio emission. *Astron. Astrophys. Rev.*, 20:54.

Foot, R. and Vagnozzi, S. (2016). Solving the small-scale structure puzzles with dissipative dark matter. *Journal of Cosmology and Astroparticle Physics.*, 7:013.

Fu, L., Kilbinger, M., Erben, T., Heymans, C., Hildebrandt, H., Hoekstra, H., Kitching, T. D., Mellier, Y., Miller, L., Semboloni, E., Simon, P., Van Waerbeke, L., Coupon, J.,

Harnois-Déraps, J., Hudson, M. J., Kuijken, K., Rowe, B., Schrabback, T., Vafaei, S., and Velander, M. (2014). CFHTLenS: cosmological constraints from a combination of cosmic shear two-point and three-point correlations. *Mon. Not. R. Astron. Soc.*, 441:2725–2743.

Garrett, M. A., Porcas, R. W., Pedlar, A., Muxlow, T. W. B., and Garrington, S. T. (1999). Wide-field VLBI imaging. *New Astron. Rev.*, 43:519–522.

George, E. M., Reichardt, C. L., Aird, K. A., Benson, B. A., Bleem, L. E., Carlstrom, J. E., Chang, C. L., Cho, H.-M., Crawford, T. M., Crites, A. T., de Haan, T., Dobbs, M. A., Dudley, J., Halverson, N. W., Harrington, N. L., Holder, G. P., Holzapfel, W. L., Hou, Z., Hrubes, J. D., Keisler, R., Knox, L., Lee, A. T., Leitch, E. M., Lueker, M., Luong-Van, D., McMahon, J. J., Mehl, J., Meyer, S. S., Millea, M., Mocanu, L. M., Mohr, J. J., Montroy, T. E., Padin, S., Plagge, T., Pryke, C., Ruhl, J. E., Schaffer, K. K., Shaw, L., Shirokoff, E., Spieler, H. G., Staniszewski, Z., Stark, A. A., Story, K. T., van Engelen, A., Vanderlinde, K., Vieira, J. D., Williamson, R., and Zahn, O. (2015). A Measurement of Secondary Cosmic Microwave Background Anisotropies from the 2500 Square-degree SPT-SZ Survey. *Astrophys. J.*, 799:177.

Giacconi, R., Murray, S., Gursky, H., Kellogg, E., Schreier, E., and Tananbaum, H. (1972). The Uhuru catalog of X-ray sources. *Astrophys. J.*, 178:281–308.

Giacconi, R., Zirm, A., Wang, J., Rosati, P., Nonino, M., Tozzi, P., Gilli, R., Mainieri, V., Hasinger, G., Kewley, L., Bergeron, J., Borgani, S., Gilmozzi, R., Grogin, N., Koekemoer, A., Schreier, E., Zheng, W., and Norman, C. (2002). Chandra Deep Field South: The 1 Ms Catalog. *Astrophys. J. Supp.*, 139:369–410.

Giacintucci, S., Markevitch, M., Brunetti, G., Cassano, R., and Venturi, T. (2011). A radio minihalo in the extreme cool-core galaxy cluster RXC J1504.1-0248. *Astron. Astrophys.*, 525:L10.

Giacintucci, S., O'Sullivan, E., Clarke, T. E., Murgia, M., Vrtilek, J. M., Venturi, T., David, L. P., Raychaudhury, S., and Athreya, R. M. (2012). Recurrent Radio Outbursts at the Center of the NGC 1407 Galaxy Group. *Astrophys. J.*, 755:172.

Giacintucci, S., Venturi, T., Macario, G., Dallacasa, D., Brunetti, G., Markevitch, M., Cassano, R., Bardelli, S., and Athreya, R. (2008). Shock acceleration as origin of the radio relic in A 521? *Astron. Astrophys.*, 486:347–358.

Gil-Marín, H., Percival, W. J., Verde, L., Brownstein, J. R., Chuang, C.-H., Kitaura, F.-S., Rodríguez-Torres, S. A., and Olmstead, M. D. (2016). The clustering of galaxies in the SDSS-III Baryon Oscillation Spectroscopic Survey: RSD measurement from the power spectrum and bispectrum of the DR12 BOSS galaxies. *ArXiv e-prints 1606.00439*.

Giovannini, G. and Feretti, L. (2000). Halo and relic sources in clusters of galaxies. *New Astron.*, 5:335–347.

Giovannini, G. and Feretti, L. (2004). Radio Relics in Clusters of Galaxies. *Journal of Korean Astronomical Society*, 37:323–328.

Gitti, M., Giroletti, M., Giovannini, G., Feretti, L., and Liuzzo, E. (2014). Twin SMBH candidates in the BCG of RBS 797. In *Proceedings of the 12th European VLBI Network Symposium and Users Meeting (EVN 2014). 7-10 October 2014. Cagliari, Italy. Online at ¡A href="http://pos.sissa.it/cgi-bin/reader/conf.cgi?confid=230"¿http://pos.sissa.it/cgi-bin/reader/conf.cgi?confid=230¡/A¿, id.82*, page 82.

Gitti, M., Tozzi, P., Brunetti, G., Cassano, R., Dallacasa, D., Edge, A., Ettori, S., Feretti, L., Ferrari, C., Giacintucci, S., Giovannini, G., Hogan, M., and Venturi, T. (2015). The SKA view of cool-core clusters: evolution of radio mini-halos and AGN feedback. *Advancing Astrophysics with the Square Kilometre Array (AASKA14)*, page 76.

Govoni, F., Feretti, L., Giovannini, G., Böhringer, H., Reiprich, T. H., and Murgia, M. (2001). Radio and X-ray diffuse emission in six clusters of galaxies. *Astron. Astrophys.*, 376:803–819.

Govoni, F., Murgia, M., Xu, H., Li, H., Norman, M., Feretti, L., Giovannini, G., Vacca, V., Bernardi, G., Bonafede, A., Brunetti, G., Carretti, E., Colafrancesco, S., Donnert, J., Ferrari, C., Gitti, M., Iapichino, L., Johnston-Hollitt, M., Pizzo, R., and Rudnick, L. (2015). Cluster magnetic fields through the study of polarized radio halos in the SKA era. *Advancing Astrophysics with the Square Kilometre Array (AASKA14)*, page 105.

Harris, D. E., Stern, C. P., Willis, A. G., and Dewdney, P. E. (1993). The megaparsec radio relic in supercluster, Rood No. 27. *Astron. J.*, 105:769–777.

Haslam, C. G. T., Salter, C. J., and Stoffel, H. (1981). The All-Sky 408-MHZ Survey. In Setti, G., Spada, G., and Wolfendale, A. W., editors, *Origin of Cosmic Rays*, volume 94 of *IAU Symposium*, page 217.

Hasselfield, M., Hilton, M., Marriage, T. A., Addison, G. E., Barrientos, L. F., Battaglia, N., Battistelli, E. S., Bond, J. R., Crichton, D., Das, S., Devlin, M. J., Dicker, S. R., Dunkley, J., Dünner, R., Fowler, J. W., Gralla, M. B., Hajian, A., Halpern, M., Hincks, A. D., Hlozek, R., Hughes, J. P., Infante, L., Irwin, K. D., Kosowsky, A., Marsden, D., Menanteau, F., Moodley, K., Niemack, M. D., Nolta, M. R., Page, L. A., Partridge, B., Reese, E. D., Schmitt, B. L. andSehgal, N., Sherwin, B. D., Sievers, J., Sifón, C., Spergel, D. N., Staggs, S. T., Swetz, D. S., Switzer, E. R., Thornton, R., Trac, H., and Wollack, E. J. (2013). The Atacama Cosmology Telescope: Sunyaev-Zel'dovich selected galaxy clusters at 148 GHz from three seasons of data. *Journal of Cosmology and Astroparticle Physics.*, 7:008.

Helfand, D. J., White, R. L., and Becker, R. H. (2015). The Last of FIRST: The Final Catalog and Source Identifications. *Astrophys. J.*, 801:26.

Hildebrandt, H., Viola, M., Heymans, C., Joudaki, S., Kuijken, K., Blake, C., Erben, T., Joachimi, B., Klaes, D., Miller, L., Morrison, C. B., Nakajima, R., Verdoes Kleijn, G., Amon, A., Choi, A., Covone, G., de Jong, J. T. A., Dvornik, A., Fenech Conti, I., Grado, A., Harnois-Déraps, J., Herbonnet, R., Hoekstra, H., Köhlinger, F., McFarland, J., Mead, A., Merten, J., Napolitano, N., Peacock, J. A., Radovich, M., Schneider, P., Simon, P., Valentijn, E. A., van den Busch, J. L., van Uitert, E., and Van Waerbeke, L. (2016). KiDS-450: Cosmological parameter constraints from tomographic weak gravitational lensing. *ArXiv e-prints 1606.05338*.

Hoeft, M. and Brüggen, M. (2003). Radio Ghosts: Motion and Reactivation of Fossil Radio Plasma. *Astronomische Nachrichten Supplement*, 324:171.

Högbom, J. A. (1974). Aperture Synthesis with a Non-Regular Distribution of Interferometer Baselines. *Astron. Astrophys. Supp.*, 15:417.

Hu, W. and Dodelson, S. (2002). Cosmic Microwave Background Anisotropies. *Annu. Rev. Astron. Astrophys.*, 40:171–216.

Hubble, E. (1929). A Relation between Distance and Radial Velocity among Extra-Galactic Nebulae. *Proceedings of the National Academy of Science*, 15:168–173.

Hudson, D. S., Mittal, R., Reiprich, T. H., Nulsen, P. E. J., Andernach, H., and Sarazin, C. L. (2010). What is a cool-core cluster? a detailed analysis of the cores of the X-ray flux-limited HIFLUGCS cluster sample. *Astron. Astrophys.*, 513:A37.

Intema, H. T. (2014). SPAM: Source Peeling and Atmospheric Modeling. Astrophysics Source Code Library.

Intema, H. T., van der Tol, S., Cotton, W. D., Cohen, A. S., van Bemmel, I. M., and Röttgering, H. J. A. (2009). Ionospheric calibration of low frequency radio interferometric observations using the peeling scheme. I. Method description and first results. *Astron. Astrophys.*, 501:1185–1205.

Jacob, S. and Pfrommer, C. (2016). Cosmic ray heating in cool core clusters I: diversity of steady state solutions. *ArXiv e-prints 1609.06321*.

Jaffe, W. J. (1977). Origin and transport of electrons in the halo radio source in the Coma cluster. *Astrophys. J.*, 212:1–7.

Jansky, K. G. (1933). Radio Waves from Outside the Solar System. *Nature.*, 132:66.

Jenkins, A., Frenk, C. S., White, S. D. M., Colberg, J. M., Cole, S., Evrard, A. E., Couchman, H. M. P., and Yoshida, N. (2001). The mass function of dark matter haloes. *Mon. Not. R. Astron. Soc.*, 321:372–384.

Kaiser, N. (1986). Evolution and clustering of rich clusters. *Mon. Not. R. Astron. Soc.*, 222:323–345.

Kajita, T. (2016). Discovery of Atmospheric Neutrino Oscillations. *International Journal of Modern Physics A*, 31:1630047–880.

Kale, R. and Dwarakanath, K. S. (2009). Diffuse Radio Emission in Abell 754. *Astrophys. J.*, 699:1883–1890.

Kale, R. and Parekh, V. (2016). How unusual is the cool-core radio halo cluster CL1821+643? *Mon. Not. R. Astron. Soc.*, 459:2940–2947.

Kale, R., Venturi, T., Cassano, R., Giacintucci, S., Bardelli, S., Dallacasa, D., and Zucca, E. (2015). Brightest cluster galaxies in the extended GMRT radio halo cluster sample. Radio properties and cluster dynamics. *Astron. Astrophys.*, 581:A23.

Kang, H. and Ryu, D. (2016). Re-acceleration Model for Radio Relics with Spectral Curvature. *Astrophys. J.*, 823:13.

Kettenis, M., van Langevelde, H. J., Reynolds, C., and Cotton, B. (2006). ParselTongue: AIPS Talking Python. In Gabriel, C., Arviset, C., Ponz, D., and Enrique, S., editors, *Astronomical Data Analysis Software and Systems XV*, volume 351 of *Astronomical Society of the Pacific Conference Series*, page 497.

Kirk, B., Hilton, M., Cress, C., Crawford, S. M., Hughes, J. P., Battaglia, N., Bond, J. R., Burke, C., Gralla, M. B., Hajian, A., Hasselfield, M., Hincks, A. D., Infante, L., Kosowsky, A., Marriage, T. A., Menanteau, F., Moodley, K., Niemack, M. D., Sievers, J. L., Sifón, C., Wilson, S., Wollack, E. J., and Zunckel, C. (2015). SALT spectroscopic observations of galaxy clusters detected by ACT and a type II quasar hosted by a brightest cluster galaxy. *Mon. Not. R. Astron. Soc.*, 449:4010–4026.

Knowles, K., Intema, H. T. andBaker, A. J., Bond, J. R., Cress, C., Gupta, N., Hajian, A., Hilton, M., Hincks, A. D., Hlozek, R., Hughes, J. P., Lindner, R., Marriage, T. A., Menanteau, F., Moodley, K. andNiemack, M. D., Reese, E. D., Sievers, J., Sifón, C., Srianand, R., and Wollack, E. J. (2015). A giant radio halo in a low-mass SZ-selected galaxy cluster: ACT-CL J0256.5+0006. *ArXiv e-prints 1506.01547*.

Knowles, K., Intema, H. T., Baker, A. J., Bharadwaj, V., Bond, J. R., Cress, C., Gupta, N., Hajian, A., Hilton, M., Hincks, A. D., Hlozek, R., Hughes, J. P., Lindner, R. R., Marriage, T. A., Menanteau, F., Moodley, K., Niemack, M. D., Reese, E. D., Sievers, J., Sifón, C., Srianand, R., and Wollack, E. J. (2016). A giant radio halo in a low-mass SZ-selected galaxy cluster: ACT-CL J0256.5+0006. *Mon. Not. R. Astron. Soc.*, 459:4240–4258.

Knowles, K. L. (2016). *Observational probes of merging galaxy clusters*. PhD dissertation, University of KwaZulu-Natal.

Kraus, J. D. (1966). *Radio astronomy*.

Kravtsov, A. V. and Borgani, S. (2012). Formation of Galaxy Clusters. *Annu. Rev. Astron. Astrophys.*, 50:353–409.

Kuo, P.-H., Hwang, C.-Y., and Ip, W.-H. (2003). Diagnostic Signatures of Radio and Hard X-Ray Emission on Particle Acceleration Processes in the Coma Cluster. *Astrophys. J.*, 594:732–740.

Leccardi, A. and Molendi, S. (2008). Radial temperature profiles for a large sample of galaxy clusters observed with XMM-Newton. *Astron. Astrophys.*, 486:359–373.

Lemaître, G. (1931). Expansion of the universe, A homogeneous universe of constant mass and increasing radius accounting for the radial velocity of extra-galactic nebulae. *Mon. Not. R. Astron. Soc.*, 91:483–490.

Lemaître, G. (1949). Cosmological Application of Relativity. *Reviews of Modern Physics*, 21:357–366.

Lesgourgues, J., Viel, M., Haehnelt, M. G., and Massey, R. (2007). A combined analysis of 3D weak lensing, Lyman-α forest and WMAP year three data. *Journal of Cosmology and Astroparticle Physics.*, 11:008.

Lewis, A. and Challinor, A. (2006). Weak gravitational lensing of the CMB. *Phys. Rep.*, 429:1–65.

Liang, H., Hunstead, R. W., Birkinshaw, M., and Andreani, P. (2000). A Powerful Radio Halo in the Hottest Known Cluster of Galaxies 1E 0657-56. *Astrophys. J.*, 544:686–701.

Linden, T., Hooper, D., and Yusef-Zadeh, F. (2011). Dark Matter and Synchrotron Emission from Galactic Center Radio Filaments. *Astrophys. J.*, 741:95.

Loi, S. T., Murphy, T., Bell, M. E., Kaplan, D. L., Lenc, E., Offringa, A. R., Hurley-Walker, N., Bernardi, G., Bowman, J. D., Briggs, F., Cappallo, R. J., Corey, B. E., Deshpande, A. A., Emrich, D., Gaensler, B. M., Goeke, R., Greenhill, L. J., Hazelton, B. J., Johnston-Hollitt, M., Kasper, J. C., Kratzenberg, E., Lonsdale, C. J., Lynch, M. J., McWhirter, S. R., Mitchell, D. A., Morales, M. F., Morgan, E., Oberoi, D., Ord, S. M., Prabu, T., Rogers, A. E. E., Roshi, A., Shankar, N. U., Srivani, K. S., Subrahmanyan, R., Tingay, S. J., Waterson, M., Wayth, R. B., Webster, R. L., Whitney, A. R., Williams, A., and Williams, C. L. (2015). Quantifying ionospheric effects on time-domain astrophysics with the Murchison Widefield Array. *Mon. Not. R. Astron. Soc.*, 453:2731–2746.

Lonsdale, C. J. (2005). Configuration Considerations for Low Frequency Arrays. In Kassim, N., Perez, M., Junor, W., and Henning, P., editors, *From Clark Lake to the Long Wavelength Array: Bill Erickson's Radio Science*, volume 345 of *Astronomical Society of the Pacific Conference Series*, page 399.

Louis, T., Grace, E., Hasselfield, M., Lungu, M., Maurin, L., Addison, G. E., Ade, P. A. R., Aiola, S., Allison, R., Amiri, M., Angile, E., Battaglia, N., Beall, J. A., de Bernardis, F., Bond, J. R., Britton, J., Calabrese, E., Cho, H.-m., Choi, S. K., Coughlin, K., Crichton, D., Crowley, K., Datta, R., Devlin, M. J., Dicker, S. R., Dunkley, J., Dünner, R., Ferraro, S., Fox, A. E., Gallardo, P., Gralla, M., Halpern, M., Henderson, S., Hill, J. C., Hilton, G. C., Hilton, M., Hincks, A. D., Hlozek, R., Ho, S. P. P., Huang, Z., Hubmayr, J., Huffenberger, K. M., Hughes, J. P., Infante, L., Irwin, K., Muya Kasanda, S., Klein, J., Koopman, B., Kosowsky, A., Li, D., Madhavacheril, M., Marriage, T. A., McMahon, J., Menanteau, F., Moodley, K., Munson, C., Naess, S., Nati, F., Newburgh, L., Nibarger, J., Niemack, M. D., Nolta, M. R., Nuñez, C., Page, L. A., Pappas, C., Partridge, B., Rojas, F., Schaan, E., Schmitt, B. L., Sehgal, N., Sherwin, B. D., Sievers, J., Simon, S., Spergel, D. N., Staggs, S. T., Switzer, E. R., Thornton, R., Trac, H., Treu, J., Tucker, C., Van Engelen, A., Ward, J. T., and Wollack, E. J. (2016). The Atacama Cosmology Telescope: Two-Season ACTPol Spectra and Parameters. *ArXiv e-prints 1610.02360*.

Macario, G., Venturi, T., Brunetti, G., Dallacasa, D., Giacintucci, S., Cassano, R., Bardelli, S., and Athreya, R. (2010). The very steep spectrum radio halo in Abell 697. *Astron. Astrophys.*, 517:A43.

Malu, S., Datta, A., and Sandhu, P. (2016). First detection at 5.5 and 9 GHz of the radio relics in bullet cluster with ATCA. *Astrophys. Space Sci.*, 361:255.

Mana, A., Giannantonio, T., Weller, J., Hoyle, B., Hütsi, G., and Sartoris, B. (2013). Combining clustering and abundances of galaxy clusters to test cosmology and primordial non-Gaussianity. *Mon. Not. R. Astron. Soc.*, 434:684–695.

Markevitch, M., Gonzalez, A. H., Clowe, D., Vikhlinin, A., Forman, W., Jones, C., Murray, S., and Tucker, W. (2004). Direct Constraints on the Dark Matter Self-Interaction Cross Section from the Merging Galaxy Cluster 1E 0657-56. *Astrophys. J.*, 606:819–824.

Markevitch, M., Govoni, F., Brunetti, G., and Jerius, D. (2005). Bow Shock and Radio Halo in the Merging Cluster A520. *Astrophys. J.*, 627:733–738.

Marriage, T. A., Acquaviva, V., Ade, P. A. R., Aguirre, P., Amiri, M., Appel, J. W., Barrientos, L. F., Battistelli, E. S., Bond, J. R., Brown, B., Burger, B., Chervenak, J., Das, S., Devlin, M. J., Dicker, S. R., Bertrand Doriese, W., Dunkley, J., Dünner, R.,

Essinger-Hileman, T., Fisher, R. P., Fowler, J. W., Hajian, A., Halpern, M., Hasselfield, M., Hernández-Monteagudo, C., Hilton, G. C., Hilton, M., Hincks, A. D., Hlozek, R., Huffenberger, K. M., Handel Hughes, D., Hughes, J. P., Infante, L., Irwin, K. D., Baptiste Juin, J., Kaul, M., Klein, J., Kosowsky, A., Lau, J. M., Limon, M., Lin, Y.-T., Lupton, R. H., Marsden, D., Martocci, K., Mauskopf, P., Menanteau, F., Moodley, K., Moseley, H., Netterfield, C. B., Niemack, M. D., Nolta, M. R., Page, L. A., Parker, L., Partridge, B., Quintana, H., Reese, E. D., Reid, B., Sehgal, N., Sherwin, B. D., Sievers, J., Spergel, D. N., Staggs, S. T., Swetz, D. S., Switzer, E. R., Thornton, R., Trac, H., Tucker, C., Warne, R., Wilson, G., Wollack, E., and Zhao, Y. (2011). The Atacama Cosmology Telescope: Sunyaev-Zel'dovich-Selected Galaxy Clusters at 148 GHz in the 2008 Survey. *Astrophys. J.*, 737:61.

Mazzotta, P. and Giacintucci, S. (2008). Do Radio Core-Halos and Cold Fronts in Non-Major-Merging Clusters Originate from the Same Gas Sloshing? *Astrophys. J. Lett.*, 675:L9.

McDonald, A. B. (2006). Sudbury Neutrino Observatory Results. In Bergström, L., Hulth, P. O., Botner, O., Carlson, P., and Ohlsson, T., editors, *Neutrino Physics*, pages 29–32.

Menanteau, F., Sifón, C., Barrientos, L. F., Battaglia, N., Bond, J. R., Crichton, D., Das, S., Devlin, M. J., Dicker, S., Dünner, R., Gralla, M., Hajian, A., Hasselfield, M., Hilton, M., Hincks, A. D., Hughes, J. P., Infante, L., Kosowsky, A., Marriage, T. A., Marsden, D., Moodley, K., Niemack, M. D., Nolta, M. R., Page, L. A., Partridge, B., Reese, E. D., Schmitt, B. L., Sievers, J., Spergel, D. N., Staggs, S. T., Switzer, E., and Wollack, E. J. (2013). The Atacama Cosmology Telescope: Physical Properties of Sunyaev-Zel'dovich Effect Clusters on the Celestial Equator. *Astrophys. J.*, 765:67.

Merten, J. and CLASH (2014). The Concentration-Mass Relation from CLASH. In *American Astronomical Society Meeting Abstracts #223*, volume 223 of *American Astronomical Society Meeting Abstracts*, page 139.01.

Michelson, A. A. and Pease, F. G. (1922). Interferometer Measures of Star Diameters. In *Publications of the American Astronomical Society*, volume 4 of *Publications of the American Astronomical Society*, page 375.

Miniati, F., Jones, T. W., Kang, H., and Ryu, D. (2001). Cosmic-Ray Electrons in Groups

and Clusters of Galaxies: Primary and Secondary Populations from a Numerical Cosmological Simulation. *Astrophys. J.*, 562:233–253.

Mohan, N. and Rafferty, D. (2015). PyBDSM: Python Blob Detection and Source Measurement. Astrophysics Source Code Library.

Naess, S., Hasselfield, M., McMahon, J., Niemack, M. D., Addison, G. E., Ade, P. A. R., Allison, R., Amiri, M., Battaglia, N., Beall, J. A., de Bernardis, F., Bond, J. R., Britton, J., Calabrese, E., Cho, H.-m., Coughlin, K., Crichton, D., Das, S., Datta, R., Devlin, M. J., Dicker, S. R., Dunkley, J., Dünner, R., Fowler, J. W., Fox, A. E., Gallardo, P., Grace, E., Gralla, M., Hajian, A., Halpern, M., Henderson, S., Hill, J. C., Hilton, G. C., Hilton, M., Hincks, A. D., Hlozek, R., Ho, P., Hubmayr, J., Huffenberger, K. M., Hughes, J. P., Infante, L., Irwin, K., Jackson, R., Muya Kasanda, S., Klein, J., Koopman, B., Kosowsky, A., Li, D., Louis, T., Lungu, M., Madhavacheril, M., Marriage, T. A., Maurin, L., Menanteau, F., Moodley, K., Munson, C., Newburgh, L., Nibarger, J., Nolta, M. R., Page, L. A., Pappas, C., Partridge, B., Rojas, F., Schmitt, B. L., Sehgal, N., Sherwin, B. D., Sievers, J., Simon, S., Spergel, D. N., Staggs, S. T., Switzer, E. R., Thornton, R., Trac, H., Tucker, C., Uehara, M., Van Engelen, A., Ward, J. T., and Wollack, E. J. (2014). The Atacama Cosmology Telescope: CMB polarization at 200 l 9000. *Journal of Cosmology and Astroparticle Physics.*, 10:007.

Noordam, J. E. (2004). LOFAR calibration challenges. In Oschmann, Jr., J. M., editor, *Ground-based Telescopes*, volume 5489 of , pages 817–825.

Odderskov, I. and Hannestad, S. (2016). Measuring the velocity field from type Ia supernovae in an LSST-like sky survey. *ArXiv e-prints 1608.04446*.

Olive, K. A. and Particle Data Group (2014). Review of Particle Physics. *Chinese Physics C*, 38(9):090001.

Oort, J. H. (1932). The force exerted by the stellar system in the direction perpendicular to the galactic plane and some related problems. , 6:249.

Papovich, C., Momcheva, I., Willmer, C. N. A., Finkelstein, K. D., Finkelstein, S. L., Tran, K.-V., Brodwin, M., Dunlop, J. S., Farrah, D., Khan, S. A., Lotz, J., McCarthy, P., McLure, R. J., Rieke, M., Rudnick, G., Sivanandam, S., Pacaud, F., and Pierre, M. (2010). A Spitzer-selected Galaxy Cluster at z = 1.62. *Astrophys. J.*, 716:1503–1513.

Paraficz, D., Kneib, J.-P., Richard, J., Morandi, A., Limousin, M., Jullo, E., and Martinez, J. (2016). The Bullet cluster at its best: weighing stars, gas, and dark matter. *Astron. Astrophys.*, 594:A121.

Parkinson, D., Riemer-Sørensen, S., Blake, C., Poole, G. B., Davis, T. M., Brough, S., Colless, M., Contreras, C., Couch, W., Croom, S., Croton, D., Drinkwater, M. J., Forster, K., Gilbank, D., Gladders, M., Glazebrook, K., Jelliffe, B., Jurek, R. J., Li, I.-h., Madore, B., Martin, D. C., Pimbblet, K., Pracy, M., Sharp, R., Wisnioski, E., Woods, D., Wyder, T. K., and Yee, H. K. C. (2012). The WiggleZ Dark Energy Survey: Final data release and cosmological results. *Physical Review D.*, 86(10):103518.

Penzias, A. A. and Wilson, R. W. (1965). A Measurement of Excess Antenna Temperature at 4080 Mc/s. *Astrophys. J.*, 142:419–421.

Perley, R. A. (1989). Wide Field Imaging II: Imaging with Non-Coplanar Arrays. In Perley, R. A., Schwab, F. R., and Bridle, A. H., editors, *Synthesis Imaging in Radio Astronomy*, volume 6 of *Astronomical Society of the Pacific Conference Series*, page 259.

Perlmutter, S., Aldering, G., Goldhaber, G., Knop, R. A., Nugent, P., Castro, P. G., Deustua, S., Fabbro, S., Goobar, A., Groom, D. E., Hook, I. M., Kim, A. G., Kim, M. Y., Lee, J. C., Nunes, N. J., Pain, R., Pennypacker, C. R., Quimby, R., Lidman, C., Ellis, R. S., Irwin, M., McMahon, R. G., Ruiz-Lapuente, P., Walton, N., Schaefer, B., Boyle, B. J., Filippenko, A. V., Matheson, T., Fruchter, A. S., Panagia, N., Newberg, H. J. M., Couch, W. J., and Project, T. S. C. (1999). Measurements of Ω and Λ from 42 High-Redshift Supernovae. *Astrophys. J.*, 517:565–586.

Petrosian, V. (2001). On the Nonthermal Emission and Acceleration of Electrons in Coma and Other Clusters of Galaxies. *Astrophys. J.*, 557:560–572.

Planck Collaboration, Ade, P. A. R.and Aghanim, N., Arnaud, M., Ashdown, M., Atrio-Barandela, F., Aumont, J., Baccigalupi, C., Balbi, A., Banday, A. J., and et al. (2013). Planck intermediate results. V. Pressure profiles of galaxy clusters from the Sunyaev-Zeldovich effect. *Astron. Astrophys.*, 550:A131.

Planck Collaboration, Ade, P. A. R., Aghanim, N., Arnaud, M., Ashdown, M., Aumont, J., Baccigalupi, C., Banday, A. J., Barreiro, R. B., Barrena, R., and et al. (2016a).

Planck 2015 results. XXVII. The second Planck catalogue of Sunyaev-Zeldovich sources. *Astron. Astrophys.*, 594:A27.

Planck Collaboration, Ade, P. A. R., Aghanim, N., Arnaud, M., Ashdown, M., Aumont, J., Baccigalupi, C., Banday, A. J., Barreiro, R. B., Bartlett, J. G., and et al. (2016b). Planck 2015 results. XIII. Cosmological parameters. *Astron. Astrophys.*, 594:A13.

Prandoni, I. and Seymour, N. (2015). Revealing the Physics and Evolution of Galaxies and Galaxy Clusters with SKA Continuum Surveys. *Advancing Astrophysics with the Square Kilometre Array (AASKA14)*, page 67.

Pratt, G. W., Böhringer, H., Croston, J. H., Arnaud, M., Borgani, S., Finoguenov, A., and Temple, R. F. (2007). Temperature profiles of a representative sample of nearby X-ray galaxy clusters. *Astron. Astrophys.*, 461:71–80.

Press, W. H. and Schechter, P. (1974). Formation of Galaxies and Clusters of Galaxies by Self-Similar Gravitational Condensation. *Astrophys. J.*, 187:425–438.

Price, J. C. (1984). Land surface temperature measurements from the split window channels of the NOAA 7 Advanced Very High Resolution Radiometer. , 89:7231–7237.

Randall, S. W., Clarke, T. E., van Weeren, R. J., Intema, H. T., Dawson, W. A., Mroczkowski, T., Blanton, E. L., Bulbul, E., and Giacintucci, S. (2016). Multi-wavelength Observations of the Dissociative Merger in the Galaxy Cluster CIZA J0107.7+5408. *Astrophys. J.*, 823:94.

Rao Bandari, H., Sankarasubramanian, G., and Praveen Kumar, A. (2013). Wideband feeds for the upgraded GMRT. *Materials Science and Engineering Conference Series*, 44(1):012023.

Reichardt, C. L., Stalder, B. andBleem, L. E., Montroy, T. E., Aird, K. A., Andersson, K., Armstrong, R., Ashby, M. L. N., Bautz, M., Bayliss, M., Bazin, G., Benson, B. A., Brodwin, M., Carlstrom, J. E., Chang, C. L., Cho, H. M., Clocchiatti, A., Crawford, T. M., Crites, A. T., de Haan, T., Desai, S., Dobbs, M. A., Dudley, J. P., Foley, R. J., Forman, W. R., George, E. M., Gladders, M. D., Gonzalez, A. H., Halverson, N. W., Harrington, N. L., High, F. W., Holder, G. P., Holzapfel, W. L., Hoover, S., Hrubes, J. D., Jones, C., Joy, M., Keisler, R., Knox, L., Lee, A. T., Leitch, E. M., Liu, J., Lueker,

M., Luong-Van, D., Mantz, A., Marrone, D. P., McDonald, M., McMahon, J. J., Mehl, J., Meyer, S. S., Mocanu, L., Mohr, J. J., Murray, S. S., Natoli, T., Padin, S., Plagge, T., Pryke, C., Rest, A., Ruel, J., Ruhl, J. E., Saliwanchik, B. R., Saro, A., Sayre, J. T., Schaffer, K. K., Shaw, L., Shirokoff, E., Song, J., Spieler, H. G., Staniszewski, Z., Stark, A. A., Story, K., Stubbs, C. W., Šuhada, R., van Engelen, A., Vanderlinde, K., Vieira, J. D., Vikhlinin, A., Williamson, R., Zahn, O., and Zenteno, A. (2013). Galaxy Clusters Discovered via the Sunyaev-Zel'dovich Effect in the First 720 Square Degrees of the South Pole Telescope Survey. *Astrophys. J.*, 763:127.

Riess, A. G., Filippenko, A. V., Li, W., and Schmidt, B. P. (1999). Is there an Indication of Evolution of Type IA Supernovae from their Rise Times? *Astron. J.*, 118:2668–2674.

Robertson, A., Massey, R., and Eke, V. (2017). What does the Bullet Cluster tell us about self-interacting dark matter? *Mon. Not. R. Astron. Soc.*, 465:569–587.

Rood, H. J., Page, T. L., Kintner, E. C., and King, I. R. (1972). The Structure of the Coma Cluster of Galaxies. *Astrophys. J.*, 175:627.

Ross, A. J., Percival, W. J., and Manera, M. (2015). The information content of anisotropic Baryon Acoustic Oscillation scale measurements. *Mon. Not. R. Astron. Soc.*, 451:1331–1340.

Röttgering, H., Afonso, J., Barthel, P., Batejat, F., Best, P., Bonafede, A., Brüggen, M., Brunetti, G., Chyży, K., Conway, J., Gasperin, F. D., Ferrari, C., Haverkorn, M., Heald, G., Hoeft, M., Jackson, N., Jarvis, M., Ker, L., Lehnert, M., Macario, G., McKean, J., Miley, G., Morganti, R., Oosterloo, T., Orrù, E., Pizzo, R., Rafferty, D., Shulevski, A., Tasse, C., Bemmel, I. V., van der Tol, B., van Weeren, R., Verheijen, M., White, G., and Wise, M. (2011). LOFAR and APERTIF Surveys of the Radio Sky: Probing Shocks and Magnetic Fields in Galaxy Clusters. *Journal of Astrophysics and Astronomy*, 32:557–566.

Rottgering, H. J. A., Wieringa, M. H., Hunstead, R. W., and Ekers, R. D. (1997). The extended radio emission in the luminous X-ray cluster A3667. *Mon. Not. R. Astron. Soc.*, 290:577–584.

Rubin, V. C., Burbidge, E. M., Burbidge, G. R., and Prendergast, K. H. (1964). The Rotation and Mass of NGC 1792. *Astrophys. J.*, 140:80.

Rybicki, G. B. and Lightman, A. P. (1979). *Radiative processes in astrophysics*.

Ryle, M. (1952). A New Radio Interferometer and Its Application to the Observation of Weak Radio Stars. *Proceedings of the Royal Society of London Series A*, 211:351–375.

Ryle, M. and Vonberg, D. D. (1946). Solar Radiation on 175 Mc./s. *Nature.*, 158:339–340.

Sarazin, C. L. (2004). Mergers, Cosmic Rays, and Nonthermal Processes in Clusters of Galaxies. *Journal of Korean Astronomical Society*, 37:433–438.

Schaffer, K. K., Crawford, T. M., Aird, K. A., Benson, B. A., Bleem, L. E., Carlstrom, J. E., Chang, C. L., Cho, H. M., Crites, A. T., de Haan, T., Dobbs, M. A., George, E. M., Halverson, N. W., Holder, G. P., Holzapfel, W. L., Hoover, S., Hrubes, J. D., Joy, M., Keisler, R., Knox, L., Lee, A. T., Leitch, E. M., Lueker, M., Luong-Van, D., McMahon, J. J., Mehl, J., Meyer, S. S., Mohr, J. J., Montroy, T. E., Padin, S., Plagge, T., Pryke, C., Reichardt, C. L., Ruhl, J. E., Shirokoff, E., Spieler, H. G., Stalder, B., Staniszewski, Z., Stark, A. A., Story, K., Vanderlinde, K., Vieira, J. D., and Williamson, R. (2011). The First Public Release of South Pole Telescope Data: Maps of a 95 deg^2 Field from 2008 Observations. *Astrophys. J.*, 743:90.

Schuecker, P., Böhringer, H., Reiprich, T. H., and Feretti, L. (2001). A systematic study of X-ray substructure of galaxy clusters detected in the ROSAT All-Sky Survey. *Astron. Astrophys.*, 378:408–427.

Schwab, F. R. (1984). Optimal Gridding of Visibility Data in Radio Interferometry. In Roberts, J. A., editor, *Indirect Imaging. Measurement and Processing for Indirect Imaging*, pages 333–346.

Shimwell, T. W., Markevitch, M., Brown, S., Feretti, L., Gaensler, B. M., Johnston-Hollitt, M., Lage, C., and Srinivasan, R. (2015). Another shock for the Bullet cluster, and the source of seed electrons for radio relics. *Mon. Not. R. Astron. Soc.*, 449:1486–1494.

Sievers, J. L., Hlozek, R. A., Nolta, M. R., Acquaviva, V., Addison, G. E., Ade, P. A. R., Aguirre, P., Amiri, M., Appel, J. W., Barrientos, L. F., Battistelli, E. S., Battaglia, N., Bond, J. R., Brown, B., Burger, B., Calabrese, E., Chervenak, J., Crichton, D., Das, S., Devlin, M. J., Dicker, S. R., Bertrand Doriese, W., Dunkley, J., Dünner, R., Essinger-Hileman, T., Faber, D., Fisher, R. P., Fowler, J. W., Gallardo, P., Gordon, M. S., Gralla, M. B., Hajian, A., Halpern, M., Hasselfield, M., Hernández-Monteagudo, C., Hill, J. C., Hilton, G. C., Hilton, M., Hincks, A. D., Holtz, D., Huffenberger, K. M., Hughes, D. H.,

Hughes, J. P., Infante, L., Irwin, K. D., Jacobson, D. R., Johnstone, B., Baptiste Juin, J., Kaul, M., Klein, J., Kosowsky, A., Lau, J. M., Limon, M., Lin, Y.-T., Louis, T., Lupton, R. H., Marriage, T. A., Marsden, D., Martocci, K., Mauskopf, P., McLaren, M., Menanteau, F., Moodley, K., Moseley, H., Netterfield, C. B., Niemack, M. D., Page, L. A., Page, W. A., Parker, L., Partridge, B., Plimpton, R., Quintana, H., Reese, E. D., Reid, B., Rojas, F., Sehgal, N., Sherwin, B. D., Schmitt, B. L., Spergel, D. N., Staggs, S. T., Stryzak, O., Swetz, D. S., Switzer, E. R., Thornton, R., Trac, H., Tucker, C., Uehara, M., Visnjic, K., Warne, R., Wilson, G., Wollack, E., Zhao, Y., and Zunckel, C. (2013). The Atacama Cosmology Telescope: cosmological parameters from three seasons of data. *Journal of Cosmology and Astroparticle Physics.*, 10:060.

Slee, O. B., Roy, A. L., Murgia, M., Andernach, H., and Ehle, M. (2001). Four Extreme Relic Radio Sources in Clusters of Galaxies. *Astron. J.*, 122:1172–1193.

Smoot, G. F., Bennett, C. L., Kogut, A., Wright, E. L., Aymon, J., Boggess, N. W., Cheng, E. S., de Amici, G., Gulkis, S., Hauser, M. G., Hinshaw, G., Jackson, P. D., Janssen, M., Kaita, E., Kelsall, T., Keegstra, P., Lineweaver, C., Loewenstein, K., Lubin, P., Mather, J., Meyer, S. S., Moseley, S. H., Murdock, T., Rokke, L., Silverberg, R. F., Tenorio, L., Weiss, R., and Wilkinson, D. T. (1992). Structure in the COBE differential microwave radiometer first-year maps. *Astrophys. J. Lett.*, 396:L1–L5.

Sommer, M. W., Basu, K., Intema, H., Pacaud, F., Bonafede, A., Babul, A., and Bertoldi, F. (2016). Mpc-scale diffuse radio emission in two massive cool-core clusters of galaxies. *ArXiv e-prints 1610.07875*.

Spergel, D. N. and Steinhardt, P. J. (2000). Observational Evidence for Self-Interacting Cold Dark Matter. *Physical Review Letters*, 84:3760–3763.

Spoelstra, T. A. T. (1983). The influence of ionospheric refraction on radio astronomy interferometry. *Astron. Astrophys.*, 120:313–321.

Springel, V. and Farrar, G. R. (2007). The speed of the 'bullet' in the merging galaxy cluster 1E0657-56. *Mon. Not. R. Astron. Soc.*, 380:911–925.

Sullivan, M., Guy, J., Conley, A., Regnault, N., Astier, P., Balland, C., Basa, S., Carlberg, R. G., Fouchez, D., Hardin, D., Hook, I. M., Howell, D. A., Pain, R., Palanque-Delabrouille, N., Perrett, K. M., Pritchet, C. J., Rich, J., Ruhlmann-Kleider, V., Balam,

D., Baumont, S., Ellis, R. S., Fabbro, S., Fakhouri, H. K., Fourmanoit, N., González-Gaitán, S., Graham, M. L., Hudson, M. J., Hsiao, E., Kronborg, T., Lidman, C., Mourao, A. M., Neill, J. D., Perlmutter, S., Ripoche, P., Suzuki, N., and Walker, E. S. (2011). SNLS3: Constraints on Dark Energy Combining the Supernova Legacy Survey Three-year Data with Other Probes. *Astrophys. J.*, 737:102.

Sunyaev, R. A. and Zeldovich, Y. B. (1970). Small scale entropy and adiabatic density perturbations Antimatter in the Universe. *Astrophys. Space Sci.*, 9:368–382.

Sunyaev, R. A. and Zeldovich, Y. B. (1972). The Observations of Relic Radiation as a Test of the Nature of X-Ray Radiation from the Clusters of Galaxies. *Comments on Astrophysics and Space Physics*, 4:173.

Swarup, G. (1990). Giant metrewave radio telescope (GMRT) - Scientific objectives and design aspects. *Indian Journal of Radio and Space Physics*, 19:493–505.

Swetz, D. S., Ade, P. A. R., Amiri, M., Appel, J. W., Battistelli, E. S., Burger, B., Chervenak, J., Devlin, M. J., Dicker, S. R., Doriese, W. B., Dünner, R., Essinger-Hileman, T., Fisher, R. P., Fowler, J. W., Halpern, M., Hasselfield, M., Hilton, G. C., Hincks, A. D., Irwin, K. D., Jarosik, N., Kaul, M., Klein, J., Lau, J. M., Limon, M., Marriage, T. A., Marsden, D., Martocci, K., Mauskopf, P., Moseley, H., Netterfield, C. B., Niemack, M. D., Nolta, M. R., Page, L. A., Parker, L., Staggs, S. T., Stryzak, O., Switzer, E. R., Thornton, R., Tucker, C., Wollack, E., and Zhao, Y. (2011). Overview of the Atacama Cosmology Telescope: Receiver, Instrumentation, and Telescope Systems. *Astrophys. J. Supp.*, 194:41.

Thompson, A. R., Moran, J. M., and Swenson, G. W. (1986). *Interferometry and synthesis in radio astronomy.*

Thornton, R. J., Ade, P. A. R., Aiola, S., Angile, F. E., Amiri, M., Beall, J. A., Becker, D. T., Cho, H., Choi, S. K., Corlies, P., Coughlin, K. P., Datta, R., Devlin, M. J., Dicker, S. R., Dunner, R., Fowler, J. W., Fox, A. E., Gallardo, P. A., Gao, J., Grace, E., Halpern, M., Hasselfield, M., Henderson, S. W., Hilton, G. C., Hincks, A. D., Ho, S. P., Hubmayr, J., Irwin, K. D., Klein, J., Koopman, B., Li, D., Louis, T., Lungu, M., Maurin, L., McMahon, J., Munson, C. D., Naess, S., Nati, F., Newburgh, L., Nibarger, J., Niemack, M. D., Niraula, P., Nolta, M. R., Page, L. A., Pappas, C. G., Schillaci, A., Schmitt, B. L.,

Sehgal, N., Sievers, J. L., Simon, S. M., Staggs, S. T., Tucker, C., Uehara, M., van Lanen, J., Ward, J. T., and Wollack, E. J. (2016). The Atacama Cosmology Telescope: The polarization-sensitive ACTPol instrument. *ArXiv e-prints 1605.06569*.

Tingay, S. J., Goeke, R., Bowman, J. D., Emrich, D., Ord, S. M., Mitchell, D. A., Morales, M. F., Booler, T., Crosse, B., Wayth, R. B., Lonsdale, C. J., Tremblay, S., Pallot, D., Colegate, T., Wicenec, A., Kudryavtseva, N., Arcus, W., Barnes, D., Bernardi, G., Briggs, F., Burns, S., Bunton, J. D., Cappallo, R. J., Corey, B. E., Deshpande, A., Desouza, L., Gaensler, B. M., Greenhill, L. J., Hall, P. J., Hazelton, B. J., Herne, D., Hewitt, J. N., Johnston-Hollitt, M., Kaplan, D. L., Kasper, J. C., Kincaid, B. B., Koenig, R., Kratzenberg, E., Lynch, M. J., Mckinley, B., Mcwhirter, S. R., Morgan, E., Oberoi, D., Pathikulangara, J., Prabu, T., Remillard, R. A., Rogers, A. E. E., Roshi, A., Salah, J. E., Sault, R. J., Udaya-Shankar, N., Schlagenhaufer, F., Srivani, K. S., Stevens, J., Subrahmanyan, R., Waterson, M., Webster, R. L., Whitney, A. R., Williams, A., Williams, C. L., and Wyithe, J. S. B. (2013). The Murchison Widefield Array: The Square Kilometre Array Precursor at Low Radio Frequencies. , 30:e007.

Tinker, J., Kravtsov, A. V., Klypin, A., Abazajian, K., Warren, M., Yepes, G., Gottlöber, S., and Holz, D. E. (2008). Toward a Halo Mass Function for Precision Cosmology: The Limits of Universality. *Astrophys. J.*, 688:709–728.

Tucker, W., Blanco, P., Rappoport, S., David, L., Fabricant, D., Falco, E. E., Forman, W., Dressler, A., and Ramella, M. (1998). 1E 0657-56: A Contender for the Hottest Known Cluster of Galaxies. *Astrophys. J. Lett.*, 496:L5–L8.

van Cittert, P. H. (1958). Degree of coherence. *Physica*, 24:505–507.

van Haarlem, M. P., Wise, M. W., Gunst, A. W., Heald, G., McKean, J. P., Hessels, J. W. T., de Bruyn, A. G., Nijboer, R., Swinbank, J., Fallows, R., Brentjens, M., Nelles, A., Beck, R., Falcke, H., Fender, R., Hörandel, J., Koopmans, L. V. E., Mann, G., Miley, G., Röttgering, H., Stappers, B. W., Wijers, R. A. M. J., Zaroubi, S., van den Akker, M., Alexov, A., Anderson, J., Anderson, K., van Ardenne, A., Arts, M., Asgekar, A., Avruch, I. M., Batejat, F., Bähren, L., Bell, M. E., Bell, M. R., van Bemmel, I., Bennema, P., Bentum, M. J., Bernardi, G., Best, P., Bîrzan, L., Bonafede, A., Boonstra, A.-J., Braun, R., Bregman, J., Breitling, F., van de Brink, R. H., Broderick, J., Broekema, P. C., Brouw, W. N., Brüggen, M., Butcher, H. R., van Cappellen, W., Ciardi, B., Coenen, T.,

Conway, J., Coolen, A., Corstanje, A., Damstra, S., Davies, O., Deller, A. T., Dettmar, R.-J., van Diepen, G., Dijkstra, K., Donker, P., Doorduin, A., Dromer, J., Drost, M., van Duin, A., Eislöffel, J., van Enst, J., Ferrari, C., Frieswijk, W., Gankema, H., Garrett, M. A., de Gasperin, F., Gerbers, M., de Geus, E., Grießmeier, J.-M., Grit, T., Gruppen, P., Hamaker, J. P., Hassall, T., Hoeft, M., Holties, H. A., Horneffer, A., van der Horst, A., van Houwelingen, A., Huijgen, A., Iacobelli, M., Intema, H., Jackson, N., Jelic, V., de Jong, A., Juette, E., Kant, D., Karastergiou, A., Koers, A., Kollen, H., Kondratiev, V. I., Kooistra, E., Koopman, Y., Koster, A., Kuniyoshi, M., Kramer, M., Kuper, G., Lambropoulos, P., Law, C., van Leeuwen, J., Lemaitre, J., Loose, M., Maat, P., Macario, G., Markoff, S., Masters, J., McFadden, R. A., McKay-Bukowski, D., Meijering, H., Meulman, H., Mevius, M., Middelberg, E., Millenaar, R., Miller-Jones, J. C. A., Mohan, R. N., Mol, J. D., Morawietz, J., Morganti, R., Mulcahy, D. D., Mulder, E., Munk, H., Nieuwenhuis, L., van Nieuwpoort, R., Noordam, J. E., Norden, M., Noutsos, A., Offringa, A. R., Olofsson, H., Omar, A., Orrú, E., Overeem, R., Paas, H., Pandey-Pommier, M., Pandey, V. N., Pizzo, R., Polatidis, A., Rafferty, D., Rawlings, S., Reich, W., de Reijer, J.-P., Reitsma, J., Renting, G. A., Riemers, P., Rol, E., Romein, J. W., Roosjen, J., Ruiter, M., Scaife, A., van der Schaaf, K., Scheers, B., Schellart, P., Schoenmakers, A., Schoonderbeek, G., Serylak, M., Shulevski, A., Sluman, J., Smirnov, O., Sobey, C., Spreeuw, H., Steinmetz, M., Sterks, C. G. M., Stiepel, H.-J., Stuurwold, K., Tagger, M., Tang, Y., Tasse, C., Thomas, I., Thoudam, S., Toribio, M. C., van der Tol, B., Usov, O., van Veelen, M., van der Veen, A.-J., ter Veen, S., Verbiest, J. P. W., Vermeulen, R., Vermaas, N., Vocks, C., Vogt, C., de Vos, M., van der Wal, E., van Weeren, R., Weggemans, H., Weltevrede, P., White, S., Wijnholds, S. J., Wilhelmsson, T., Wucknitz, O., Yatawatta, S., Zarka, P., Zensus, A., and van Zwieten, J. (2013). LOFAR: The LOw-Frequency ARray. *Astron. Astrophys.*, 556:A2.

van Moorsel, G., Kemball, A., and Greisen, E. (1996). AIPS Developments in the Nineties. In Jacoby, G. H. and Barnes, J., editors, *Astronomical Data Analysis Software and Systems V*, volume 101 of *Astronomical Society of the Pacific Conference Series*, page 37.

van Uitert, E., Hoekstra, H., Schrabback, T., Gilbank, D. G., Gladders, M. D., and Yee, H. K. C. (2012). Constraints on the shapes of galaxy dark matter haloes from weak gravitational lensing. *Astron. Astrophys.*, 545:A71.

van Weeren, R. J., Intema, H. T., Oonk, J. B. R., Röttgering, H. J. A., and Clarke, T. E.

(2009). The discovery of diffuse steep spectrum sources in Abell 2256. *Astron. Astrophys.*, 508:1269–1273.

Vazza, F., Tormen, G., Cassano, R., Brunetti, G., and Dolag, K. (2006). Turbulent velocity fields in smoothed particle hydrodymanics simulated galaxy clusters: scaling laws for the turbulent energy. *Mon. Not. R. Astron. Soc.*, 369:L14–L18.

Venturi, T. (2011). Observational properties of diffuse radio sources in galaxy clusters . Current knowledge and open questions. *Mem. Societa Astronomica Italiana*, 82:499.

Venturi, T., Giacintucci, S., Brunetti, G., Cassano, R., Bardelli, S., Dallacasa, D., and Setti, G. (2007). GMRT radio halo survey in galaxy clusters at z = 0.2-0.4. I. The REFLEX sub-sample. *Astron. Astrophys.*, 463:937–947.

Venturi, T., Giacintucci, S., Cassano, R., Brunetti, G., Dallacasa, D., Macario, G., Setti, G., Bardelli, S., and Athreya, R. (2009). The GMRT Radio Halo Survey and Low Frequency Follow–up. In Saikia, D. J., Green, D. A., Gupta, Y., and Venturi, T., editors, *The Low-Frequency Radio Universe*, volume 407 of *Astronomical Society of the Pacific Conference Series*.

Vikhlinin, A., Kravtsov, A., Forman, W., Jones, C., Markevitch, M., Murray, S. S., and Van Speybroeck, L. (2006). Chandra Sample of Nearby Relaxed Galaxy Clusters: Mass, Gas Fraction, and Mass-Temperature Relation. *Astrophys. J.*, 640:691–709.

Voges, W., Aschenbach, B., Boller, T., Bräuninger, H., Briel, U., Burkert, W., Dennerl, K., Englhauser, J., Gruber, R., Haberl, F., Hartner, G., Hasinger, G., Kürster, M., Pfeffermann, E., Pietsch, W., Predehl, P., Rosso, C., Schmitt, J. H. M. M., Trümper, J., and Zimmermann, H. U. (1999). The ROSAT all-sky survey bright source catalogue. *Astron. Astrophys.*, 349:389–405.

Warren, M. S., Abazajian, K., Holz, D. E., and Teodoro, L. (2006). Precision Determination of the Mass Function of Dark Matter Halos. *Astrophys. J.*, 646:881–885.

Watson, M. G., Schröder, A. C., Fyfe, D., Page, C. G., Lamer, G., Mateos, S., Pye, J., Sakano, M., Rosen, S., Ballet, J., Barcons, X., Barret, D., Boller, T., Brunner, H., Brusa, M., Caccianiga, A., Carrera, F. J., Ceballos, M., Della Ceca, R., Denby, M., Denkinson, G., Dupuy, S., Farrell, S., Fraschetti, F., Freyberg, M. J., Guillout, P., Hambaryan, V.,

Maccacaro, T., Mathiesen, B., McMahon, R., Michel, L., Motch, C., Osborne, J. P., Page, M., Pakull, M. W., Pietsch, W., Saxton, R., Schwope, A., Severgnini, P., Simpson, M., Sironi, G., Stewart, G., Stewart, I. M., Stobbart, A.-M., Tedds, J., Warwick, R., Webb, N., West, R., Worrall, D., and Yuan, W. (2009). The XMM-Newton serendipitous survey. V. The Second XMM-Newton serendipitous source catalogue. *Astron. Astrophys.*, 493:339–373.

Weisskopf, M. C., Brinkman, B., Canizares, C., Garmire, G., Murray, S., and Van Speybroeck, L. P. (2002). An Overview of the Performance and Scientific Results from the Chandra X-Ray Observatory. *Pub. Astron. Soc. Pacific*, 114:1–24.

Wen, Z. L. and Han, J. L. (2013). Substructure and dynamical state of 2092 rich clusters of galaxies derived from photometric data. *Mon. Not. R. Astron. Soc.*, 436:275–293.

Willson, M. A. G. (1970). Radio observations of the cluster of galaxies in Coma Berenices - the 5C4 survey. *Mon. Not. R. Astron. Soc.*, 151:1–44.

Wilson, T. L., Rohlfs, K., and Hüttemeister, S. (2009). *Tools of Radio Astronomy*. Springer-Verlag.

Wylezalek, D., Galametz, A., Stern, D., Vernet, J., De Breuck, C., Seymour, N., Brodwin, M., Eisenhardt, P. R. M., Gonzalez, A. H., Hatch, N., Jarvis, M., Rettura, A., Stanford, S. A., and Stevens, J. A. (2013). Galaxy Clusters around Radio-loud Active Galactic Nuclei at 1.3 z 3.2 as Seen by Spitzer. *Astrophys. J.*, 769:79.

Young, T. (1801). The Bakerian Lecture: On the Mechanism of the Eye. *Philosophical Transactions of the Royal Society of London Series I*, 91:23–88.

ZuHone, J. and Markevitch, M. (2012). Probing the Microphysics of the Intracluster Medium with Cold Fronts in the ICM. In Ness, J.-U., editor, *Galaxy Clusters as Giant Cosmic Laboratories*, page 64.

Zwicky, F. (1933). Die Rotverschiebung von extragalaktischen Nebeln. *Helvetica Physica Acta*, 6:110–127.

Zwicky, F. (1937a). On a New Cluster of Nebulae in Pisces. *Proceedings of the National Academy of Science*, 23:251–256.

Zwicky, F. (1937b). On the Masses of Nebulae and of Clusters of Nebulae. *Astrophys. J.*, 86:217.

Zwicky, F., Herzog, E., and Wild, P. (1968). *Catalogue of galaxies and of clusters of galaxies.*